

GEOLOGICA ULTRAIECTINA

Mededelingen van de
Faculteit Aardwetenschappen
Universiteit Utrecht

No. 172

**EVOLUTION OF
THE CONTINENTAL UPPER MANTLE:**

**NUMERICAL MODELLING OF THERMO-CHEMICAL
CONVECTION INCLUDING PARTIAL MELTING**

JEROEN HENK DE SMET

GEOLOGICA ULTRAIECTINA

Mededelingen van de
Faculteit Aardwetenschappen
Universiteit Utrecht

No. 172

**EVOLUTION OF
THE CONTINENTAL UPPER MANTLE:
NUMERICAL MODELLING OF THERMO-CHEMICAL
CONVECTION INCLUDING PARTIAL MELTING**

JEROEN HENK DE SMET

**EVOLUTION OF
THE CONTINENTAL UPPER MANTLE:
NUMERICAL MODELLING OF THERMO-CHEMICAL
CONVECTION INCLUDING PARTIAL MELTING**

Evolutie van de continentale bovenmantel:

**Numeriek modelleren van thermo-chemische
convectie met inbegrip van partiëel smelten**

(met een samenvatting in het Nederlands)

PROEFSCHIFT

TER VERKRIJGING VAN DE GRAAD VAN DOCTOR
AAN DE UNIVERSITEIT UTRECHT
OP GEZAG VAN DE RECTOR MAGNIFICUS, PROF. DR. H.O. VOORMA,
INGEVOLGE HET BESLUIT VAN HET COLLEGE VOOR PROMOTIES
IN HET OPENBAAR TE VERDEDIGEN
OP MAANDAG 10 MEI 1999 DES MIDDAGS TE 14:30 UUR

DOOR

JEROEN HENK DE SMET

GEBOREN OP 15 MEI 1968, TE RIJSWIJK

promotor: Prof. dr. N.J. Vlaar
co-promotor: dr. A.P. van den Berg
Department of Theoretical Geophysics,
Utrecht University

ISBN: 90-5744-029-6

... slow motion is better than no motion
(William Collins, 1979)

- CONTENTS 1

1 GENERAL INTRODUCTION 5

I General concepts and model description 11

2 MODEL DESCRIPTION 13

- 2.1 Partial melting of mantle peridotite 13
 - 2.1.1 Basic petrology 13
 - 2.1.2 Three phase-diagram parameterizations 14
- 2.2 Governing model equations 15
 - 2.2.1 Driving forces in thermo-chemical convection 15
 - 2.2.2 Upper mantle phase-transitions 16
 - 2.2.3 Rheological model 20
 - 2.2.4 Conservation equations 20
- 2.3 Model assumptions and approximations 21

3 NUMERICAL METHODS 23

- 3.1 Introduction 23
- 3.2 Energy equation 23
- 3.3 The Stokes equation 24
- 3.4 Transport equation 24
 - 3.4.1 Characteristics based method 25
 - 3.4.2 Tracer particle method 25
- 3.5 Numerical time integration 25

II Modelling results 27

4 STABILITY AND GROWTH OF CONTINENTAL SHIELDS IN MANTLE CONVECTION MODELS INCLUDING RECURRENT MELT PRODUCTION 29

- 4.1 Introduction 29
- 4.2 Model description and numerical method 31
- 4.3 Numerical modelling results 33
- 4.4 Discussion 41
- 4.5 Conclusions 42

5 THE EVOLUTION OF CONTINENTAL ROOTS IN NUMERICAL THERMO-CHEMICAL MANTLE CONVECTION MODELS INCLUDING DIFFERENTIATION BY PARTIAL MELTING 43

- 5.1 Introduction 43
- 5.2 The model 45
 - 5.2.1 Conceptual continental model 45
 - 5.2.2 Parameterization of the partial melting process 48
 - 5.2.3 Thermal coupling between upper and lower mantle 49
 - 5.2.4 Governing model equations and numerical methods 49
- 5.3 Numerical modelling results 50

5.3.1	Early evolution	51
5.3.2	Long term evolution	53
5.3.3	Patterns of mantle differentiation	55
5.3.4	Global evolution	56
5.4	Concluding remarks	58
6	A CHARACTERISTICS-BASED METHOD FOR SOLVING THE TRANSPORT EQUATION AND ITS APPLICATION TO THE PROCESS OF MANTLE DIFFERENTIATION AND CONTINENTAL ROOT GROWTH	61
6.1	Introduction	62
6.2	Conceptual model and equations	62
6.3	The characteristics-based hybrid scheme	64
6.4	Test applications	66
6.4.1	A one-dimensional test case	66
6.4.2	A two-dimensional benchmark	69
6.5	Application of the hybrid scheme to the continental upper mantle model	70
6.6	Concluding Remarks	73
7	EARLY FORMATION AND LONG-TERM STABILITY OF CONTINENTS RESULTING FROM DECOMPRESSION MELTING IN A CONVECTING MANTLE	75
7.1	Introduction	76
7.2	Model description	76
7.3	Modelling results	77
7.3.1	Model evolution up to 4 billion years	77
7.3.2	Detailed dynamics of diapiric partial melting	80
7.3.3	Comparison with theoretical geotherms	82
7.3.4	Age and compositional structure of continental roots	84
7.4	Discussion and conclusions	87
8	SEISMIC VELOCITY STRUCTURE OF THE ROOT INFERRED FROM THE MODEL	91
8.1	Introduction	91
8.2	Seismic velocity parameterizations	91
8.3	Results	93
8.3.1	Vertical velocity profiles	93
8.3.2	Seismic reflection coefficients	94
8.4	Concluding remarks	96
9	GENERATION OF KOMATIITE IN THE TRANSITION ZONE	97
9.1	Introduction	97
9.2	Model description	98
9.3	Results	99
9.3.1	Upwelling from the deepest upper mantle	99
9.3.2	Melting in the upper mantle transition zone	100
9.4	Conclusions	103

10 COLOUR PLATES	105
- BIBLIOGRAPHY	117
A FORMULATION OF PARTIAL MELTING SOURCE TERM	125
B DISCRETIZED FORM OF THE ENERGY EQUATION	127
- SUMMARY	131
- SAMENVATTING (SUMMARY IN DUTCH)	133
- DANKWOORD (ACKNOWLEDGMENTS)	135
- CURRICULUM VITAE	137

Chapter 1

GENERAL INTRODUCTION

Part of the present-day continental area is almost as old as the Earth itself. The Earth has an estimated age of about 4.6 *Ga*. The oldest preserved rocks have their origin in the Early Archaean (4.0 – 3.5 *Ga b.p.*). Only old zircons are sometimes estimated to be older than these oldest preserved rocks, and the zircons form an indication that mechanical erosion took place during the Earth's early evolution. In sharp contrast to these ages is the age of the oldest modern oceanic lithosphere, which is no more than 180 *Ma*. The concept of present-day style of plate tectonics placed in the framework of upper mantle convection gives a sufficient explanation for this limited age of oceanic lithosphere. Modern oceanic lithosphere is generated at a Mid Oceanic Ridge (MOR) and destroyed at subduction zones. However, the concept of plate tectonics does not explain the long-term stability and evolution of the oldest continental lithosphere, which is the subject of this thesis.

The study of the Precambrium evolution of the Earth (4.0–0.6 *Ga b.p.*) is hampered, since no Precambrium oceanic lithosphere is preserved. Preservation of such lithosphere could reveal information on the style of oceanic upper mantle dynamics during the Precambrium. Moreover, many of the preserved continental rocks have been reworked by several, not necessarily known, processes. This increases the difficulties that arise in the interpretation of these rocks.

The Archaean is an important era in the Earth's evolution. It (4.0 – 2.5 *Ga b.p.*) covers about one third of the Earth's history, and initial formation and stabilization of continental lithosphere is thought to have taken place during this period.

An early Earth setting is needed for the initial state of the presented model that describes the continental upper mantle evolution. Therefore, some Archaean geological findings are reviewed. They have implications which are relevant for this modelling study. Despite the problems involved in the interpretation of the Archaean rock record, several conclusions can be drawn.

Evidence for the presence of surface water during the early evolution of the Earth exists in the form of pillow lavas that are found in Archaean terrains. This is a lava typical for subaqueous outflow conditions. Furthermore, sediments are found that have Archaean ages. These sediments are related to the presence of surface water (DiMarco and Lowe 1989). In addition, cratonic shields sometimes contain fossilized systems of single-cell organisms (Buick 1984; Hunter and Stowe 1997). These fossilized stromatolites are build principally by almost exclusively aquatic plants. The ages of these

stromatolites have been pushed back to 3.0 *Ga*. The presence of surface water restricts the surface temperature to approximately 0 – 100°C, although it cannot be stated with certainty that this situation existed continuously.

Age determinations are based on measurements of specific radiogenic isotope concentrations. The radioactive decay of some isotopes generates large amounts of radiogenic heat. During the Early Archaean, this important heat source is estimated to be 2 to 3 times as great as it is today (Turcotte and Schubert 1982). In addition, heat was stored in the Earth during accretion (primitive heat) and heat was released during formation of the core. These are the three major reasons to assume that the mantle during the Archaean was several hundreds of degrees hotter than at present. Besides, Archaean terrains contain komatiites. Their presence supports the hot Earth hypothesis.

Secondary melting of hydrated basalts generated the primary continental crustal rocks (Taylor and McLennan 1985), which on average are less dense than basaltic rocks. Exhumation of about 30 *km* continental crust during the Late Archaean and Proterozoic resulted in the surfacing of high-grade terrains. The present-day thickness of old cratonic crust is about 40 *km*. Thus almost the same amount of old cratonic continental crust has been eroded since the Archaean.

The dynamical process by which remelted basalt forms continental crustal segments is subject of debate (Rudnick 1995). Early continental formation from oceanic lithosphere is probably influenced by the effect that the much thicker oceanic crust and depleted lithosphere had on the early upper mantle dynamics.

Oceanic lithosphere consists of a basaltic surface layer with a residual harzburgite layer underneath it. Fertile upper mantle rock reduces to the harzburgitic upper mantle layer when basaltic melt is extracted and segregates to form the surface layer. This process of basaltic crust segregation is the consequence of partial melting of the upper mantle rock when pressure is released in an ascending volume. In a hotter upper mantle, i.e. Archaean upper mantle, the differentiated layers were much thicker (Sleep and Windley 1982; Vlaar 1985), because partial melting started at higher pressures.

Since harzburgite is less dense than its fertile source rock, a thicker layer of harzburgite has a large stabilizing effect. At larger depths, the thicker basaltic crust is probably in its dense eclogite phase, which forms another important factor that can effect the Archaean upper mantle dynamics (Vlaar et al. 1994). Hence, the compositional signature of the Archaean oceanic lithosphere influences the buoyancy (Vlaar and Van Den Berg 1991; Vlaar et al. 1994), and rheology (Hoffman and Ranalli 1988) effecting the dynamical processes in a hotter Archaean upper mantle. The question whether obduction, subduction or a combination of these processes occurred remains unanswered. Convection was presumably more vigorous in a hot mantle (Jackson and Pollack 1984; Vlaar 1986). Nevertheless, the oldest stable continental segments were formed in spite of this vigorous convection regime,

Figure 1.1 is a map of the world showing the oldest surfacing continental areas as present today (Pollack et al. 1993). The grey areas are surfacing Archaean (4.0 – 2.5 *Ga b.p.*) regions. The boundary between Archaean and Proterozoic (2.5 – 0.6 *Ga*) is probably not precisely fixed at 2.5 *Ga b.p.*, but had a more transient character. Thus the map only forms an indication of locations of the Archaean terrains. Younger continental crust is supposed to have formed around these Archaean nuclei. How fast and when the

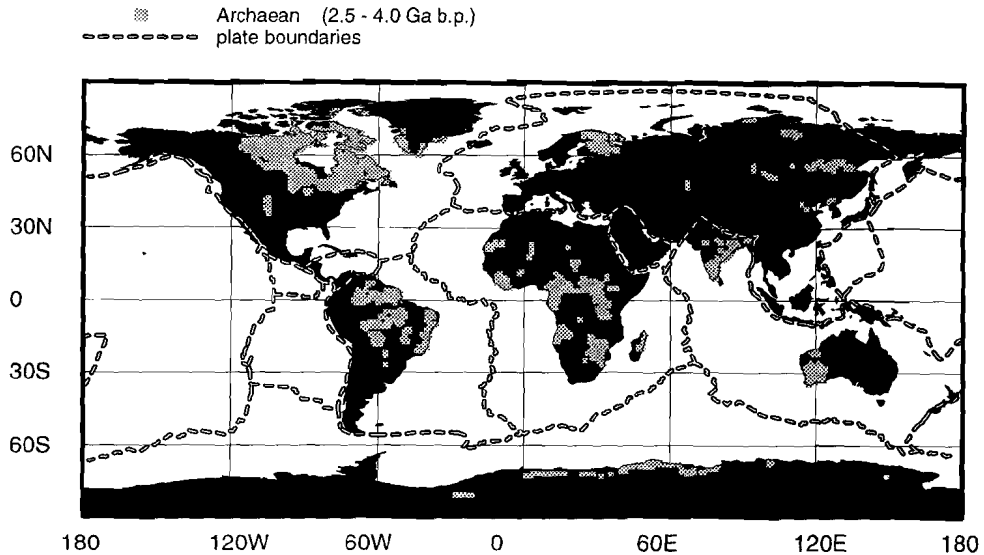


Figure 1.1: World map with in black the non-subaqueous parts of the continents and dashed lines the plate boundaries. The surfacing Archean continental areas are shown in grey (after Pollack et al., 1993).

stable continental areas were formed remains an unanswered question. Several models that describe the growth of volume of continental crust have been proposed and they are compiled by Windley (1995). Most model concepts show that continental formation started in the Early Archean and that the major increase in continental volume was established during the Late Archean. Several models show a major surge of crustal growth during the Mid and Late Archean after which the process slowly continues (Pollack 1986).

At present, the cratons are laying on a thick and cold lithosphere as revealed by seismological studies, heat flow measurements, and data inferred from xenoliths and other upper mantle rock samples.

The spherical harmonics of degree 12 representation of surface heat flow data is given in Figure 1.2 (Pollack et al. 1993). The areas where continental heat flow rates reach values less than $\sim 60 \text{ mWm}^{-2}$ coincide with Archean terrains (compare Figure 1.1). The best examples are Western Australia, Southern Africa, Western Africa, Siberia, the Eastern part of North America, and the Eastern part of South America. Less pronounced are the minimum heat flow values at the Canadian and Scandinavian shields. Low surface heat flow thus correlates with old continental crust.

As early as the 1960s, seismologists showed that the continental upper mantle differs from its oceanic counterpart. Many different seismological studies show that underneath continental shields the seismic velocities are significantly higher than underneath the oceanic plates (Jordan 1975; Anderson 1990; Zhang and Tanimoto 1993; Trampert and Woodhouse 1996). Figure 1.3 shows the shear wave anomalies at a depth of 150 km as

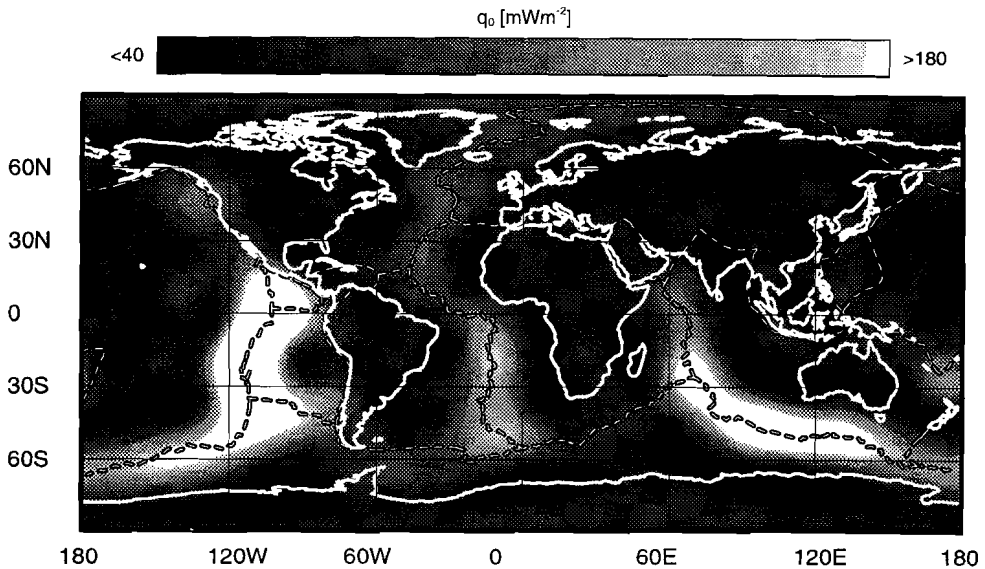


Figure 1.2: Spherical harmonic degree 12 representation of heat flow data (Pollack et al., 1993). Plate boundaries are indicated with black dashed lines and thick solid white lines show the boundaries between water and the surfacing continents.

found by Woodhouse and Trampert (1995) through inversion of body and surface wave travel times. The deep regions with high velocities are overlain by surface areas which correspond to the Archaean shields. This correlation vanishes at a certain depth. It is still controversial to what depths these high velocity 'continental roots' precisely extend. Agreement exists that the minimum depth extend is at least 150 km . Maximum depth extend estimates vary from less than 200 km (Anderson 1990) to over 350 km (Polet and Anderson 1995). Problems in determining the depth extend of the continental roots concern the resolution of, and the error estimates and effects in the applied methods (Polet and Anderson 1995; Trampert 1998).

The composition of these roots is similar to present-day oceanic residual lithosphere. However, differences exist and most of them are poorly understood. One difference is relevant in the present context, since it might be related to komatiitic melt generation.

For variably-depleted peridotites of oceanic mantle origin, a relation is found between olivine contents and magnesium number. These oceanic peridotite samples are relatively young. This magnesium-olivine relation is not observed for depleted garnet peridotites as pointed out by Boyd (1989). A possible explanation is given by Takahashi (1990) and is related to higher mantle temperatures during which genesis of the cratonic depleted roots presumably took place. Komatiitic melt is extracted as a result of high degrees of partial melting that can be established in a hotter mantle. According to Takahashi (1990) komatiitic melt extraction can explain why depleted garnet peridotites do not show the oceanic magnesium-olivine relation. This is consistent with the concept of high Archaean mantle temperatures, and it is supported by the presence of komatiitic

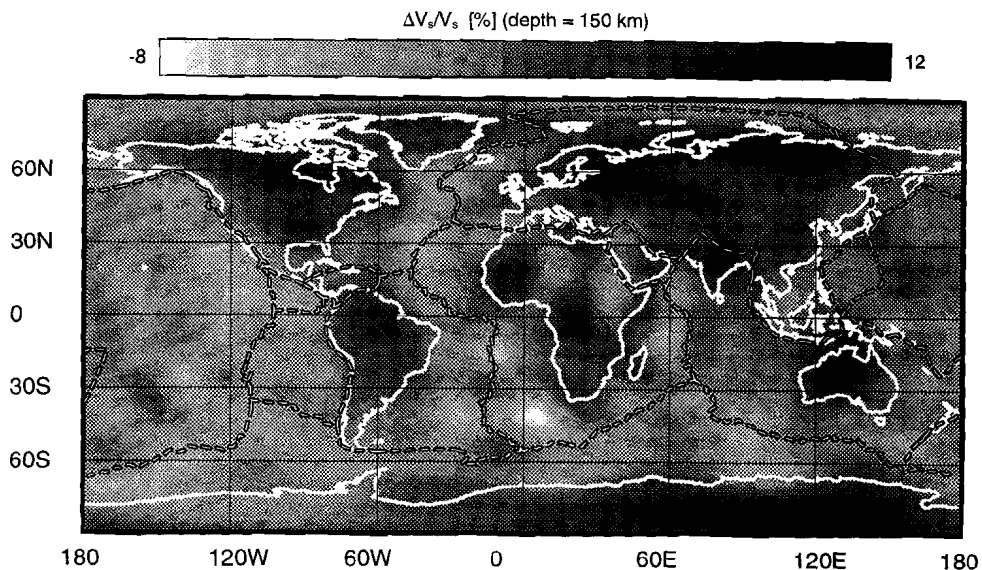


Figure 1.3: Shear wave velocity anomalies at 150 km depth (Woodhouse & Trampert, 1995). Dashed and solid lines are as in Figure 1.2.

rocks in Archaean greenstone belts and the absence of such a komatiitic signature in younger continental areas.

It has also been suggested that the komatiites were generated during the Archaean in a hotter mantle and that they geochemically and petrologically fit to a lower mantle source. In the suggested scenario, these magnesium-rich melts originate from this deeper part of the mantle in the tail of a plume (Campbell et al. 1989). This seems an unnecessarily complicated way to explain the presence of komatiites in Archaean terrains.

A diapiric melting scenario of upper mantle rock solely explains the generation of komatiitic melt. It is assumed here that partial melting is initiated at relative large depths in the hot center of the diapir. This hot center of the diapir can reach high degrees of depletion and komatiitic melt is generated. In the colder part of the upwelling diapir, partial melting starts at shallower depths and the reached degrees of depletion are less high. Both komatiite and basalt are generated (Vlaar, personal communication).

This diapiric melting scenario in which a hot thermal upwelling impinges on a colder lithosphere might also explain another observation. Archaean terrains contain diamonds which come from depths between 150 and 200 km (Boyd et al. 1985) and it is widely held that these stones were formed during the Archaean (~ 3 Ga b.p.) at temperatures of 900 – 1200°C (Boyd et al. 1985; Boyd and Gurney 1986). This is an indication that the thermal state of the Archaean mantle did not differ much from the modern mantle. This is a paradoxical observation. This seemingly contradictory observation fits in a scenario with local hot upwellings where large parts of the continental lithosphere are relatively cold at the same time.

Organization and scope of this thesis

The evolution of the continental upper mantle forms the scope of this numerical modelling study. An Archaean setting which follows from the previous discussion gives the initial condition for the used model in which early formation of the depleted continental root is the direct consequence of early differentiation in a hot upper mantle.

Others have proposed different hypothesis to explain the presence of thick depleted roots. Imbricated slabs of Archaean oceanic lithosphere (Kusky 1993), and similar buoyant subduction mechanisms, combined with continental collision (Jordan 1988) or not (Abbott 1991) have been suggested. These scenarios assume subduction in a plate tectonics scenario almost similar to the modern process.

In this thesis, it is demonstrated that a hot Earth can explain the presence of the continental roots. The scenario does not depend on any specific type of subduction of Archaean oceanic lithosphere. This study consists of two parts.

Part I: General concepts and model description :

The model incorporates the fundamental process of pressure-released partial melting of fertile mantle peridotite. This process is discussed in Section 2.1 where the basic upper mantle petrology and the used parameterizations of the phase-diagrams are introduced. The equations describing the numerical model are given in Section 2.2 followed by an elaboration on the most important model approximations and assumptions in Section 2.3. The numerical methods are briefly discussed in Chapter 3.

Part II: Modelling results :

Within the concept of a hotter upper mantle in the early Earth, thick depleted roots as present today can exist when they are formed during the Early Archaean as discussed in Chapter 4 and 5. Furthermore, the model explains the long-term stability (several billions of years) of continental shields, and that large variations in the depth extend of the root can evolve. This long-term evolution and a comparison of model results with the present-day state of cratonic upper mantle is discussed in Chapter 7. In addition, a small-scale mechanism is found by which the root can grow (Chapter 4-7). This diapiric process of continental root growth takes place due to cooling from the top rather than in spite of this cooling. Basaltic melt is generated which possibly adds crustal material.

To study the thermo-chemical differentiation process, an adaptive numerical method is developed. Several benchmarks and the applicability of this method are discussed in Chapter 6.

Some observations for which no satisfying explanation is known might be solved, or placed in a new perspective, by the occurrence of the diapiric growth process (Chapter 4 and 7).

The possible occurrence of deep upper mantle differentiation and the possible consequences are discussed in Chapter 5 and 9.

Part I

General concepts and model description

Chapter 2

MODEL DESCRIPTION

2.1 Partial melting of mantle peridotite

2.1.1 Basic petrology

Ringwood (1982) gives a simple petrological stratification for the oceanic upper mantle. His view on the composition of the deeper mantle is consistent with the outline Agee (1993) provides. The upper mantle composition changes gradually with increasing depth from harzburgitic rock to lherzolitic rock and finally to fertile upper mantle rock. The compositional situation is simplified for the aims of this thesis. A slightly more detailed stratification is given by Blatt and Tracy (1996)(p.145). Their overview also includes garnet, spinel, and plagioclase phases.

Fertile upper mantle rock, i.e. capable of producing basaltic melt, is referred to as lherzolite. Lherzolite, harzburgite, wehrlite, and dunite are all peridotites Blatt and Tracy (1996)(p.73). The upper mantle extends to a depth of ~ 670 km where the boundary between the upper and lower mantle is situated. The deepest upper mantle region is assumed to consist of fertile upper mantle rock, i.e. lherzolite. During partial decompression melting incompatible elements are extracted from the lherzolite and expelled with the basaltic melt that forms the primitive crust. Here, the solid residue is referred to as harzburgite, which experiences a gradual change in composition as a result of partial melting and melt extraction. The degree of depletion is defined here as the mass fraction of the melt produced by a certain volume of peridotite. The residue is referred to as depleted peridotite, i.e. harzburgite. The density of the harzburgite decreases with increasing degree of depletion. This density effect (Jordan 1979; Niu and Batiza 1991) is one of the key-elements in this modelling study.

The models as used by Kostopoulos (1991) and Hirschmann et al. (1998) both indicate roughly the same petrological change upon melting. The garnet lherzolite, or undepleted peridotite, is a four component system consisting of garnet (Gt), orthopyroxene (Opx), clinopyroxene (Cpx), and olivine (Ol) from which first Gt and Cpx are removed during partial melting. Whether the extraction of Opx starts at low degrees of depletion (Kostopoulos 1991) or at much higher values (Hirschmann et al. 1998) and whether Gt is completely removed or not at low degrees of depletion is contradictory within both model frameworks. Ringwood (1982) states that Gt and Cpx extraction is completed at relative low degrees of melting, which is consistent with the data as given by Jordan (1979). Most important in the present work is that the harzburgite has a density which is intrinsically less than the density of the lherzolitic source rock.

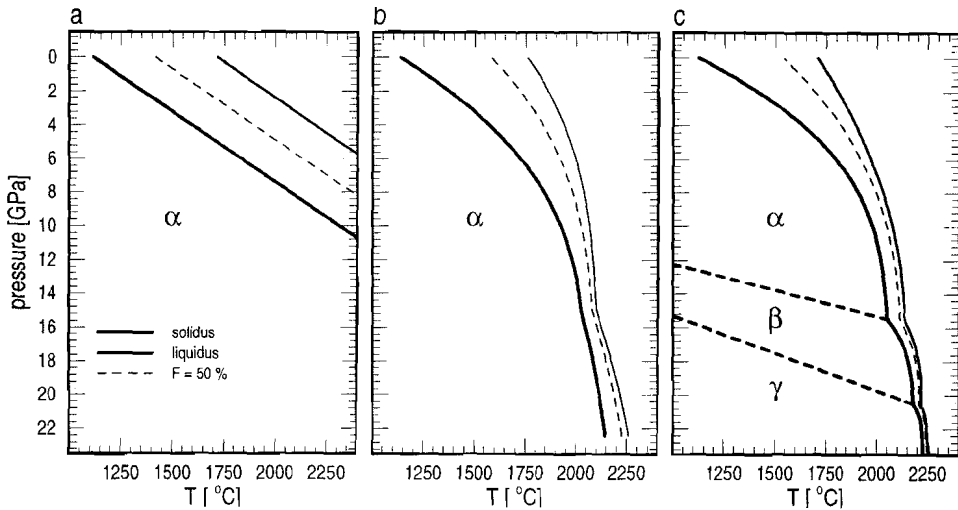


Figure 2.1: The three different phase-diagram parameterizations as used in the present work. The thick solid, thin solid, and thin dashed lines represent the solidus, liquidus, and $F = 50\%$ equilibrium lines, respectively. The solid state phase of olvine is indicated with α , β , and γ . **a** The oversimplified parameterization with parallel and straight solidus and liquidus. A linear relation for $F(\theta)$ is applied. **b** The more realistic curved phase diagram with a kink in the equilibrium lines corresponding to the $\alpha \leftrightarrow \beta$ solid-state phase transition not incorporated. **c** The last improvement including both $\alpha \leftrightarrow \beta$ and $\beta \leftrightarrow \gamma$ solid-state phase transitions which have also been incorporated in the model.

Most melting experiments relevant for this four component system are only performed at low pressure ($< 3 \text{ GPa}$) and extensions to higher pressures are needed but not precisely known. Niu (1997) shows that there is a pressure-dependent trend in the extraction of the minerals when their abundances are expressed in weight-percentages.

Also the composition of the basaltic melt is dependent on the pressure where partial melting takes place. During the Archaean, mantle temperatures were higher than at present, and melting started at larger depths, i.e. higher pressures. Komatiitic melt, i.e. magnesium-rich basalts, are thought to be generated through partial decompression melting at high pressure (Bickle et al. 1977; Takahashi 1990; Herzberg 1992; Bickle 1993; Nisbet et al. 1993).

2.1.2 Three phase-diagram parameterizations

Three different phase-diagrams describing the differentiation by partial melting have been used in this work. They include different parameterizations for solidus and liquidus equilibrium lines and correspond to a static situation without melt extraction (i.e. batch melting). In addition, the change in petrology upon melting results in a non-linear relation between the degree of depletion F and the normalized supersolidus temperature θ , which is taken into account in more realistic phase-diagram parameterizations.

Figure 2.1.a shows a simplified phase-diagram which is appropriate for melting up to approximately 150 km depth ($\sim 5 \text{ GPa}$). The parameterization is based on the data presented by Takahashi and Kushiro (1983). The parallel solidus and liquidus have a slope of $dT_s/dp = 120 \text{ K GPa}^{-1}$ and the solidus temperature is 1115°C at zero pressure, whereas the liquidus is situated at a 600°C higher temperature. The change

in F between solidus and liquidus follows a linear parameterization based on data given by Jacques and Green (1980).

Figure 2.1.b is a first improvement to the phase-diagram of Figure 2.1.a. It has curved equilibrium lines and the temperature difference between solidus and liquidus decreases with increasing pressure. This is important for modelling deep partial melting. It incorporates a kink in the equilibrium lines where the solid-state phase transition from α -olivine to β -spinel takes place. This transition is, however, not taken into account in the subsolidus part of the phase-diagram. Up to pressures of 15 GPa , the solidus and liquidus are based on work presented by Gasparik (1990) and Takahashi (1990). At higher pressures the parameterization is based on data given by Ohtani et al. (1986). The non-linear relation for $F(\theta)$ used for this phase-diagram is shown in Figure 5.2 and given by McKenzie and Bickle (1988). The parameterization for this phase-diagram is given in Section 5.2.

Figure 2.1.c shows the most complete parameterization which also includes the second solid-state phase-transition from β -spinel to γ -spinel. Both phase-transitions are also incorporated in the rest of the phase-diagram. The corresponding Clausius-Clapeyron curves are drawn as thick solid dashed lines for which details are discussed in Section 2.2.2. The solidus and liquidus are based on data presented by Herzberg and Zhang (1996) and the parameterization used is given in Section 9.2. The $F(\theta)$ -relation is identical to the $F(\theta)$ -relation incorporated in the phase-diagram shown Figure 2.1.b.

2.2 Governing model equations

The fact that fertile upper mantle source rock is denser than its differentiated harzburgitic residue has a large influence on the dynamics of the upper mantle. The extracted basalt forms a low density crust and, when subject to secondary melting processes, continental crust can be formed (Taylor and McLennan 1985; Windley 1995). In the presented model this phase of continental crust formation is not incorporated. The harzburgitic layer situated below the crust is less dense than the underlying lherzolite and is therefore gravitationally stable. Thus incorporation of thermal buoyancy only forms an incomplete description of upper mantle dynamics, since nothing prevents the harzburgite to take part in the upper mantle convection when rheological effects are disregarded. Including the stabilizing compositional buoyancy of the harzburgite is of crucial importance in the description of upper mantle dynamics.

In the following discussion, the basic equations are given for the composition, velocity, pressure and temperature that describe the dynamics of thermo-chemical convection in a viscous upper mantle model of the Earth. Symbol definitions are given in Table 2.1.

2.2.1 Driving forces in thermo-chemical convection

Thermal expansion and compositional changes upon differentiation influence the density of upper mantle rock. The resulting total density variations produce the driving forces in our thermo-chemical convection model. Partial melting changes the composition of the residual matrix and reduces the density of this solid rock as discussed in Section 2.1. The applied parameterization of this effect is based on data given by Jordan (1979):

$$\rho_s(F) = \rho_0 - \delta\rho F \quad (2.1)$$

where F is the mass fraction of the generated basaltic melt, commonly referred to as the degree of depletion. Incorporating thermal expansion results in an equation of state (EOS) given by:

$$\rho(T, F) = \rho_s(F) [1 - \alpha(T - T_{srf})] \quad (2.2)$$

With the applied values of $\delta\rho = 226 \text{ kgm}^{-3}$, based on the work presented by (Jordan 1979), and $\alpha = 3 \cdot 10^{-5}$ the dynamical effect of the compositional change can be expressed by a thermal equivalent. A relatively small depletion increment of $\Delta F = 0.1$ is compensated by a thermal decrement of approximately $\Delta T = -110 \text{ K}$. Only part of this decrement is accomplished by latent heat consumption upon isentropic partial melting. Hence, the instant net effect of partial melting is a reduction of the residual density of the solid matrix. The linearized EOS is:

$$\rho(T, F) = \rho_0 \left[1 - \frac{\delta\rho}{\rho_0} F - \alpha(T - T_{srf}) \right] \quad (2.3)$$

Note that in this EOS no contribution of liquefied melt is incorporated, which is discussed in Section 2.3.

2.2.2 Upper mantle phase-transitions

Two major solid-state exothermal phase-transitions for olivine are present in the upper mantle:

- α -olivine to β -spinel ($i = 1$),
- β -spinel to γ -spinel ($i = 2$).

Solid-state phase-transitions of the other minerals present in upper mantle material are not taken into account. When the olivine phase-transitions are incorporated in the model, the corresponding parameterizations are based on results given by Herzberg and Zhang (1996). The density jumps are derived from data presented by Yoshioka et al. (1997). The parameters are given in Table 2.2. These phase-transitions have an additional influence on ρ and T . A fundamental approach to the latent heat effect of phase transformations is described by Bina (1998).

The phase-diagram determines the phase functions $\Gamma_i (i = 1, 2)$ and yields:

$$\rho(\Gamma) = \rho_0 \left[1 + \sum_{i=1,2} X_i \Gamma_i \frac{\delta\rho_i}{\rho_0} \right] \quad (2.4)$$

where X_i is the volume fraction of olivine. The incorporation of this fraction is the correction for the presence of other upper mantle minerals.

Fertile upper mantle peridotite consists of approximately 60 weight-% olivine (Ol) in the α -olivine temperature and pressure range and olivine co-exists with the following other minerals: Garnet (Gt), Orthopyroxene (Opx), and Clinopyroxene (Cpx) (Jordan 1979; Ringwood 1982). We adjust the phase-transition contribution for the presence of these other minerals. Let X_0 be the volume fraction of α -olivine of an upper mantle control volume and m_m the mass of the rest of this control volume. Conservation of mass yields that after transition to the β -spinel phase

$$X_0 \rho_\alpha + m_m = X_1 \rho_\beta + m_m \quad (2.5)$$

yielding

$$X_1 = X_0 \frac{\rho_\alpha}{\rho_\beta} \quad (2.6)$$

for the volume fraction β -olivine X_1 . By assuming that the mass fraction (or weight-%) equals the volume fraction of α -olivine and $\rho_\alpha = \rho_0$, we find:

$$X_1 = 60\% \frac{\rho_\alpha}{\rho_\beta} \quad (2.7)$$

and similar for the second phase-transition at higher pressure:

$$X_2 = X_1 \frac{\rho_\alpha}{\rho_\beta} = 60\% \frac{\rho_\alpha}{\rho_\gamma} \quad (2.8)$$

Extension of the EOS in Equation 2.2 with these phase-transitions effects gives:

$$\rho(T, F, \Gamma) = \rho_0 \left[1 - \frac{\delta\rho}{\rho_0} F - \alpha(T - T_0) + \sum_{i=1,2} X_i \Gamma_i \frac{\delta\rho_i}{\rho_0} \right] \quad (2.9)$$

after linearization. Note that we used X_i for the transition from phase $i - 1$ to phase i instead of a gradual transition from X_{i-1} to X_i .

The phase-transitions obey the Clausius-Clapeyron (CC) relation:

$$\gamma_i = \left. \frac{dp}{dT} \right|_i = \left. \frac{\Delta S}{\Delta V} \right|_i = \left. \frac{\Delta S}{\Delta(\rho^{-1})} \right|_i \approx - \frac{\rho_0^2 \Delta S_i}{\delta\rho_i} \quad (2.10)$$

The latent heat associated with these phase-transitions is determined through this approximation:

$$\Delta Q = -T \Delta S_i \approx T \frac{\gamma_i \delta\rho_i}{\rho_0^2} \quad (2.11)$$

For both phase-transitions a smooth function over the width of the transition interval $2\Delta z_{\Gamma_i}$ (see Table 2.2) is applied:

$$\Gamma_i(z) = \frac{1}{2} \left[1 + \sin \left(\frac{\pi}{2} \frac{\Delta z_i(z)}{\Delta z_{\Gamma_i}} \right) \right] \quad (2.12)$$

under the condition

$$- \Delta z_{\Gamma_i} \leq \Delta z_i(z) \leq \Delta z_{\Gamma_i} \quad (2.13)$$

where

$$\Delta z_i(z) = z - \frac{\gamma_i \cdot (T(z) - T_i^{CC}(p=0))}{\rho_0 g} \quad (2.14)$$

symbol	definition	value	units
\vec{x}	spatial coordinates: (x, z)	—	m
z	vertical coordinate aligned with gravity	—	m
ρ_0	reference density	3416	kgm^{-3}
ρ	effective density: $\rho(T, F, \Gamma)$	—	kgm^{-3}
ρ_c	crustal density at $T = T_{surf}$	3000	kgm^{-3}
$\rho_s(F)$	density of solid matrix: $\rho_0 - F\delta\rho$	—	kgm^{-3}
ρ_f	density of liquefied melt	2800	kgm^{-3}
$\delta\rho$	density drop upon full differentiation	226	kgm^{-3}
$\Delta\rho$	density anomaly: $\rho - \rho_0$	—	kgm^{-3}
F	degree of depletion	—	—
α	thermal expansion coefficient	3×10^{-5}	K^{-1}
η	non-dimensional viscosity	—	—
η_0	reference viscosity	10^{21}	Pa s
η_m	Arrhenius type p, T -dependent mantle viscosity	—	Pa s
η_{max}	maximum viscosity	10^{24}	Pa s
E	activation energy	250	$kJmol^{-1}$
V	activation volume	11.0 or 7.5	$\mu m^3 mol^{-1}$
R	gas constant	8.3143	$Jmol^{-1}K^{-1}$
$B(F)$	viscosity pre-factor	$(90 \text{ or } 5.53) \times 10^{11}$	Pa s
\vec{u}	advection velocity	—	ms^{-1}
w	vertical component of advection velocity	—	ms^{-1}
e	strain rate tensor: $\nabla\vec{u} + \nabla\vec{u}^T$	—	s^{-1}
e^2	squared 2nd invariant of the e -tensor: $e^2 = 1/2 \cdot e_{ij}e_{ij}$	—	s^{-2}
p	pressure	—	Pa
π_i	reduced pressure: $\pi_i = p - p_i - \gamma_i T$ (see Table 2.2)	—	Pa
Δp	non-dimensional hydrodynamic pressure	—	—
T	non-dimensional temperature	—	—
ΔT	temperature scale	2200	K
T_{surf}	surface temperature	273.15	K
T_0	non-dimensional surface temperature: $T_{surf}/\Delta T$.12416	—
$T_s(p)$	pressure dependent solidus temperature	—	K
$T_l(p)$	pressure dependent liquidus temperature	—	K
$\Delta T(p)_{sl}$	distance between solidus and liquidus	—	K
$\Theta(p, T)$	normalized super-solidus temperature	—	—
q	heat-flow density	—	Wm^{-2}
$\langle X \rangle_{hor}$	horizontally averaged quantity X	—	—
τ	deviatoric stress tensor	—	Pa
h	depth scale	670	km
λ	radioactive decay constant	.347	$(Ga)^{-1}$
κ	thermal diffusivity: $k/(\rho_0 c_p)$	10^{-6}	$m^2 s^{-1}$
k	thermal conductivity	3.416	$Wm^{-1}K^{-1}$
c_p	heat capacity at constant pressure	1000	$Jkg^{-1}K^{-1}$
ΔS	entropy change upon full differentiation	300	$Jkg^{-1}K^{-1}$
$\mathcal{P}(p, T, F)$	partial melting source term for F	—	s^{-1}
$H(z, t)$	non-dimensional radiogenic heat generation	—	—
H_0	reference value radiogenic heat generation	5.33×10^{-6}	Wm^{-3}
Φ	viscous dissipation: $2\eta e^2$	—	Wm^{-3}

Table 2.1: Explanation of symbols used.

symbol	definition	value	units
<i>i = 1: α-olivine to β-spinel</i>			
Γ_1	phase function (see Section 2.2.2)	–	–
γ_1	CC-slope $(dp/dT)_1$	3.112	$MPaK^{-1}$
$T_1^{CC}(p = 15.5 \text{ GPa})$	phase transition temperature at 15.5 GPa	2323.58	K
p_1	transition pressure at $T = 0 \text{ K}$	–	GPa
Δz_{Γ_1}	half-width phase-transition	10	km
ΔS_{Γ_1}	entropy change upon transition	-54.62	$Jkg^{-1}K^{-1}$
$\delta\rho_1$	α -olivine to β -spinel density jump	204.80	kgm^{-3}
X_1	volume fractional correction	0.5661	–
<i>i = 2: β-spinel to γ-spinel</i>			
Γ_2	phase function (see Section 2.2.2)	–	–
γ_2	CC-slope $(dp/dT)_2$	4.406	$MPaK^{-1}$
$T_2^{CC}(p = 20.5 \text{ GPa})$	phase transition temperature at 20.5 GPa	2452.35	K
p_2	transition pressure at $T = 0 \text{ K}$	9.695	GPa
Δz_{Γ_2}	half-width phase-transition	5	km
ΔS_{Γ_2}	entropy change upon transition	-33.69	$Jkg^{-1}K^{-1}$
$\delta\rho_2$	α -olivine to β -spinel density jump	89.23	kgm^{-3}
X_2	volume fractional correction	0.5525	–

Table 2.2: Solid-state phase-transition parameters.

$\vec{x} \cdot \frac{1}{h}$	$= \vec{x}'$	$p \cdot \frac{h^2}{\eta_0 \kappa}$	$= p'$
$\vec{u} \cdot \frac{h}{\kappa}$	$= \vec{u}'$	$\pi_i \cdot \frac{h^2}{\eta_0 \kappa}$	$= \pi'_i$
$T \cdot \frac{1}{\Delta T}$	$= T'$	$\gamma_i \cdot \frac{h^2 \Delta T}{\eta_0 \kappa}$	$= \gamma'_i$
$t \cdot \frac{\kappa}{h^2}$	$= t'$	$\tau \cdot \frac{h^2}{\eta_0 \kappa}$	$= \tau'$

Table 2.3: Non-dimensionalization scaling factors.

symbol	definition	formula	value
\mathcal{R}	internal heating number	$H_0 \cdot \frac{h^2}{\kappa \Delta T}$	318.4
Di	dissipation number	$\frac{\alpha g h}{c_p}$.1970
Ra	thermal Rayleigh number	$\frac{\rho_0 \alpha \Delta T g h^3}{\kappa \eta_0}$	664.5×10^3
Rb	compositional Rayleigh number	$\frac{\delta \rho g h^3}{\kappa \eta_0}$	666.1×10^3
Rb_{Γ_1}	Rb for solid state phase transition 1	$\frac{\delta \rho_1 g h^3}{\kappa \eta_0}$	603.6×10^3
Rb_{Γ_2}	Rb for solid state phase transition 2	$\frac{\delta \rho_2 g h^3}{\kappa \eta_0}$	263.0×10^3

Table 2.4: Non-dimensional scaling coefficients.

2.2.3 Rheological model

The ductile deformation of upper mantle peridotite is described by a linear stress–strain-rate relation. The strength of the upper material is therefore given by a Newtonian viscosity. The upper mantle consists of approximately 60 weight-% olivine (Ringwood 1982). Since olivine is also the weakest of the different minerals in upper mantle peridotite (Ranalli 1986), the upper mantle can be approximated by an olivine rheology.

We adopt an Arrhenius type of temperature- and pressure-dependent viscosity relation (Ranalli 1991):

$$\eta_m(p, T) = \mathcal{B}(F) \cdot \exp\left(\frac{E + pV}{RT}\right) \quad (2.15)$$

where symbols are defined in Table 2.1. The pre-factor $\mathcal{B}(F)$ values given in Table 2.1 correspond to a viscosity value of $\eta = \eta_0 = 10^{21}$ *Pa s* at a depth of 400 *km* ($p = 13.39$ *GPa*) and a temperature of 1750°C. In addition, the pre-factor can contain a F -dependency (see Section 4.2).

The constant high viscosity of the crust is also the maximum allowed viscosity η_{max} applied in the models. A smooth truncation of the mantle viscosity is used by taking the harmonic average, which yields for the effective dimensioned viscosity:

$$\eta(p, T) = \left[\frac{1}{\eta_m} + \frac{1}{\eta_{max}} \right]^{-1} \quad (2.16)$$

2.2.4 Conservation equations

We apply the Extended Boussinesq Approximation (EBA) to formulate equations for the conservation of mass, energy and momentum. For the application to the Earth's upper mantle, inertial forces may be neglected (infinite-Prandtl-number fluid). Conservation of mass and momentum are given by:

$$\nabla \cdot \vec{u} = 0 \quad (2.17)$$

$$\nabla \Delta p = \nabla \cdot (\eta(\nabla \vec{u} + \nabla \vec{u}^T)) - \Delta \rho(T, F, \Gamma) g \hat{z} \quad (2.18)$$

The relation for conservation of energy is:

$$\rho_0 c_p \frac{dT}{dt} - \alpha \frac{dp}{dt} T = k \nabla^2 T + H + \tau \cdot \nabla \vec{u} - \rho_0 \Delta S \frac{dF}{dt} T - \rho_0 \sum_{i=1,2} X_i \Delta S_{\Gamma_i} \frac{d\Gamma_i}{dt} T \quad (2.19)$$

Neglecting mass diffusion for the conservation of composition yields:

$$\frac{D F}{Dt} = \mathcal{P}(p, T, F) \quad (2.20)$$

where \mathcal{P} is the source term of F related to the melt productivity (see Appendix A). A similar equation for the advection of the crustal layers is valid:

$$\frac{DC}{Dt} = 0 \quad (2.21)$$

where C defines the initial position of a crustal volume. No source or sink terms are incorporated since processes related to such terms (e.g. crustal growth and crustal erosion) are not explicitly incorporated in the model.

Applying the non-dimensionalization factors given in Table 2.3 and dropping primes, the Equations 2.18 and 2.19 take the following non-dimensional form:

$$\nabla \Delta p = \nabla \cdot (\eta(\nabla \vec{u} + \nabla \vec{u}^T)) - RaT\hat{z} - RbF\hat{z} + \sum_{i=1,2} X_i Rb\Gamma_i \Gamma_i \hat{z} \quad (2.22)$$

where the EOS (Equation 2.3) has been substituted in the Stokes equation (Equation 2.18). Similarly, we find for the energy equation (Equation 2.19):

$$\frac{dT}{dt} - Di(T + T_0)w = \nabla^2 T + \mathcal{R}H + \frac{Di}{Ra} \Phi - \frac{\Delta S}{c_p} \frac{dF}{dt} (T + T_0) - \sum_{i=1,2} \frac{X_i \Delta S \Gamma_i}{c_p} \frac{d\Gamma_i}{dt} (T + T_0) \quad (2.23)$$

The non-dimensional coefficients are given in Table 2.4.

2.3 Model assumptions and approximations

Explicit formulations for melt storage and segregation are not incorporated in the equations that describe the continental upper mantle model. It is assumed that the generated melt is instantaneously extracted from the residual mantle rock. This implies that the equations describing the two-phase flow of solid residue and liquid melt as given in (McKenzie 1984) reduce to single flow equations for the residual matrix. The problems and implications that arise in the thermo-dynamics of melt segregation are studied by others (Spiegelman 1993a; Spiegelman 1993b; Spiegelman 1993c; Ogawa 1993; Kameyama et al. 1996; Schmeling 1999) and not discussed in this thesis.

The use of the EBA implies that compaction upon melt segregation cannot be operative in the model. Thus the volume of depleted mantle rock is overestimated in the model. A modelled elementary volume of depleted mantle rock has generated a volume of melt that corresponds to its degree of depletion and is given by the porosity:

$$\phi = \frac{F \rho_s(F)}{\rho_f + F(\rho_s(F) - \rho_f)} \quad (2.24)$$

A first order approximation for this equation is $\phi = F$, which follows from stating $\rho_f = \rho_s(F)$.

Applying this approximation to the obtained results described in Part II gives a first order indication of the overestimated volume of depleted material. The continental root as modelled here has an average degree of depletion of $F = 20\%$. This illustrates that the modelled continental root thicknesses will reduce to 80% of their modelled value. In terms of an average depth extend of about 250 km including an average crustal thickness of 50 km, the depth extend is reduced to 210 km.

Chapter 3

NUMERICAL METHODS

3.1 Introduction

The model equations introduced in Chapter 2 have been solved numerically. For the Stokes equation and the energy equation finite element methods were used on a mesh of triangular elements. Quadratic 6-point elements were used for the velocity field in the Stokes equation. A subdivision of the 6-point triangular elements into 4 linear 3-point elements was applied for the energy equation (Van Den Berg et al. 1993; Van Keken 1993). The transport equations for the degree of depletion F and the crustal layer were solved using a characteristics based method. The complete set of equations have been integrated in time using a Predictor–Corrector scheme for the time-dependent energy equation (Van Den Berg et al. 1993) which has been extended with the time-dependent transport equations. In the following, the different numerical treatments of the separate equations are discussed.

3.2 Energy equation

The energy equation (Equation 2.23) is solved on a finite element mesh constructed of linear triangular elements. The semi-discretized form of the energy equation is:

$$\mathbf{M} \frac{\partial \mathbf{T}}{\partial t} + \mathbf{S} \mathbf{T} = \mathbf{R} \quad (3.1)$$

Incorporating the physics described in Section 2.2 results in a time-dependent mass matrix \mathbf{M} , stiffness matrix \mathbf{S} , and right-hand-side vector \mathbf{R} . Furthermore, it can make the equation non-linear. This non-linearity in \mathbf{M} , \mathbf{S} and \mathbf{R} originates from the latent heat terms. In addition, adiabatic compression, radioactive decay of heat sources, and advection results in time-dependent \mathbf{M} , \mathbf{S} and \mathbf{R} . The precise contributions of these different aspects of the physics, that are contained in the non-dimensional Equation 2.23, to the matrices \mathbf{M} , \mathbf{S} and \mathbf{R} are described in Appendix B.

To increase the numerical stability at locations where the advection rates are high relative to the thermal diffusion, Streamline Upwind Petrov–Galerkin (SUPG) (Hughes and Brooks 1979) has been applied in some cases. We use a time-dependent type of SUPG (Segal and Praagman 1995) which makes \mathbf{M} dependent on the convective velocity and therefore time-dependent. Furthermore, the SUPG technique makes \mathbf{M} non-symmetrical. The use of SUPG techniques also effects the structure of \mathbf{S} .

Integration over a discrete time step $\Delta t = t^{(n+1)} - t^{(n)}$ yields for Euler backward used in the Predictor step:

$$\left[\frac{1}{2} (\mathbf{M}^{(n)} + \mathbf{M}^{(n+1)}) + \Delta t \mathbf{S}^{(n+1)} \right] \mathbf{T}^{(n+1)} \approx \left[\frac{1}{2} (\mathbf{M}^{(n)} + \mathbf{M}^{(n+1)}) \right] \mathbf{T}^{(n)} + \Delta t \mathbf{R}^{(n+1)} \quad (3.2)$$

For the Crank-Nicholson midpoint rule used in the Corrector step, the discretized form becomes:

$$\begin{aligned} [\mathbf{M}^{(n)} + \mathbf{M}^{(n+1)} + \Delta t \mathbf{S}^{(n+1)}] \mathbf{T}^{(n+1)} \approx & [\mathbf{M}^{(n)} + \mathbf{M}^{(n+1)} - \Delta t \mathbf{S}^{(n)}] \mathbf{T}^{(n)} \\ & + \Delta t [\mathbf{R}^{(n)} + \mathbf{R}^{(n+1)}] \end{aligned} \quad (3.3)$$

3.3 The Stokes equation

The discrete formulations of the Stokes equation (Equation 2.22) and the incompressibility condition are:

$$\mathbf{S}\mathbf{u} - \mathbf{L}^T \Delta \mathbf{p} = \mathbf{F} \quad (3.4)$$

$$\mathbf{L}\mathbf{u} = 0 \quad (3.5)$$

This set of equations is solved with the discrete penalty function method (Cuvelier et al. 1988; Van Keken 1993; Segal and Praagman 1995) in which the incompressibility condition is perturbed with a small term containing the pressure:

$$\mathbf{p} = -\frac{1}{\epsilon} \nabla \vec{u} \quad (3.6)$$

which after discretization becomes:

$$\Delta \mathbf{p} = -\frac{1}{\epsilon} \mathbf{M}_p^{-1} \mathbf{L}\mathbf{u} \quad (3.7)$$

where \mathbf{M}_p is the pressure mass matrix. Substitution of Equation 3.7 in Equation 3.4 gives:

$$\left(\mathbf{S} + \frac{1}{\epsilon} \mathbf{L}^T \mathbf{M}_p^{-1} \mathbf{L} \right) \mathbf{u} = \mathbf{F} \quad (3.8)$$

from which \mathbf{u} is solved.

3.4 Transport equation

The equation which describes the upper mantle compositional state of differentiation (Equation 2.20) is a transport equation including a source term. Crustal layers in the model also evolve according to a transport equation, but without sources or sinks (Equation 2.21). Furthermore, the evolution of several other physical quantities is monitored using tracer particles for which also transport equations with or without sources or sinks have to be solved. Two methods to solve the necessary transport equations are employed.

3.4.1 Characteristics based method

The method of characteristics (MoC) forms the framework of the technique that has been used to solve the transport equations. Chapter 6 describes the principles and possibilities of the method in more detail. Here, only a brief summary is given.

By combining higher and lower order interpolations into a hybrid scheme, an optimal balance can be found between accuracy and stability. Source terms are easily incorporated. Both the equations describing the mantle and crustal evolution are solved with this solution technique.

3.4.2 Tracer particle method

Tracer particles are used to monitor the evolution of single material points along their flow-characteristics.

When tracer particles are applied (Chapter 7), a single set of initially randomly distributed tracers in space is used to trace the evolutions of the following quantities: temperature, thermal age, and degree of depletion. Interpolation from the finite element meshes to this unstructured tracer distribution is done with the Particle in Cell (PIC) interpolation (Hockney and Eastwood 1988) and subsequential bilinear interpolation. The cells used for the PIC interpolation form a structured equidistant grid and the PIC interpolation results in values at the grid nodes. These values are then bilinearly interpolated onto the particles.

Tracers are transported along their characteristics which are determined with a fourth order Runge–Kutta scheme. The convective velocities are bilinearly interpolated from the linear 3-point triangular finite elements, which resulted from the subdivision of the quadratic 6-point triangular velocity elements (see Section 3.1).

3.5 Numerical time integration

Time integration of the four equations describing the dynamics of the model is done with a Predictor–Corrector (PC) scheme. First a summary is given of the external quantities that are present in each equation, and what quantity is solved from each equation:

	equation	Eq. #	external quantities ('input')	solved quantity ('output')
A	energy	(2.19)	\vec{u} dF/dt T $d\Gamma/dt$	T
B	transport/melting	(2.20)	\vec{u} F dF/dt T	F dF
C	crustal advection	(2.21)	\vec{u}	C
D	Stokes	(2.18)	T F Γ	\vec{u}

Here, the order in which the equations are solved is not subject of investigation. The original PC-scheme is followed as close as possible, which results in the following order applied in all modelling studies and is identical to the order used by Van Keken (1993):

Initial condition :

- Initial fields $T^{(n=0)}$, $F^{(n=0)}$ and $C^{(n=0)}$ are set from which the corresponding $\vec{u}^{(n=0)}$ is determined.

Predictor :

- A** First the energy equation is solved in the Predictor with the backward Euler method where we assume that at $t^{(n+1)}$ all external quantities have not changed since $t^{(n)}$. This results in a Predictor $T_\star^{(n+1)}$.
- B** Determine $F_\star^{(n+1)}$ and corresponding $\Delta F/\Delta t_\star^{(n+1)}$ using $T_\star^{(n+1)}$.
- C** Determine $C_\star^{(n+1)}$.
- D** Determine $\tilde{u}_\star^{(n+1)}$ using $T_\star^{(n+1)}$, $F_\star^{(n+1)}$ and $C_\star^{(n+1)}$.

Corrector :

- A** Determine $T^{(n+1)}$ using the Crank-Nicholson time integration scheme and all the Predictor fields.
- B** Determine $F^{(n+1)}$ and corresponding $\Delta F/\Delta t^{(n+1)}$ using $T^{(n+1)}$.
- C** Determine $C^{(n+1)}$.
- D** Determine $\tilde{u}^{(n+1)}$ using $T^{(n+1)}$, $F^{(n+1)}$ and $C^{(n+1)}$.

Monitored quantities :

- Quantities monitored by the tracer particles do not influence the dynamics and are therefore determined after all the updates for the fields at $t^{(n+1)}$ have been completed.

The integration time-step is controlled in two ways.

- The Courant–Friedrichs–Levi (CFL) criterion is applied (Van Den Berg et al. 1993). This results in a maximum time-step Δt_{CFL} of which a fraction is applied through a CFL-factor f_{CFL} :

$$\Delta t = f_{CFL} \cdot \Delta t_{CFL} \quad (3.9)$$

This factor is normally set to $0.5 < f_{CFL} < 0.6$, but in some cases a much higher value is applied. During the long term evolution a large factor of $f_{CFL} = 3$ was applied. This has been tested and only minor differences are observed, when the solution is compared with values obtained for $f_{CFL} = 0.5$. The reason for this is probably that also a second time-step criterion in the Predictor is applied:

- For each time-step the relative supremum norm between the $\mathbf{T}^{(n)}$ and $\mathbf{T}_\star^{(n+1)}$ was required to be less than ϵ_T . If this norm was larger than ϵ_T , the time-step $\Delta t^{(n+1)}$ was reduced with a factor $f_{\Delta t}^-$ and if the norm satisfied the criterion the next time-step $\Delta t^{(n+2)}$ grows with a factor $f_{\Delta t}^+$. The applied values are:

$$\begin{aligned} 0.6 &< f_{\Delta t}^- < 0.8 \\ &f_{\Delta t}^+ &= 1.1 \\ 1\% &< \epsilon_T < 2\% \end{aligned} \quad (3.10)$$

These chosen parameter values represent a reasonable compromise between accuracy and efficiency of the method.

Part II

Modelling results

Chapter 4

STABILITY AND GROWTH OF CONTINENTAL SHIELDS IN MANTLE CONVECTION MODELS INCLUDING RECURRENT MELT PRODUCTION

¹ **Abstract:** The long term growth and stability of compositionally layered continental upper mantle has been investigated by numerical modelling. We present the first numerical model of a convecting mantle including differentiation through partial melting resulting in a stable compositionally layered continental upper mantle structure. This structure includes a continental root extending to a depth of about 200 km. The model covers the upper mantle including the crust and incorporates physical features important for the study of the continental upper mantle during secular cooling of the Earth since the Archaean. Among these features are: a partial melt generation mechanism allowing consistent recurrent melting, time dependent non-uniform radiogenic heat production, and a temperature- and pressure-dependent rheology. The numerical results reveal a long term growth mechanism of the continental compositional root. This mechanism operates through episodic injection of small diapiric upwellings from the deep layer of undepleted mantle into the continental root which consists of compositionally distinct depleted mantle material. Our modelling results show the layered continental structure to remain stable during at least 1.5 Ga. After this period mantle differentiation through partial melting ceases due to the prolonged secular cooling and small-scale instabilities sets in through continental delamination. This stable period of 1.5 Ga is related to a number of limitations in our model. By improving on these limitations in the future this stable period will be extended to more realistic values.

4.1 Introduction

Several geodynamical scenarios exist which address the continental formation during the early evolution in the Earth (Jordan 1988; Anderson 1990; Vlaar et al. 1994). The stability of the continental root, differences between oceanic and continental lithosphere, the thickness of the continental lithosphere, and differences between old cratonic and younger continental lithosphere are some of the issues addressed by such geodynamical scenarios. Evidence for a specific continental configuration extending over several hundreds of kilometers in depth comes from different disciplines.

¹This chapter has been published in *Tectonophysics* (1998) V.296 pp. 15-29

Based on seismological observations, Jordan (1975) finds that present day lithosphere of old continental nuclei must be significantly cooler than recent oceanic lithosphere. This led him to the concept of the continental 'tectosphere'. An overview and discussion of evidence supporting the existence of the tectosphere is given by Jordan (1988) where it is argued that it extends to 250-400 *km* depth, depending on its age of formation. Other studies which discuss seismological observations concerning the structure of continental lithosphere (Anderson 1990; Polet and Anderson 1995) are in agreement with this observation, although the estimates of the depth extent of the cratonic root are smaller. Similar conclusions were drawn by Doin et al. (1996) on the basis of geoid inversions.

The concept of the continental tectosphere explains the long term stability of ancient (> 3 *Ga*) continental shield areas by compositional layering. In this model a layer of depleted mantle peridotite of lower intrinsic density lies on top of a layer of undepleted denser peridotite (Jordan 1978; Jordan 1988). Depleted peridotite is the residual material in the mantle differentiation process of pressure release partial melting, resulting in production and segregation of basaltic melt.

Geodynamical consequences for the evolution of the Earth of this differentiation process in an oceanic setting were investigated by Vlaar and Van Den Berg (1991), using a modification of the model by McKenzie (1984) for 1-D pressure release melting. In Vlaar et al. (1994) a more extended model was used to investigate the role of the upper mantle differentiation process in Earth's secular cooling. Particularly in Vlaar and Van Den Berg (1991) and Vlaar et al. (1994) it was demonstrated that in the early Earth when partial melting takes place at higher mantle temperature, a much thicker basaltic crust and corresponding thicker depleted peridotite layer are produced. This creates an intrinsically stable layering and conditions which do not favor a present day style of plate tectonics. In the present Chapter an extended formulation for partial melting not restricted to 1-D adiabatic conditions is applied to investigate how Archaean continental shields have evolved. We assume a higher mantle temperature consistent with secular cooling of the Earth since the early Archaean. This Chapter is focused on some of the major topics concerning the evolution of old continental shield. Among these are the stability, growth and cooling behaviour of the continental mantle. To this end we have used a numerical model for thermo-chemical mantle convection that includes mantle differentiation by means of partial melting. Our model is the first one exhibiting a convecting mantle with partial melting that produces a stable layering of lighter depleted peridotite on top of a fertile peridotite layer.

Alternative convection models have been applied to the upper mantle by different authors. Ogawa (1988, 1993, 1994) focuses on upper mantle differentiation in the context of the Earth's evolution. The model of Doin et al. (1997) includes an ad hoc continental region of which the stability is studied. The model of Lenardic (1997) is appropriate to study the variation of continental heat flow variations. Upper mantle differentiation in mantle convection has also been studied by Schmeling and Bussod (1996) for present day continental conditions.

The next section discusses the numerical model. The model incorporates important physical aspects which are necessary to study evolution of old continental lithosphere. This includes recurrent melting of partially depleted material, which is important to study possible growth mechanisms of the depleted continental root in a convecting mantle. According to Jordan (1988) two growth mechanisms can be responsible. The first is a process of steady internal depletion of the continental root. The second one adds depleted material from below. Which one of these, or possibly other mechanisms cause

the growth remains an unanswered question. At least one such mechanism, however, is required to stabilize the continental lithosphere during secular cooling. The modelling results presented illustrate clearly the different possibilities of active growth mechanisms and their relative importance. The model presented here includes the physics that covers both growth mechanisms, and from the modelling results their relative importance can be investigated. Thermal aspects are also discussed in this work, since they influence the stability of the tectosphere. To this end, several important thermal effects are incorporated: cooling due to adiabatic decompression, internal radiogenic heating, and directly connected to the melting process, the effect of latent heat consumption.

The combination of the consistent partial melting with the aforementioned thermal aspects, and a parameterization that is thought to be applicable to an Archaean continental situation results in a model that can explain how continental roots have grown during Earth's secular cooling and why they have remained stable in the process.

4.2 Model description and numerical method

The state of differentiation of the mantle is described by the degree of depletion expressed as the mass fraction F of the produced partial melt: $0 \leq F < 1$. A zero value of the degree of depletion corresponds to a pyrolite primitive upper mantle and a gradually increasing F corresponds to low degrees of partial melting resulting in a lherzolithic residue and for even larger values of F the residue is harzburgitic (Ringwood 1982). This compositional effect (Jordan 1979) is translated into a density effect which influences the gravitational stability of the system as shown by Vlaar and Van Den Berg (1991) and Vlaar et al. (1994). Including the effect of thermal expansion the linearized equation of state is

$$\rho(T, F) = \rho_0[1 - \alpha(T - T_{srf}) - F \delta\rho/\rho_0] \quad (4.1)$$

Symbols are defined in Table 2.1 and all quantities in Equation 4.1 are in dimensional form. We used a non-dimensionalization scheme described in Van Den Berg et al. (1993). In the following equations non-dimensional quantities are used unless explicitly stated otherwise. The equation of state defines the buoyancy force in the non-dimensional momentum equation through the thermal and compositional Rayleigh numbers Ra and Rb respectively. For an infinite Prandtl number fluid this yields

$$\nabla \cdot (\eta(\nabla \vec{u} + \nabla \vec{u}^T)) - \nabla \Delta p = (Ra T + Rb F) \hat{z} \quad (4.2)$$

where \hat{z} is the unit vector in the vertical direction aligned with gravity. The definitions of \vec{u} , Δp , Ra and Rb , and the values Ra and Rb are listed in Table 2.1.

We assume a Newtonian pressure- and temperature-dependent viscosity defined by an Arrhenius relation

$$\eta(p, T) = B(F) \cdot \exp \left[\frac{E + pV}{RT} \right] \quad (4.3)$$

where the temperature, pressure and viscosity are in dimensional form. The numerical values of the activation parameters E and V for dry olivine are taken from Ranalli (1991) and Karato and Wu (1993) and listed in Table 2.1. The pre-factor B contains the dependence on the degree of depletion F (see below) and is chosen such that at 400 km depth, 1750 °C and $F = 0$ the viscosity equals the reference viscosity $\eta = \eta_0 =$

10^{21} *Pa.s*. The top part of the model is a mechanical boundary layer (MBL) with a high viscosity lid. For numerical reasons we truncated the viscosity distribution near the cold top boundary at $\eta_{max} = 10^{24}$ *Pa.s*. The average mantle geotherm in the model results in a layer of minimum viscosity directly underneath this MBL. Such a rheological layering is also found in viscosity profiles derived from post-glacial rebound analysis (Lambeck et al. 1996). The stabilizing effect of the MBL is enhanced by the buoyant crustal layer of lower density ρ_c . Internal heating by radioactive decay is strongest in the crustal part, resulting in a thermal blanketing effect and slower cooling. The buoyant MBL prevents the gravitational collapse of the upper continental lithospheric part of the model during secular cooling. At greater depths the pressure dependence dominates over the temperature effect and hence the viscosity increases. This makes the deeper part of the upper mantle less mobile, restricting the mantle circulation to shallower depths in our model. We have investigated two different rheological models. In one model we assume the viscosity of the residual material to be larger than for undepleted rock, i.e. $B(F) = 5 \cdot B(0)$ when $F > 0$ in Equation (4.3). The model with F -dependent rheology is referred to as Model B and the model with uniform $B = B(0)$ is referred to as Model A.

We assume a simplified parameterization of the melting phase diagram with linear and parallel solidus and liquidus between which F is a bilinear function of p and T based on experimental data compiled by Jacques and Green (1980). The transport equation describing partial melting of a volume of mantle material in terms of the degree of depletion F is,

$$\frac{D F(p, T)}{Dt} = \frac{D f(\Theta)}{Dt} \quad (4.4)$$

where the right-hand-side describes a source distribution of partial melt production and Θ is a normalized super-solidus temperature further defined in Appendix A. A volume of partially melted material that is being recycled can only differentiate further when its Θ value is in excess of any previously reached value.

The energy equation based on the Extended Boussinesq Approximation (EBA) (Christensen and A. 1985; Steinbach et al. 1989; Ita and King 1994) is written in non-dimensional form using the non-dimensionalization scheme described in Van Den Berg et al. (1993),

$$\frac{dT}{dt} - Di(T + T_0)u_z = \nabla^2 T + \mathcal{R}H(\vec{x}, t) - (T + T_0) \frac{\Delta S}{c_p} \frac{dF}{dt} \quad (4.5)$$

where the viscous dissipation term is neglected and Di is the dissipation number defined in Table 2.1. Latent heat consumption by partial melting is represented by the last term. The term containing the dissipation number Di accounts for heating and cooling due to adiabatic (de-)compression. Taking this effect into account is essential in stability experiments. This is reflected in the fact that the critical Rayleigh number for Rayleigh-Benard convection is higher (Steinbach 1991) compared to the Boussinesq case with $Di = 0$.

We have used a non-uniform distribution of internal heat production with the maximum values in the crustal layer. Increased internal heating in the top layers results in a strong blanketing effect which in turn delays the cooling from the top. This increases the stability of the layering significantly.

The present day continental situation of the heat production in the 16 km thick upper crust initially follows $H(\vec{x}, 0) = H_0 \cdot \exp(-z/b)$ with $b = 30$ km and $H_0 =$

$2.67 \mu W m^{-3}$. In the lower crust up to 50 km depth a uniform $H_l = 0.45 \mu W m^{-3}$, and for undepleted mantle material a lower uniform productivity of $H_u = 0.045 \mu W m^{-3}$ is valid. Total segregation of melt as assumed in our model will remove most of the incompatible radiogenic elements and the value of H for this case is assumed to drop to $H_d = 0.02 \mu W m^{-3}$. Radiogenic heating is essential to establish a realistic continental geotherm. The values given above for H represent the present day situations of continental shields according to Chapman (1986). The upper crustal value is in agreement with O'Connell and Hager (1980). Estimations of H applicable to the Archaean era vary from 2 to 3 times the present day value. We have applied the lower bound in our model. Multiplying all the above given figures by two yields $H_0 = 5.33$, $H_l = 0.9$, $H_u = 0.09$ and $H_d = 0.04 \mu W m^{-3}$. The choice of the value of 2 for the radioactive decay factor results in an underestimation of the Archaean radiogenic heat production.

Melt segregation due to mantle differentiation is the prime cause for the non-uniform heat production as described above. Since the influence of this process on separate radioactive isotopes is rather uncertain, and isotope concentrations are not precisely known for the Archaean era, multiplication of each layer separately by the same factor of two gives only an approximation of the Archaean distribution. Furthermore, there are many other uncertainties, such as the amount of erosion and the parameter b and the isotope dependent radioactive decay constant λ , which also influence the validity of this extrapolation. The effective radioactive decay constant is set to $\lambda = .347 Ga^{-1}$ (Turcotte and Schubert 1982). When the melt is expelled, it is removed from the model and is not added to the crustal mass. This implicitly assumes that erosion balances the melt production and that the crustal heat generation is not affected by these processes.

The momentum and energy equations are solved with a finite element method (Van Den Berg et al. 1993) and a time dependent upwind scheme (SUPG) (Segal 1982; Hughes and Brooks 1979) is applied to the latter to improve numerical stability in advection dominated regions of the domain. The transport equation for F is solved using a method of characteristics on a mesh much denser than the finite element mesh. A fourth order Runge-Kutta integration scheme is applied in combination with a hybrid interpolation scheme. Bilinear interpolations (Sotin and Parmentier 1989; Sparks and Parmentier 1993) form one part of this hybrid scheme. The other part consists of bicubic spline interpolations (Ten et al. 1996). Equations (4.2), (4.4) and (4.5) are solved in this order.

4.3 Numerical modelling results

We present modelling results for a rectangular domain with a depth of 670 km and an aspect ratio $a = 3$ corresponding to a width of 2010 km. The bottom boundary represents the interface between the upper and lower mantle. A zero heat flux condition is applied to the bottom boundary, resulting in an overestimated cooling rate for the model. The vertical boundaries are thermally isolated and the top of the crust has a fixed surface temperature T_{surf} . All boundaries are impermeable and a free slip condition is imposed on them. The two rheologically different models mentioned in the previous section have been investigated.

Initial condition

The purpose of our modelling experiments is to investigate the growth and the long

term evolution of a differentiated, layered continental upper mantle. Since the actual upper mantle conditions in the early Earth are largely unknown, we have constructed a dynamical initial condition for the time dependent model calculations.

The dynamical initial condition is created in the following way: the model equations (4.2) and (4.5) are integrated in time for a duration of several hundred million years for an undifferentiated mantle. In this start-up run, partial melting is switched off and radiogenic heating is defined constant in time and purely depth dependent, i.e. $H = H(z)$. During this initial convection stage, a thermal state of the mantle develops which is determined fully by the distribution of heat sources and the boundary conditions. As a result a statistically stationary situation evolves with $F = 0$ throughout the model. When this situation is reached, mantle differentiation in the model is switched on and the thermo-chemical evolution starts. Radioactive decay is also started at this moment, which we will refer to as $t = 0 \text{ Ma}$.

As will be shown below, mantle differentiation starts rapidly after $t = 0 \text{ Ma}$ and after only a few million years a gravitationally stable, partially depleted layer has developed directly below the crust. This depleted layer then evolves with a much lower growth rate, driven by the secular cooling of the upper mantle. This observation suggests that transient effects due to the dynamical initial condition are limited in time to about 10 Ma . The evolution of the layered system which is relevant in the present context starts after this initial phase.

The initial crustal thickness of 50 km does not change during the computations since crustal accumulation of melt is not implemented in the model. The crustal layer is part of the MBL and as such it is allowed to deform mechanically under the influence of viscous stress resulting from the mantle convection currents. The crust has an important stabilizing effect on the layering of the uppermost mantle during the start-up run and after. The high internal heating of the crust results in a strong thermal blanketing effect. Furthermore, its low density and high viscosity prevents the relative cold boundary layer from gravitational collapse. Experiments with thinner crusts revealed the same configuration of a depleted mantle directly under this crustal layer. The major effect of a thinner lower crust is a reduction of the crustal blanketing effect due to the reduced radiogenic heat production in the lower crust. This would result in a slightly cooler geotherm and a reduction of the thickness of the depleted zone. However, this reduction of the thickness of the depleted zone is counteracted by the fact that the top of the depleted zone would be at a shallower depth. A more detailed description of processes which influence the crustal thickness such as erosion and melt accumulation are not included in our model. However, for reasons described above we expect the crustal thickness in the model to have a minor influence on the model evolution.

Global thermo-chemical evolution

An impression of how the mantle model evolves compositionally and thermally is given in Figure 10.1 for Model A. The depletion field F (left hand column) and the modified temperature field $T - \langle T \rangle_{hor}$ (right hand column), which is used to emphasize the small lateral variations in the temperature field with respect to the 1-D background temperature, are shown for three different time values. Contours of the stream function Ψ are also plotted. Black and white contours are used for positive and negative values of Ψ to distinguish the orientation of the flow field. The streamlines show a large-scale sluggish convection pattern below the zone of the depleted layer and a small-scale convection pattern decaying in time in the continental root. The small-scale

thermo-chemical convection pattern in the rapidly developing continental root during the initial formation phase is related to the dynamic initial condition discussed above. Figures 10.1.a1 and 10.1.b1 show that the vigor of convection throughout the upper mantle is strongly decreased after 71 Ma and that the bulk of the continental root already has developed. The low density root limits large-scale convection to the mantle underneath it.

Due to the mechanical boundary conditions, blobs of cold depleted material flow down at the vertical boundaries of the domain illustrated at the right hand boundary in Figure 10.1.b1 and 10.1.b2. This descending depleted material is absorbed in the deeper mantle as shown in the last pair of frames at almost 1 Ga (Figure 10.1.c). This artifact due to boundary conditions contaminates the development of the whole system, especially when aspect ratios smaller than two are used. The net effect of this contamination of the deep upper mantle is that the effective density contrast between continental root and under-laying mantle decreases, thereby also decreasing the gravitational stability of the layering in the presented model.

The temperature fields depicted in the right hand column of Figure 10.1 illustrate that cooling from the top slowly penetrates into the lower mantle. Some correlation between temperature and depletion F can be observed, for instance in cold blobs, slightly depleted, descending from the bottom of the depleted zone. This is most clearly depicted in Figure 10.1.b. An overall characteristic of Figure 10.1 is that of rapid growth of the continental root situated in the upper 200 km of the mantle.

Quantification of the global evolution

In Figure 4.1 time series of several global quantities are shown. The time-series begin with the start-up period of 300 Ma preceding $t = 0$ Ma during which the aforementioned dynamic initial condition evolves. This formation of a statistically stationary situation is clearly illustrated in the volume average temperature shown in Figure 4.1.b. This curve shows that the model reaches a statistically thermal equilibrium approximately 150 Ma before mantle differentiation is started at $t = 0$ Ma . Similarly the time series of the root mean square velocity (V_{rms}) shown in Figure 4.1.a fluctuates about a stationary state.

At $t = 0$ Ma mantle differentiation through partial melting is switched on in the model. As a result upwelling flows of low density depleted material develop rapidly starting the growth of the depleted zone below the crust. These ascending and differentiating upwellings are accelerated in their upward motion due to the fact that the compositional buoyancy dominates the counteracting effect of cooling by latent heat consumption and adiabatic decompression. The spin-up in V_{rms} shown in Figure 4.1 during this initial stage lasts approximately 10 Ma . After the initial spin-up stage a layered system has evolved which represents a young Archaean configuration in our model.

Figure 4.1.a shows the strong effect of the density layering created during the spin-up stage on the convection dynamics. The vigor of convection is strongly reduced as a result of the increased internal stability of the layered system. The V_{rms} drops from a time averaged value of ~ 2 cm/a just before the start of the spin-up at $t = 0$ Ma to $V_{rms} \approx 0.4$ cm/a afterwards. The volume averaged temperature $\langle T \rangle$ in Figure 4.1.b shows a small but sharp decrease at $t = 0$ Ma due to the consumption of latent heat during the spin-up phase. After the spin-up phase a gradual decrease of the upper mantle temperature occurs of approximately 250 K during the 1.5 Ga time window.

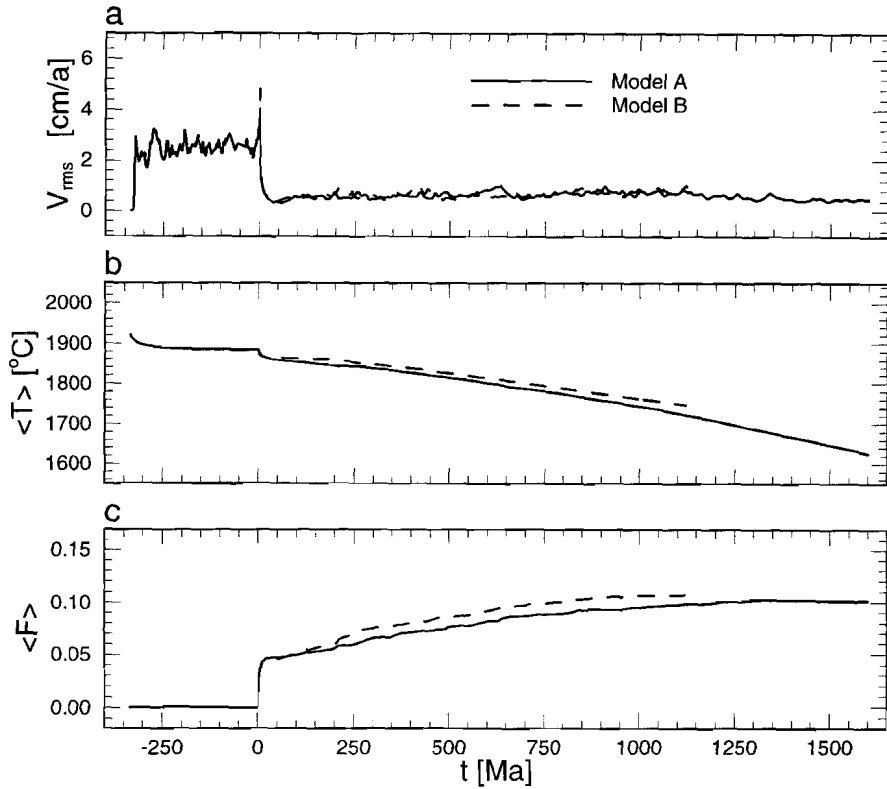


Figure 4.1: Time series of volume averaged quantities for Models A (solid lines) and B (dashed lines); **a** The root-mean-squared velocity, **b** The volume averaged temperature, and **c** The volume averaged degree of depletion. During the first 300 *Ma* shown ($t < 0$ *Ma*) the statistically stationary dynamical initial condition evolves. At $t = 0$ *Ma* mantle differentiation is allowed to start in the model resulting in a transient spin-up phase with a duration of almost 10 *Ma*.

No dramatic events occur during the evolution of the system as shown by the quantities depicted in Figure 4.1. Catastrophical root collapses would cause other spin-ups probably accompanied by massive melting. The continental root remains stable during the observed time-span.

The volume average degree of depletion $\langle F \rangle$ shown in Figure 4.1.c is slowly increasing after the initial spin-up. Figure 4.1.c shows a steep increase of $\langle F \rangle$ during the spin-up phase (i.e. up to $t \approx 10$ *Ma*) when the continental root is formed. Within this period there is a rapid increase in volume of depleted material positioned just below the crust as is depicted in Figure 10.1.a1.

From the different traces in Figure 4.1 it can be concluded that the transient effect of the dynamic initial condition decays rapidly in approximately 10 *Ma*. After this initial start-up phase a stable growth of the layered continental upper mantle system continues throughout the observed time-span.

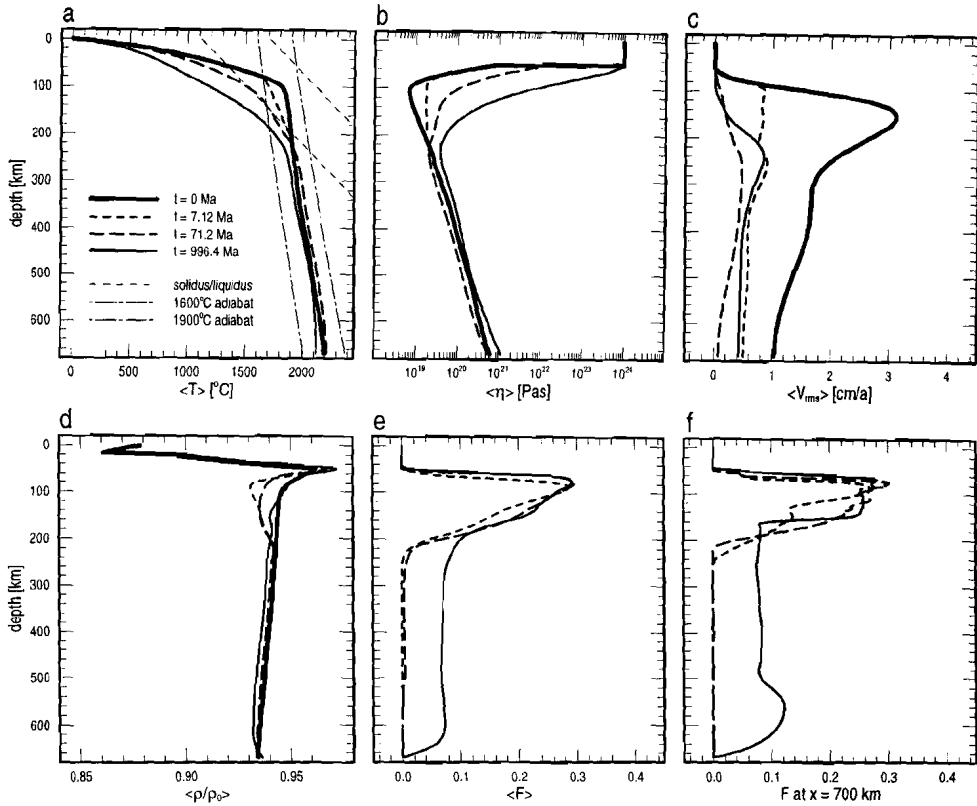


Figure 4.2: Horizontally averaged profiles (a-e) and vertical cross-sections (f) for different time values for Model A. **a** Horizontally averaged geotherms. The dash-dotted lines are adiabats for the potential temperatures indicated. The dashed lines are the solidus (for $F = 0$) and liquidus lines. Surface heat flows are $150, 137$ and 107 mWm^{-2} for $t = 7.12 \text{ Ma}$, $t = 71.2 \text{ Ma}$ and $t = 996.4 \text{ Ma}$ respectively. **b** Averaged viscosity profiles; Note the slowly growing MBL. **c** Averaged V_{rms} profiles, **d** averaged effective normalized density profiles clearly illustrating the density inversion in the continental root, decaying in time. **e** Averaged F , and **f** specific profile at given x ; The profiles at $t = 0 \text{ Ma}$ are not shown for clarity.

Layering and stability

Figure 4.2 shows the depth distribution of several horizontally averaged quantities and vertical cross-sections at different time values. Averaged geotherms are shown in Figure 4.2.a, together with the solidus and liquidus used in our model. The initial temperature distribution appears to be above the solidus temperature in the depth range between the bottom of the crustal layer and 200 km depth. At later time values this depth range decreases and after about 100 Ma the average geotherm is completely below the solidus. From about $t = 100$ Ma on, melting only occurs in regions with a positive temperature deviation from the horizontally averaged background geotherm, such as hot upwelling diapirs.

Figure 4.2.b shows horizontally averaged viscosity profiles for the same time values. The location of minimum viscosity shifts to greater depths as secular cooling proceeds, illustrating the growth of the MBL which is an important factor in stabilizing the cold top boundary layer. The horizontally averaged root mean square velocity $\langle V_{rms} \rangle_{hor}$ is displayed in Figure 4.2.c. Below the strong lid of the high viscosity crust the $\langle V_{rms} \rangle_{hor}$ increases rapidly in the low viscosity region at $t = 0$ Ma. The velocity in this region decreases rapidly after $t = 0$ Ma both because of the increase in viscosity due to cooling from the top and also because of the rapid formation of the low density depleted layer. At larger time values the location of maximum $\langle V_{rms} \rangle_{hor}$ shifts downward with the location of minimum viscosity.

Figure 4.2.d shows the horizontally averaged effective density distribution $\langle \rho(T, F) \rangle_{hor}$. After $t = 0$ Ma a strong density inversion develops due to the lighter depleted material accumulating at shallow depths. This density inversion is an important factor in the initial stabilization of the layering. For larger time values the density increases due to cooling from the top. High internal heating in the buoyant crust causes a thermal blanketing effect which slows down the cooling of the shallow layering. For later stages in the evolution the increase in viscosity shown in Figure 4.2.b prevents the collapse of the gravitationally unstable layering.

Horizontally averaged values of F and a vertical cross-section at $x = 700$ km of the degree of depletion are shown in Figure 4.2.f and 4.2.g. These figures illustrate the rapid development of the depleted zone from $F = 0$ at $t = 0$ Ma to $t = 70$ Ma in the region between the crust to a depth of about 200 km. The finite values of F in the deeper part of the model at $t = 1$ Ga are related to the absorption of depleted material, originating from downwellings at the vertical boundary illustrated in Figure 10.1. The detailed fine-scale layered structures in the depleted region shown in the profile of Figure 4.2.f are in part remnants of the vigorous partial melting stage during the spin-up phase directly following $t = 0$ Ma. Some of the structures, however, are directly caused by the active ongoing growth process of the depleted zone. An illustration of this is given below.

The onset of instability, continental delamination

After approximately 1.5 Ga the character of the evolution changes. Gravitational instability due to cooling from the top is increasing. At the same time partial melting has stopped because upwelling flows in the convecting undepleted zone no longer cross the solidus due to the general temperature decrease illustrated by the 1 Ga geotherm in Figure 4.2.a. As the effective density contrast between the depleted zone and the layer beneath diminishes, large downwellings from the lower part of the depleted zone start to develop. Apparently the still growing MBL is no longer strong enough to prevent the

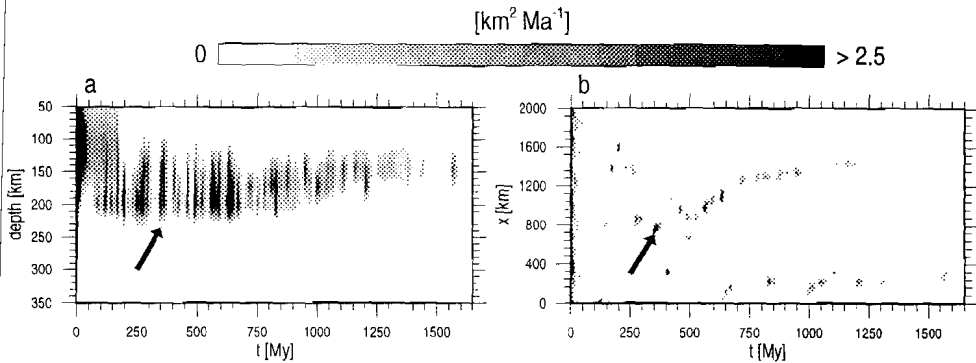


Figure 4.3: 1-D depth (a) and horizontal (b) distribution of melt production for Model A as a function of time. The black arrows point to the partial melting event that is studied in more detail in Figure 10.2.

increasingly unstable layering from collapse. However, these continental delaminations do not trigger any catastrophic events, such as upper mantle overturns, as is illustrated by the stationary character of the time series of the V_{rms} in Figure 4.1. The delamination process cannot be studied in greater detail in our modelling results due to the lack of numerical resolution at greater depths. Because of this, numerical diffusion becomes too strong in the deeper regions, which induces that the downwellings are smoothly integrated in the deeper part of the upper mantle. Hence, higher grid resolutions must be used to study the phenomenon of delamination. The delamination of the deepest part of the depleted layer as observed in our model is a smaller scale phenomenon than the one described by Pari and Peltier (1996).

Growth mechanism of the continental root

Figure 4.3 shows the melt production rates integrated over the width of the domain (4.3.a) and depth (4.3.b) respectively as a function of time. Figure 4.3.a shows that the depth range where partial melting occurs is between 110 and 240 km. The decrease in melt production amplitude shown in Figure 4.3.a is caused by the secular cooling of the mantle. Figure 4.3.a also shows that this decrease is accompanied by a narrowing of the depth range where melting occurs. The maximum depth where melting still occurs decreases when the mantle cools, which is in accordance with previous studies (Vlaar and Van Den Berg 1991; Vlaar et al. 1994). Both Figure 4.3.a and Figure 4.3.b indicate that the melting process has a pulsating nature. Small localized events that last for no longer than 50 Ma which have a lateral extent of approximately 100 km produce most of the depleted continental root. The upwellings in the large-scale time dependent convection pattern below the depleted zone are located where the events of melt production show horizontal allignments in Figure 4.3.b. The arrows in Figures 4.3.a and 4.3.b point to a single event which we have isolated for a more detailed investigation. This event is representative for the other episodic occurrences of partial melting.

Figures 10.2.a1-d1 show a time-sequence of blow-up snapshots of the degree of depletion together with flow patterns indicated by the contours of the instantaneous stream-function field. The corresponding modified temperature fields are given in Figures 10.2.a2-d2 together with several selected isotherms defined in the figure caption.

At the bottom of Figure 10.2.a1 a small diapir with a low degree of partial melting appears at a depth of about 210 km at $x=685$ km. This small feature originates from the undepleted mantle and collides with the depleted layer. Vertical profiles through the center and the tail of this diapiric upwelling are given in Figure 10.2.a3 and 10.2.a4 for F and T respectively at the x -coordinate printed in the figure and indicated by the dashed vertical white line in the first two columns. The compositional buoyancy which increases due to melting in the head of the diapir facilitates the penetration into the continental root (compare Figure 10.2.a1-a4 with 10.2.b1-b4). After a fast initial ascent the diapir becomes stagnant (compare Figure 10.2.b1-b4 and 10.2.c1-c4). This stagnation is a combined effect of the increased viscosity of the MBL at shallower depth and the decrease in degree of depletion contrast of the diapir with its environment. The high temperature feature in the upper right corner of Figure 10.2.a2 is the remnant of an older diapir which stagnated in this position as described above.

In the temperature profiles of Figure 10.2.a2-d2 the location of maximum deviation from the (dashed) solidus can be seen to move upward with the diapiric head, illustrating the ongoing melt production during the ascent and after stagnation. Note that the diapiric head produces a mushroom shaped thin depleted layer at a depth of approximately 100 km (Figures 10.2.d1 and 10.2.d3) and that the tail of the diapir has also been subject to partial melting resulting in an almost linear vertical depletion profile (Figures 10.2.b3-d3).

Internal circulation of differentiated material within the depleted zone does not generate new melt in significant amounts. This is because in order to allow recurrent melting, the super-solidus temperature of mantle material (defined in the Appendix A) must be brought to a higher value than the maximum value it has experienced previously. This process of recurrent melting does not seem to be significant in a depleted zone subject to secular cooling. This means that the growth of the continental root in our model takes place almost exclusively through the growth of the depleted zone by the addition of depleted material derived from upwelling fertile material in the slowly convecting layer beneath the depleted zone. This process takes place in an episodic way as illustrated in Figures 4.3 and 10.2

Effects of F -dependent rheology

Model B is characterised by a rheology which depends on the degree of depletion through the viscosity pre-factor $\mathcal{B}(F)$. Time series of global averaged quantities for this model are shown as dashed lines in Figure 4.1. At about 200 Ma a downwelling of depleted material develops at the vertical boundary causing an upward return flow which generates the sudden increase in the volume averaged value of the degree of depletion shown in Figure 4.1.c. The higher viscosity of the depleted material decreases its mobility and the convective heat transport through the layer. As a result the volume averaged temperature shown in Figure 4.1.b is slightly higher than in Model A. This reduced cooling rate of Model B does not influence the principle growth process of the continental root.

The overall characteristics of this model differ only slightly from Model A where the rheology is independent of the degree of depletion F . No onset of continental delamination was observed in the 1 Ga time window of the model calculations. It can be expected that this onset will be delayed with respect to Model A due to the higher viscosity of the depleted zone and the related reduced rate of secular cooling.

4.4 Discussion

The modelling results show that a compositionally layered structure rapidly develops that will remain stable over long periods of time. After sufficiently long time, however, secular cooling results in gravitational instability and continental delamination. In Model A delamination sets in after a period of time t_d about 1.5 *Ga*. The value of t_d is related to several approximations made in the model. The zero heat flux condition applied at the depth of 670 *km* results in a secular cooling rate which is too high. Furthermore, the solidus temperature in the simplified melting phase diagram used overestimates the real solidus temperature to an increasing extent for increasing depth or pressure. This results in an underestimated amount and duration of the mantle differentiation. In future work we plan to improve our model in order to eliminate these limitations and obtain more realistic evolution time-scales for the continental upper mantle.

Most observational evidence on the thickness of old continental roots comes from seismology and this evidence can be compared with our findings. In Figure 4.2.d a compositionally distinct root up to 200 *km* is shown which is in reasonable agreement with the depth of the drop in the seismic shear velocity between 170 and 200 *km* given by Anderson (1990). According to some authors (Jordan 1988; Polet and Anderson 1995) and the compositional layer that forms the continental root may be thicker. We expect that such depth extends larger than 200 *km* of the root will occur in our model when a more accurate solidus and liquidus parameterization is applied (Takahashi 1990; Vlaar et al. 1994).

The continental root growth mechanism in our model is an episodic diapiric process which results in a small-scale shallow layering (see Figure 4.2.e) which might explain seismic reflections from the shallow part of the continental upper mantle below the Moho discontinuity. These reflections could be associated with the remnants of mantle melting events (Flack and Warner 1990). Melt segregation to a higher level or melt trapped in the mushroom shaped diapiric heads can form layers which may act as good reflectors. Best (1991) describes such a reflecting zone at approximately 72 *km* depth beneath the Archaean terrain of the Montana Great Plains. The highlighted diapir in Figure 10.2 reaches a depth of near 100 *km* (Figure 10.2.d3), which suggests that these seismic reflections may be related to such an ancient event.

The size of the diapiric events appear to be small compared to events responsible for the generation of outbursts of flood basalts. The diapir highlighted in Figures 4.3 and 10.2 is one of the greater occurrences of melt generation and the amount of melt that is generated by this upwelling feature was estimated at 170000 *km*³. This estimate is based on the assumption that the width in the *x*-direction equals the width perpendicular to the 2-D model. Volume estimates of the smaller flood basalts start at approximately 750000 *km*³ and the generated volumes for the larger outflows are estimated at several millions of cubic kilometers (White and McKenzie 1989; Farnetani and Richards 1994).

A more quantitative comparison of the studied models can be made through the observed surface heat flow data. Heat loss through the top of the crust decreases from approximately 130 *mWm*⁻² during the early stages for Model A, to approximately 100 *mWm*⁻² after 1 *Ga* evolution. These are reasonable values since they are consistent with observational data. A present day value for old cratons is about 50 *mWm*⁻² and 80 ± 20 *mWm*⁻² for younger continental shields (Vitarello and Pollack 1980; Chapman 1986; Pollack, Hurter, and Johnson 1993). The present model results are best compared to the heat flow data for younger continental crust, which have not been subject to

secular cooling as long as the present-day Archaean shields. The values found from the models do not have any contribution from the lower mantle. Hence, the heat flow values found are lower bounds.

Finally, a restriction of the presented models is that they incorporate an isolated continental environment. Therefore, extrapolation of the thermal evolution from the present models to the whole Earth is not straight forward, since oceanic evolution is known to have different characteristics. Influence of ocean-continent interactions at shallow and deep levels are thus excluded from the present discussion.

4.5 Conclusions

The results of our modelling experiments have shown that stable continental structures with a compositional root can exist over long periods of time ($> 1.5 Ga$). This long term stability results from the density gradient related to the degree of depletion in the continental root. Also the temperature- and pressure-dependent rheology is important in preventing the continental root from collapse during secular cooling.

Potential temperatures in the model of the Archaean continental mantle were found to be in the range of $1700 < T_{pot} < 1900$ °C. These values proved to be sensitive to characteristics of the layering, in particular to the rheology of the depleted zone.

The continental growth process is an essential ingredient for continental lithospheric stability. In fact, stability comes to an end in our model when cooling from the top has brought the averaged geotherm below the peridotite solidus and mantle differentiation by partial melting stops. The evolution time-scale $t_d = 1.5 Ga$ found from our models, corresponding to the onset of continental delamination should be considered as a lower bound for the following reasons. First, the thermal coupling between the upper and lower mantle has been neglected in the model resulting in an overestimation of the secular cooling. Second, the parameterization of the melting phase diagram uses simple linearized versions of the solidus and liquidus of mantle peridotite. This in turn minimizes the amount of melt produced and the duration of melt production during secular cooling. A more realistic parameterization of the solidus and liquidus will result in melting in a wider depth range and over a longer time period during secular cooling. This in turn would result in a thicker and further differentiated continental root, which would extend to greater depths. This is in line with depths of 300 km found in Polet and Anderson (1995) and Jordan (1988).

Chapter 5

THE EVOLUTION OF CONTINENTAL ROOTS IN NUMERICAL THERMO-CHEMICAL MANTLE CONVECTION MODELS INCLUDING DIFFERENTIATION BY PARTIAL MELTING

¹ **Abstract:** Incorporating upper mantle differentiation through decompression melting in a numerical mantle convection model, we demonstrate that a compositionally distinct root consisting of depleted peridotite can grow and remain stable during a long period of secular cooling. Our modelling results show that in a hot convecting mantle partial melting will produce a compositional layering in a relatively short time of about 50 *Ma*. Due to secular cooling mantle differentiation finally stops before 1 *Ga*. The resulting continental root remains stable on a billion year time scale due to the combined effects of its intrinsically lower density and temperature dependent rheology. Two different parameterizations of the melting phase-diagram are used in the models. The results indicate that during the Archaean melting occurred on a significant scale in the deep regions of the upper mantle, at pressures in excess of 15 *GPa*. The compositional depths of continental roots extend to 400 *km* depending on the potential temperature and the type of phase-diagram parameterization used in the model. The results reveal a strong correlation between lateral variations of temperature and the thickness of the continental root. This shows that cold regions in cratons are stabilised by a thick depleted root.

5.1 Introduction

Continental nuclei are much older than oceanic lithosphere. Continents have cratonic segments with ages of 3.0 billion years and older (Condie 1984), in contrast with the oceanic lithosphere with ages up to about 200 million years (Müller et al. 1996). Thus, continents apparently form stable systems in the sense that they do not subduct. Oceanic lithosphere is subducting at ocean-continent boundaries, and this process is relatively well understood. The evolution of continental systems is much less clear. In this Chapter we present a model for the formation and long term evolution of continental systems within the frame-work of a numerical mantle convection model. There exists evidence for a specific continental configuration that extends to several hundreds of kilometers into the upper mantle. It has been suggested that the con-

¹This chapter is accepted for publication in *Lithos* (1998)

tinental lithosphere, also called the tectosphere (Jordan 1975), is a cold layer that is prevented from collapsing through a compositionally determined low intrinsic density. An overview of evidence supporting such a chemically distinct layer is given by Jordan (1988). Estimates of the depths of these chemically defined continental roots range from 200 – 400 km (Jordan 1975; Jordan 1988; Anderson 1990; Polet and Anderson 1995; Doin et al. 1996).

During the Archaean era the Earth had a hotter upper mantle because radiogenic heat production was higher and more initial heat from planetary formation and early differentiation was still stored in the Earth. It has been demonstrated that a hotter geotherm has a large effect on the depth where pressure release partial melting starts in the upper mantle (McKenzie 1984). This melting process results in residual material with an intrinsically lower density and a basaltic crust derived from the primary melt. This low density residual material is depleted peridotite or harzburgite and its presence can explain the long term stability of ancient, i.e. $> 3 Ga$, continental areas through gravitationally stable compositional layering.

The importance of a higher mantle temperature for the stability of oceanic and continental lithospheric systems has been discussed in Vlaar and Van Den Berg (1991) and Vlaar et al. (1994) who used simple models based on the 1-D adiabatic model for partial melting by McKenzie (1984). The results of these 1-D models showed that the present day style of plate tectonics cannot be extrapolated to the Archaean, since the compositionally differentiated layers produced by a convecting mantle, must have been much thicker during the Archaean. It was shown that a thick layer of harzburgitic residue underneath an also thicker crust must have led to a different thermo-chemical convection regime (Vlaar et al. 1994). In this Chapter we extend these earlier models of partial melting to non-adiabatic conditions within a thermo-chemical mantle convection model (Dupeyrat et al. 1995) (Chapter 4). We use a fully dynamical numerical mantle convection model including partial melting phase-diagrams based on empirical data. A similar model has been used in Chapter 4 and it has been further extended to investigate continental evolution. A new more realistic parameterization of the melting phase-diagram is incorporated in the present work allowing deep melting for a realistic young Earth continental geotherm. Here we apply this dynamic mantle differentiation model to investigate an upper mantle system subject to secular cooling in a continental setting and study in particular the formation and subsequent thermo-chemical evolution of the continental root.

Other workers have investigated continental systems in the context of mantle convection models. Effects of rheology have been studied by Moresi and Solomatov (1997) and Schmeling and Bussod (1996). Effects of Composition and rheology on delamination of a lithospheric root are studied by Schott and Schmeling (1998). Several authors use ad-hoc compositional layering of the continental upper mantle. Lenardic (1997) uses this type of model to explain surface heat flow data. Stability aspects are examined by (Doin et al. 1997). Long term evolutions for the whole upper mantle including partial melting are examined by Ogawa (1994) and Kameyama et al. (1996). Walzer and Hendl (1997) included the lower mantle in their study of mantle evolution with respect to the chemical differentiation of heat producing elements. The Hawaiin hotspot and rifting scenarios in relation with partially melting mantle plumes are studied by Ribe and Christensen (1994), Ebinger and Sleep (1998), and Leitch et al. (1998).

In the next section we present our model which focuses on the Archaean continental upper mantle. Incorporated are several important physical aspects, such as adiabatic compression, viscous heating, time and depth dependent radiogenic heat generation,

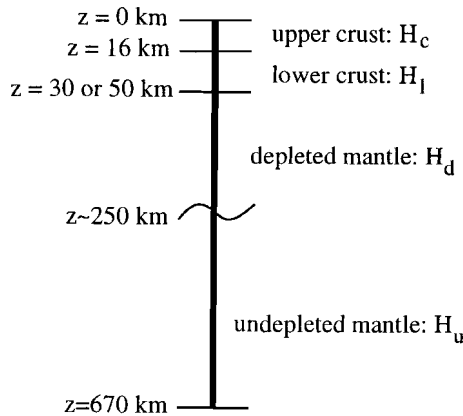


Figure 5.1: Schematic depth profile of the continental model with in the left-hand column depths in km . The upper and lower crust form a high density of viscosity layer with high radiogenic heat sources. The upper part of the mantle consists of a depleted layer up to approximately $250 km$ depending on the mantle temperature and in the present context also depending on the type of parameterization of the melting phase diagram (see Figure 5.2). This depleted layer has an intrinsically lower density ($\rho(F > 0) < \rho_s$) than the deeper undepleted part of the upper mantle ($\rho(F = 0) = \rho_s$).

latent heat consumption, and a pressure and temperature dependent rheology.

5.2 The model

We have applied a numerical convection model for the upper mantle including pressure release melting. A similar model with a different parameterization of the melting phase diagram was applied in Chapter 4.

5.2.1 Conceptual continental model

Figure 5.1 gives a schematic depth profile of the model. The model incorporates a crust of 30 to 50 km thickness overlaying the upper mantle to a depth of 670 km which is assumed to be mechanically decoupled from the lower mantle. The upper mantle consists of two layers: a deep lherzolithic layer of undepleted mantle peridotite and a more shallow harzburgitic layer with a variable degree of depletion. The depleted residual material is produced when the lherzolithic source material crosses its solidus and partial melting produces a melt fraction, which is assumed to be extracted instantaneously.

The process of partial melting also effects the distribution of radiogenic heat sources $H(\vec{x}, t)$. Figure 5.1 gives a schematic depth profile of the model distinguishing four layers with distinct values for $H(\vec{x}, t)$. The deeper undepleted mantle has an $H_u = 0.09 \mu W m^{-3}$, while the partial melting process reduces the value for the depleted layer to $H_d = 0.04$ or $0.0 \mu W m^{-3}$. This is due to the extraction of heat producing incompatible elements (Walzer and Hendel 1997). We used $H_l = 0.9 \mu W m^{-3}$ in the lower and $H_c = 4.13 \mu W m^{-3}$ in the upper crust. The values have been derived from the present day values given by O'Connell and Hager (1980) and Chapman (1986) by applying an amplification factor of two accounting for the mean radiogenic decay since the Archaean.

Estimations of Archaean radiogenic heat sources vary from two to three times the present day value. We have adopted the lower bound of this density range and included a decrease of productivity through the radioactive decay constant $\lambda = .347 \text{ Ga}^{-1}$, which corresponds to a half-life time of 2 Ga (Turcotte and Schubert 1982).

Model	crustal thickness [km]	thermal coupling upper/lower mantle	H_d [mWm^{-3}]	phase-diagram parameterization	initial geotherm
A	50	reservoir	0.04	linear	warm
B	50	isolated	0.04	polynomial	warm
C	30	isolated	0.0	polynomial	'cold'

Table 5.1: The differences between models A,B and C. The last column refers to the two initial geotherms given in Figure 5.2.a which are actually both warm and *cold* is meant in a relative way. The heat generation density for depleted material is given in column four (H_d). All model differences are discussed in Section *The model*.

Three different models A to C will be discussed. Model A and B have the heat generation parameterization mentioned above, whereas Model C has zero heat generation when the degree of depletion is larger than zero, i.e. $H_d = 0$ when $F > 0$. Both Models A and B have a crustal thickness of 50 km , whereas Model C has a reduced crustal thickness of 30 km . Further differences between the Models are discussed below and an overview of the model characteristics is given in Table 5.1.

The high crustal heat generation values result in a significant crustal blanketing effect. Since the model crust also has a low density ($\rho_c = 3000 \text{ kgm}^{-3}$) and a high viscosity ($\eta_{max} = 10^{24} \text{ Pas}$) it is stably situated on top of the continental mantle. Given the constant temperature at the surface (T_{surf}), the shallow geotherm in the mechanical boundary layer (MBL) at the top of the model is to a large extent determined by its heat source distributions.

In the deeper region the geotherm is influenced by several other factors. One of them is the compositional layering. The formation of a depleted low density layer impedes large scale convection and the formation of an adiabatic mantle geotherm at this depth level. An additional factor is the rheological parameterization including a strong temperature dependence of the viscosity. The effect of cooling from the top is a strong increase of the viscosity which gradually reduces the vigor of convection in the depleted zone which becomes stagnant from the top down.

We have used a Newtonian temperature and pressure dependent rheology. The viscosity model follows an Arrhenius relation which, in its dimensional form, is

$$\eta(p, T) = B \cdot \exp \left[\frac{E + pV}{RT} \right] \quad (5.1)$$

where values are given in Table 2.1 and the viscosity is truncated at its maximum value $\eta_{max} = 10^{24} \text{ Pas}$ which equates the crustal value. The viscosity pre-factor B is determined from the constraint that at $z = 400 \text{ km}$ and $T = 2023.15 \text{ K}$ (i.e. 1750°C) the viscosity equals the reference viscosity value 10^{21} Pas . In the present models we apply a stronger pressure dependence of the rheology, expressed in an activation volume of $V = 11.0 \mu\text{m}^3\text{mol}^{-1}$ compared to a $V = 7.5 \mu\text{m}^3\text{mol}^{-1}$ used in Chapter 4. Both numbers are in the range of possible values for the upper mantle (Ranalli 1991; Karato and Wu 1993). The increase of the pressure dependence increases the viscosity mainly in the deeper parts of the model, whereas at shallower depth the mobility increases

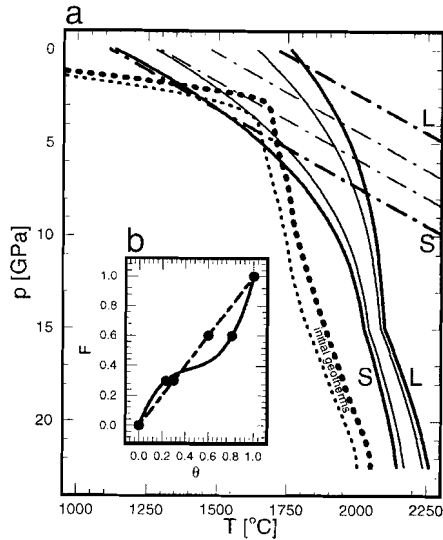


Figure 5.2: Parameterizations used in the models. **a)** The thick lines are the solidus and liquidus for the linear (dashed) and polynomial (solid) parameterization where *S* and *L* indicate the solidus and liquidus for both parameterizations respectively. The thinner lines correspond with phase equilibrium lines for which a degree of depletion is reached of 30 % and 60 %. The kink at 15 *GPa* corresponds to the phase transition that takes place at this depth. The thick dotted line is the initial geotherm at which melting is switched on at $t = 0$ for Models A and B. For Model C this is the thin dotted line. **b (inset)**, Degree of depletion (F) as function of normalized super-solidus temperature θ for the two models. The linearized curve (dashed) is a simplification of data given by Jacques & Green (1980) and corresponds with the dashed phase-lines of Figure 5.2.a. The bent curve (solid) is the third order polynomial fit as determined by McKenzie & Bickle (1988) and is used in the phase-diagram given by the curved phase-lines of Figure 5.2.a. The dots correspond to F -values of 0, 30, 60 and 100 % and for which the phase lines are given in Figure 5.2.a.

and the zone of minimum viscosity occurs at shallower depth ($z = 80$ km at $t = 0$ in the present Models A and B). This results in a thinner MBL and an overall decrease of the geotherm of about 175 K. We consider the reduced maximum temperature in the present models to be more representative for the young Earth. The horizontally averaged geotherm for $t = 0$ for Models A and B used here is depicted as the thick dotted line in Figure 5.2.a. The thin dotted line in Figure 5.2.a is the colder horizontally averaged geotherm corresponding to Model C. The difference is caused by the thinner crust in Model C.

In mantle peridotites subject to partial melting the solubility of water is higher in the basaltic melt fraction than in olivine. Furthermore, hydrous olivine has a lower viscosity than anhydrous olivine. Thus, basaltic melt extraction will increase the viscosity of the residual material (Karato 1990; Karato and Jung 1998; Hirth and Kohlstedt 1996). This effect can amount up to two orders of magnitude as estimated by Karato and Jung (1998). The influence of a modest increase in viscosity, i.e. the viscosity change from almost dry olivine to dry olivine, on the model has been investigated in Chapter 4. It stabilizes the root further and increases the thermal blanketing effect slightly.

The initial geotherm has been computed from the resulting temperature field obtained from a startup convection run. In this startup run, partial melting and the decrease of heat production in time are artificially switched off. After several hundred million years a statistically steady-state sets in, and a single snapshot of the temperature field of this

steady-state is used as an initial condition for a subsequent model run including partial melting and decrease of radiogenic heat production with time. We refer to Chapter 4 for a more extensive discussion.

5.2.2 Parameterization of the partial melting process

Mantle differentiation through partial melting is implemented in our model based on a melting phase-diagram for peridotite, which gives the equilibrium value of degree of depletion F for given values of p and T . In Chapter 4 we have used a simple parameterization of the phase-diagram, using linear and parallel curves for solidus and liquidus (Takahashi and Kushiro 1983). Here we also apply an improved parameterization based on a higher order polynomial fit of empirical data for the solidus and liquidus of mantle peridotite. Solidus and liquidus lines for both parameterizations are shown in Figure 5.2.a labeled with S and L , both the linear (dashed lines) and the polynomial (solid lines) parameterizations are shown.

Up to 15 GPa the curved solidus and liquidus are third order fits to data from Gasparik (1990) and Takahashi (1990) also used by Vlaar et al. (1994). For pressures in excess of 15 GPa a second order fit to the data from Ohtani et al. (1986) has been applied. The sample material used in both references are not identical and therefore a constant shift of about $-70 K$ has been applied to the data points from Ohtani et al. (1986) such that solidus and liquidus are continuous at $p = 15 GPa$. With $\vec{p} = (1, p, p^2, p^3)^T$ the parameterization used for the solidus is:

$$\begin{aligned} T_s(p) &= \vec{a}_s \cdot \vec{p} \\ \vec{a}_s &= (1136. , 134.2 , -6.581 , 0.1054)^T : p \leq 15 GPa \\ \vec{a}_s &= (1510.76 , 46.27 , -0.8036 , 0.)^T : p > 15 GPa \end{aligned}$$

where superscript T is the transposed of the vector. For the liquidus we used:

$$\begin{aligned} T_l(p) &= \vec{a}_l \cdot \vec{p} \\ \vec{a}_l &= (1762. , 57.46 , -3.487 , 0.0769)^T : p \leq 15 GPa \\ \vec{a}_l &= (1470.3025 , 55.53 , -0.9084 , 0.)^T : p > 15 GPa \end{aligned}$$

From Figure 5.2.a we conclude that up to 5 GPa and near the solidus (indicated with S in Figure 5.2.a) both parameterizations are similar. However, for the larger part of the phase-diagram the differences are significant. Deep melting processes for pressure values exceeding 10 GPa , for example, are excluded by the linear parameterization for realistic geotherms.

Also, the polynomial parameterization is combined with a more realistic parameterization of depletion dependency on the normalized super-solidus temperature θ given by

$$F(p, T) = f \left(\frac{T - T_s(p)}{\Delta T_{sl}(p)} \right) = f(\theta) \quad (5.2)$$

where symbol definitions are given in Table 2.1. We adopted an empirical relation for $f(\theta)$ as given by McKenzie and Bickle (1988), which is based on a third order polynomial fit of available empirical data. In Figure 5.2.b this relation is represented by the solid curve and the dash-dotted line is the linear relation used in Chapter 4, a linear fit derived from data given by Jacques and Green (1980). The dots on the curves correspond to

different degrees of depletion (30 %, 60 %) for which the equilibrium phase lines are drawn in Figure 5.2.a. The different phase diagrams result in a different distribution of partial melting. In particular, the more realistic curved solidus will result in melt production at greater depths. The differences in the phase diagrams result in different dynamics of the model. This is caused mainly by the corresponding differences in the compositional buoyancy defined in terms of F and in the differences in latent heat consumption during partial melting. The density effecting the buoyancy is given by the linearized equation of state

$$\rho(T, F) = \rho_0[1 - \alpha(T - T_{srf}) - F \delta\rho/\rho_0] \quad (5.3)$$

The EOS (Equation 5.3) includes a linear fit of empirical data specifying $\rho(F)$ from Jordan (1979), where $\delta\rho$ is given in Table 2.1.

In the present work two sets of modelling results are discussed which differ in the type of parameterization of the melting phase-diagram. Model A uses the linearized parameterization and Model B and C are based on the higher order polynomial parameterization.

5.2.3 Thermal coupling between upper and lower mantle

For secular cooling models of the upper mantle, thermal coupling between upper and lower mantle is important. Here we consider two limiting cases implemented in the aforementioned Models A to C. Model A includes a simple heat reservoir representing the lower mantle which is assumed isothermal $T = T_R(t)$ as used by Kameyama et al. (1996). The reservoir does not contain any internal heating. Its volume is twice the volume of the upper mantle and other physical properties equal those of the upper mantle. The heat extracted from the reservoir is computed from the heat flux through the lower boundary of the numerical model, i.e. the upper/lower mantle interface. The reservoir temperature is used as a time dependent essential boundary condition in Model A.

In Models B and C we consider an upper mantle thermally isolated from the lower mantle. With the heat reservoir approximation we establish a more realistic estimate of the effect of a non-zero heat flow from the lower mantle. Models with a zero heat flux condition at the bottom boundary can be considered as end-member cases, which result in a maximum estimate of the rate of secular cooling of the upper mantle system (Chapter 4).

5.2.4 Governing model equations and numerical methods

In the following equations non-dimensional quantities are used unless explicitly stated otherwise. We used a non-dimensionalization scheme described by Van Den Berg et al. (1993).

For an infinite-Prandtl-number fluid the momentum equation with the thermal and compositional Rayleigh numbers Ra and Rb , respectively, is given by

$$\nabla \cdot (\eta(\nabla \vec{u} + \nabla \vec{u}^T)) - \nabla \Delta p = (Ra T + Rb F) \hat{z} \quad (5.4)$$

where \hat{z} is the unit vector in the vertical direction aligned with gravity. The definitions of the symbols are listed in Table 2.1.

The transport equation describing partial melting of a volume of mantle material in

terms of the degree of depletion F is,

$$\frac{D F(p, T)}{Dt} = \frac{D f(\theta)}{Dt} \quad (5.5)$$

where the right-hand-side describes a source distribution of partial melt production following from the phase diagram discussed above. Recurrent melting is incorporated in this formulation, meaning that a volume of recycled partially melted material experiences further melting when its super-solidus temperature θ is in excess of any previously reached value.

The energy equation used is based on the Extended Boussinesq Approximation (EBA) (Ita and King 1994)

$$\frac{dT}{dt} - Di(T + T_0)u_z = \nabla^2 T + \mathcal{R}H(z, t) + \frac{Di}{Ra}\Phi - (T + T_0)\frac{\Delta S}{c_p}\frac{dF}{dt} \quad (5.6)$$

where the symbols are defined in Table 2.1. The last three terms of the right-hand-side are the: radioactive heat generation, viscous dissipation, and latent heat consumption. The second term on the left accounts for cooling and heating due to adiabatic (de-)compression. The effect of viscous heating is relatively small since the vigor of convection is low after the depleted layer has formed.

The momentum and energy equations are solved with a finite element method (Van Den Berg et al. 1993), and a time dependent upwind scheme (SUPG) (Segal 1982; Hughes and Brooks 1979) is applied to the latter to improve numerical stability in advection dominated regions of the domain. The transport equation for F is solved using a method of characteristics (MoC) (Sotin and Parmentier 1989; Sparks and Parmentier 1993). A hybrid scheme using both low and high order interpolations for F in combination with a fourth order Runge-Kutta time-integration was applied over a structured grid (Chapter 6). In order to limit the amount of numerical diffusion over the whole domain, this unequally spaced grid used for the MoC computations of the degree of depletion field F was much denser than the finite element mesh used, and the grid densities were higher than those used in Chapter 4. We used a resolution with grid cells ranging from 1121 to 3116 m in the horizontal direction and 921 to 1688 m in the vertical direction. A Predictor-Corrector time-stepping scheme is applied to solve the Equations in the following order: (5.4), (5.5) and (5.6).

5.3 Numerical modelling results

We will focus mainly on the differences in the evolution of Models A and B. Results for Model A are qualitatively similar to earlier results described in Chapter 4. The increase of the activation volume in our present models results in a colder geotherm due to a thinner MBL.

Up to approximately 200 Ma both models A and B show a similar evolution pattern. After this time deep upper mantle differentiation starts to occur in Model B.

We first discuss the early stage before the onset of deep melting in Model B. Next we describe the long term evolution of the continental model with special interest in the stability of the system. A brief description of the dynamically created initial condition has been given above.

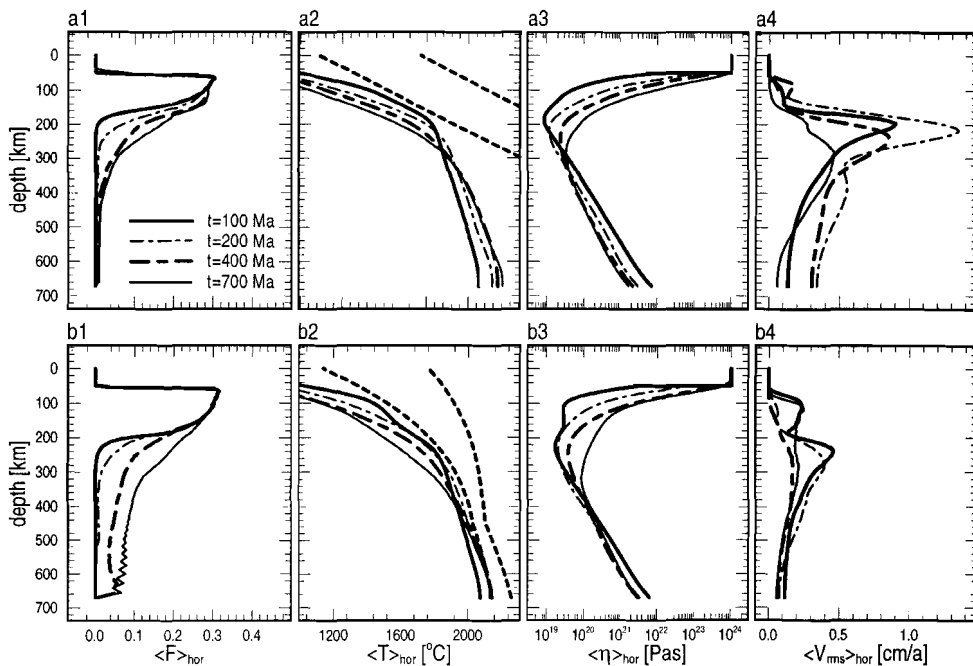


Figure 5.3: For all cases shown in Figures 10.3 and 10.4 horizontally averaged profiles are given: **1** the degree of depletion, **2** the temperature, **3** the viscosity, **4** and the velocity root mean square. The dashed curves in **a2** and **b2** are the solidus and liquidus. Note the numerical instabilities in the $\langle F \rangle$ -profile for $t = 700$ Ma in Model B (figure 5.3.b.1), which is caused by the too coarse grid over which the transport equation for F is solved. These wiggles are also expressed by the wash-board effect in Figure 10.4.b.2.

5.3.1 Early evolution

From Figure 10.3.a and 10.3.b a global comparison between model A and B can be made. In the left column the compositional field (degree of depletion F) is shown with upper (white) and lower (black) crustal layers on top of the partially depleted layer shown in colour. The lateral variation of the temperature field with respect to the horizontally averaged background value, i.e. $T - \langle T \rangle_{hor}$, is shown in the right-hand column. All frames also contain instantaneous flow lines indicating clock- and counter-clockwise flows as black and white contour lines respectively.

The advection velocities in Model A are higher than those in Model B as can be seen from the number of flow lines within each convection cell. This is mainly due to the differences in the accumulated depleted layers resulting from the different melting parameterizations as will be shown below. The small downwellings of material with low degree of depletion of < 10 % (light-blue to white) in Figure 10.3.b.2 are due to re-mixing as will be discussed together with the long term evolution.

The lateral temperature variations are similar for both models, with exception of the high T -anomaly above the upwelling part of the convecting cells in Figure 10.3.a.2. This large scale two-cell convection pattern is persistent during a long period of model evolution. Figure 10.3.a and 10.3.b illustrate the relatively short time scale of < 100 Ma in which a compositionally distinct continental root builds up in a convecting mantle

after the onset of melting at $t = 0$. This shows that mantle differentiation is a powerful process in a planetary mantle that is hot enough for the mantle adiabat to intersect the solidus. The rapid build-up of a stably layered system results in a reduced heat transport efficiency and a gradual warming of the deeper half of the model.

Figure 5.3 shows the depth distribution of several horizontally averaged quantities for four time values after the onset of melting for both Model A (Figure 5.3.a) and B (Figure 5.3.b). Frames numbered 1 through 5 correspond to (1) degree of depletion F , (2) temperature T , (3) viscosity $\eta(p, T)$, and (4) root-mean-squared velocity V_{rms} . The averaged profiles for F (Figure 5.3.a.1 and 5.3.b.1) indicate that both models initially evolve in a similar way. The continental root grows due to the mechanism of intermittent small-scale diapiric melting events as investigated in Chapters 4 and 6, where the parameterization of Model A was used. The same mechanism is operative in Model B.

The depleted layer in model B (Figures 10.3.b, 5.3.b.1) is thicker than in Model A where melting occurs in a greater depth interval. This is clearly shown by the difference in pressure where the initial geotherm intersects the solidus lines in Figure 5.2.a. This pressure difference is about 1 GPa and results after 100 Ma in a continental root extending to approximately 180 and 220 km for model A and B, respectively. Note also the finite values of F in the 350 to 500 km depth range after 200 Ma in Model B (Figure 5.3.b1).

Due to the different $F(\theta)$ -parameterizations, the transition from the depleted root to the deeper undepleted mantle is sharper, i.e. the slope of $\langle F \rangle_{hor}$ is steeper for Model B (Figure 5.3.b.1) than in Model A (Figure 5.3.a.1). Note that the maxima of $\langle F \rangle_{hor}$ are in both cases practically identical. This is explained by the fact that for a θ of about 0.25, an F -value of about 30 % is obtained in both $F(\theta)$ parameterizations. This is indicated by the proximity of θ -values of the two dots for $F = 30\%$ in Figure 5.2.b. Figures 5.3.a.2,b.2 show the horizontally averaged geotherms. Both models show an initial increase of temperature with time in the deeper half of the model. This is a result of the rapid build up of a shallow layering inhibiting whole layer upper mantle circulation. This layering consists of cold and therefore strong material which is part of the MBL. This cold and depleted layer is gravitationally stable with respect to the deeper parts of the model. A super-adiabatic regime develops quickly in this stagnant top layer, indicating the predominance of conductive heat transport over advection. In Model B the geotherm intersects the solidus at large depths at $t \sim 200Ma$ and melting is initiated in the lower half of the domain. The latent heat effects of the exothermic phase transition from olivine to spinel at 15 GPa may prevent the geotherm from crossing the solidus above 15 GPa . However, solid-state phase transitions are not included in the present models.

After several hundred million years ($\sim 300 Ma$) the temperature at the bottom of the upper mantle starts to decrease. These results illustrate the thermal blanketing effect of layered continental systems (Gurnis 1988), which delay secular cooling. This decrease of the bottom temperature is stronger in Model B, because of the absence of heat influx from the lower mantle, and because latent heat consumption and surface heat flow are higher in Model B.

In figure 5.3.a.3,b.3 viscosity profiles are shown, the crustal viscosity is set by the truncation value $\eta_{max} = 10^{24} Pa\cdot s$ applied for numerical reasons. Effects of initial warming at large depth and cooling from the top are reflected in the temperature dependent viscosity. Model A develops a viscosity minimum which is slightly more pronounced and at shallower depth than Model B.

In Figure 5.3.a.4,b.4 we show the V_{rms} distribution based on horizontal averaging. Model B shows a strongly reduced vigor of convection in the top half of the model. This is explained by the fact that the low viscosity zone in Model A is effectively positioned below the depleted layer resulting in a relatively mobile top layer of the undepleted mantle. In Model B the low viscosity zone occupies a depth range with finite value of the degree of depletion F , reducing the vigor of convection.

5.3.2 Long term evolution

Figures 5.3.a.1,b.1 show that models A and B have a different long term evolution. In Model A the thickness and volume of the continental root gradually increases with time due to the melting events in the upward flow of the two cell convection pattern which persists in the deep undepleted zone. At the sites of the downwellings depleted material is slowly dragged into the lower half of the model. A low degree of depletion of about 2 % volume average is found in this lower half.

In Model B much further depleted material is found in this deep region. Only a small part of it originates from re-mixed depleted material. Most of it is formed at depth since the geotherm has reached and crossed the solidus after about 200 Ma of evolution as shown in Figure 5.3.b.2. This results in modest but steady partial melting during the time-span from $t = 200 Ma$ to 850 Ma . The wiggles in F shown in Figure 5.3.b.1 below 450 km depth are due to the limited grid resolution in the lower part of the model.

Figures 5.3.a.2,b.2 show the evolution of the geotherm for Models A and B, respectively. In Model B, the geotherm is stabilised close to the solidus at large depths (i.e. $p > 15 GPa$) during the initial warming stage. This is the result of the occurrence of deep partial melting and the associated latent heat consumption at these depths. In Model A, the averaged temperature at 670 km is steadily increasing and is not bounded by partial melting. Due to shallower melting events the root is growing steadily and conductive heat transport slowly becomes more dominant than advection.

The geotherms in Figures 5.3.a.2,b.2 also show that when the heat reservoir approach is used, i.e. Model A, the inflow of heat from the lower mantle is very small. We therefore conclude that the differences in the results of Models A and B are mainly due to the difference in the phase-diagrams and to a lesser extent to the different thermal coupling with the lower mantle.

Figures 5.3.a.3,b.3 show the corresponding viscosity profiles during the evolution. In Model B the viscosity at large depths reaches an almost stationary value after 200 Ma since the geotherm becomes almost stationary. As secular cooling proceeds the MBL at the top grows and the minimum viscosity value increases and its position slowly shifts from 200 to 300 km depth during the 200 to 700 Ma time-span. Model A has a less thick depleted top layer and advection rates are higher than in Model B. This results in a hotter geotherm in the root and a smaller viscosity minimum.

These differences in geotherm evolution combined with a different evolution of the buoyant zone result in different convection velocity profiles shown in Figures 5.3.a.4,b.4. Figure 5.3.a.4 shows that convective vigor in Model A has increased near the bottom of the depleted root. This indicates active melting and corresponding production of buoyant residual material. The thickness of the continental root grows accordingly (Figure 5.3.a.1). After 200 Ma velocities decrease as an effect of cooling from the top and a corresponding increase of the viscosity, (Figure 5.3.a.3).

Figure 5.3.b.4 shows a downward shift of the velocity maximum and an increase of velocity at greater depth which coincides with the onset of deep melting around 200 Ma .

If we define that the transition from root to underlying mantle is situated at approximately $F = 0.1$, we see that at 700 *Ma* the continental root in Model B has grown to about 400 *km* thickness with large lateral variations (Figure 10.4). Convection velocities start to increase again while the melt production in the deep layer ($p > 15$ *GPa*) continues. Calculations for Model B were stopped at 850 *Ma* because insufficient resolution in the bottom layer and corresponding oscillations in the F -field solutions produce increasingly unreliable results beyond that time.

Figures 10.4.a and 10.4.b are contour plots of the depletion and temperature fields for Models A and B respectively. These snapshots correspond to the profiles as given in Figure 5.3, i.e. 400 and 700 *Ma*. For Model A also the snapshot at $t = 1200$ *Ma* is given.

In Model A the pattern of convection changes from a relatively vigorous two-cell pattern at 400 *Ma* to a multi-cell convection regime at 700 *Ma*, in line with the observed $\langle V_{rms} \rangle_{hor}$ profiles discussed above (Figure 5.3.a.4). Melting has stopped at ~ 650 *Ma*, so the depletion F is subject to advection only from that time on. Both snapshots of Model A show structures of depleted material with depletion values up to 10 % (white), which are dragged down into the undepleted zone. This process contaminates the deeper regions with depleted material at very slow rates. At $t = 1200$ *Ma* (Figure 10.4.a.3) there is a small thread-like structure of depleted material (green, i.e. $F \sim 15$ %) delaminating at $x = 1000$ *km*.

Figure 10.4.a.3 shows more stream-lines at $t = 1200$ *Ma* than Figure 10.4.a.2 at $t = 700$ *Ma*, indicating that convection rates have increased over this time interval. This is caused by continued cooling from the top, which slowly increases the temperature difference across the deeper undepleted layer and increases convection rates. It also neutralizes the positive compositional buoyancy of the deep part of the continental root, which allows for intermittent small scale delamination (Figure 10.4.a.3). At the same time, however, the MBL extends to larger depths due to the cooling from the top (Figure 5.3a.3), which prevents the gross part of the root from sinking into the slowly convecting undepleted layer.

The lateral temperature variations shown in Figure 10.4.a.1,a.2 also express the change in convection style. The high T -anomaly above the ascending flow in the two-cell convection decreases from $t = 400$ to 700 *Ma*.

Figures 10.4.b.1,b.2 show the same snapshots for Model B. The scarcity of the stream-lines illustrates that the vigor of convection is much lower compared to Model A, which is in line with the 1-D velocity profiles shown in Figure 5.3.b.4. The differences in the depletion fields between Models A and B are large due to the ongoing deep melt production in the latter. This is illustrated by the large amount of depleted material with $F > 10$ % (white = 10 %) advected by the convection in the deep zone. Ongoing melt production keeps adding residual material in the continental root which grows to a depth of about 400 *km*. The ‘wash-boarding’ effect in the low depletion zone (light blue to white) correspond to the wiggles already described in the 1-D profiles in Figure 5.3.b.1. In Figure 10.4.a.3 no ‘wash-boarding’ is observed since the used resolution is much higher in the lower part of the domain in Model A than in Model B.

The amplitude of the temperature anomalies in Model B increase from $t = 400$ to 700 *Ma* as shown in Figures 10.4.b.1 and 10.4.b.2. This coincides with a temporal acceleration of the convective flow at about $t = 700$ *Ma*, related to the upwelling near $x = 1000$ *km* and downward flow at $x = 500$ and 1500 *km*. The temperature anomalies shown in the right-hand column correlate with the distribution of composition and the structure of the convective flow. The depleted compositional root is generally cold with

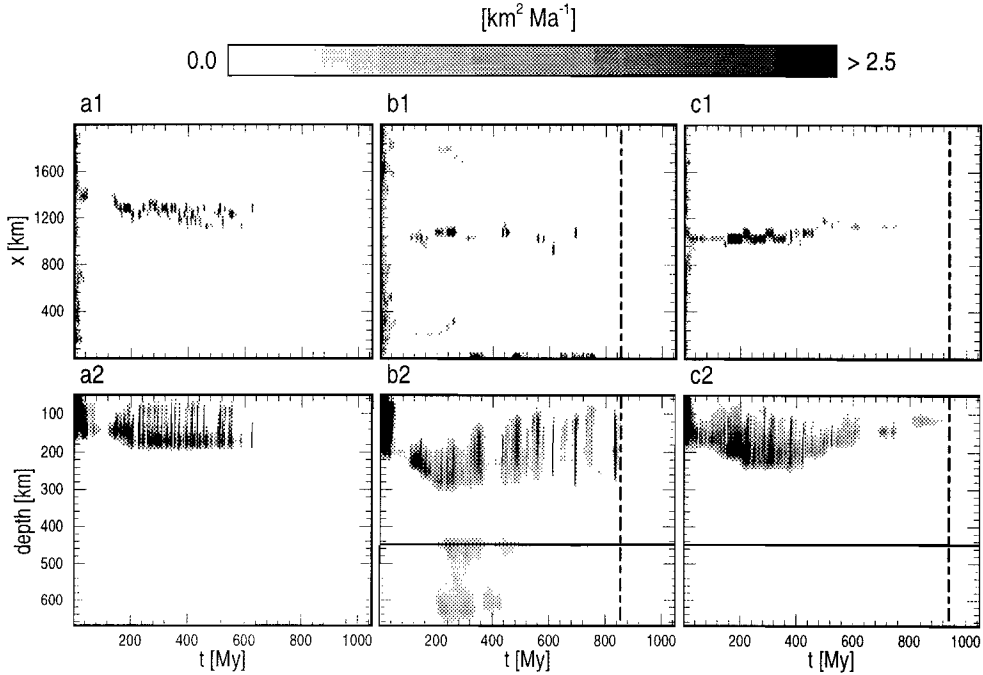


Figure 5.4: The horizontal (a1-c1) and the 1-D depth (a2-c2) melt production distribution as a function of time for Model A, B and C. Figures labeled a, b and c correspond to Model A, B and C respectively. Note the large difference in partial melting depths for both cases. In b2 and c2 the solid line is the depth where the 15 GPa kink in the solidus is located. The dashed vertical lines indicate the time where computations have been stopped. Model calculations for Model A exceed the here given time-window.

the exception of young newly formed residual material in upwelling flow. The spatial variations of the depletion and of the temperature field are both reflected in the geophysical observables: the seismic wave velocity structure of continental areas as revealed by surface wave tomography (Muyzert 1996; Curtis et al. 1998), wave velocity patterns (Jordan 1975; Anderson 1990), and the shear wave velocity distribution on a global scale (Zhang and Tanimoto 1993), and in the observed gravity field over continental areas (Matyska 1994; Doin et al. 1996).

5.3.3 Patterns of mantle differentiation

Figures 5.4.a.1 and 5.4.b.1 show the evolution of the melt production accumulated over columns in the models as a function of the x -location and the evolution of this melting pattern. The first 50 Ma of the evolution corresponds to the initial phase of rapid differentiation immediately following the onset of melting at $t = 0$. During this initial period most of the continental root is formed in our model. The Figures show that most of the melt is formed in vertical columns with a steady position at the location of warm upwellings in the large scale convection pattern of the deep mantle shown in Figure 10.3. Figure 5.4.a.2,b.2 show the evolution accumulated over rows of the computational domain. These frames illustrate the evolution of melt generation at different

depths. Melt production occurs in a wider range for Model B as a consequence of the different shape of the peridotite solidus (Figure 5.2.a).

Deep melt production, for $p > 15 \text{ GPa}$, starts around 200 Ma in Model B (see Figure 5.4.b) and continues until the end of the computation at 850 Ma . The deep melting has a less pulsating character in time because this type of melting does not take place in rapid vertical ascending flows. Melt generation is concentrated at 600 km depth and near the kink of the phase equilibrium lines at 448 km depth, i.e. at $p = 15 \text{ GPa}$. This is explained by the way in which the almost adiabatic geotherm intersects the curved solidus in the this part of the model. The large melting event between $200 - 300 \text{ km}$ depth at 700 Ma (Figure 5.4.b.2) is reflected in the F and T -fields (Figure 10.4.b.2).

The same melt production plots for Model C are given in Figures 5.4.c1,c2. Model C has the same phase-diagram parameterization as Model B, but no deep melting occurs due to the lower potential temperature and the lower density of heat generating elements. The pattern of melting is therefore similar as in Model A and differentiation takes place at pressures lower than 10 GPa . The depth range is, however, larger than in Model A and extends to a maximum of 250 km . When cooling proceeds melting ceases as in Model A, although in Model C melting proceeds longer than in Model A.

A 3-D extension of the 2-D model will not alter the observed processes to a great extent. On the one hand, a cylindric type of upwelling in a 3-D model will probably melt further since it can penetrate more easily into the existing root. On the other hand, excess heat contained in the diapir is also lost more rapid in a cylindric configuration, which results in more modest degrees of melting.

5.3.4 Global evolution

Figure 5.5 shows several globally averaged quantities for Models A, B and C, denoted by short-dashed, solid, and long-dashed lines respectively. The first -150 to 0 Ma show the statistically steady-state of the start-up scenario during which partial melting and decay of radioactive heat sources is switched off. Melting is allowed for times larger than $t = 0 \text{ Ma}$, when radioactive decay starts. This results in the short period of about 50 Ma of extensive differentiation, illustrated also in Figure 5.4, during which a large part of the continental root is formed. The rapid initial formation is an artifact of the particular start scenario used. Subsequent evolution however shows more realistic aspects of the model.

The volume averaged temperature shown in Figure 5.5.a diverges between Model A and B, especially from about 200 Ma onwards. This is mainly due to the effect of latent heat consumption, which increases strongly at the onset of deep melt production in Model B. The secular cooling shown in Figure 5.5.a is mainly due to conductive cooling from the top, since deeper parts of the model experience an initial warming during several hundred million years as shown in the evolution of vertical profiles in Figure 5.3. Model C has an averaged initial temperature which is 70 K lower than in Models A and B. After the onset of melting, owing to the reduced heat production, the temperature in Model C drops much faster than in the two others.

Figure 5.5.b shows the volume average of the degree of depletion. The initial phase of rapid melting is reflected in the steep increase of $\langle F \rangle$. In Model B, more melt is produced and melting continues until the end of the computations whereas in Model A, melting ceases around $t = 650 \text{ Ma}$. Model C produces approximately the same volume of continental root as Model A which is explained by the difference in phase-diagram parameterization: in spite of a colder geotherm it can still generate a large amount of

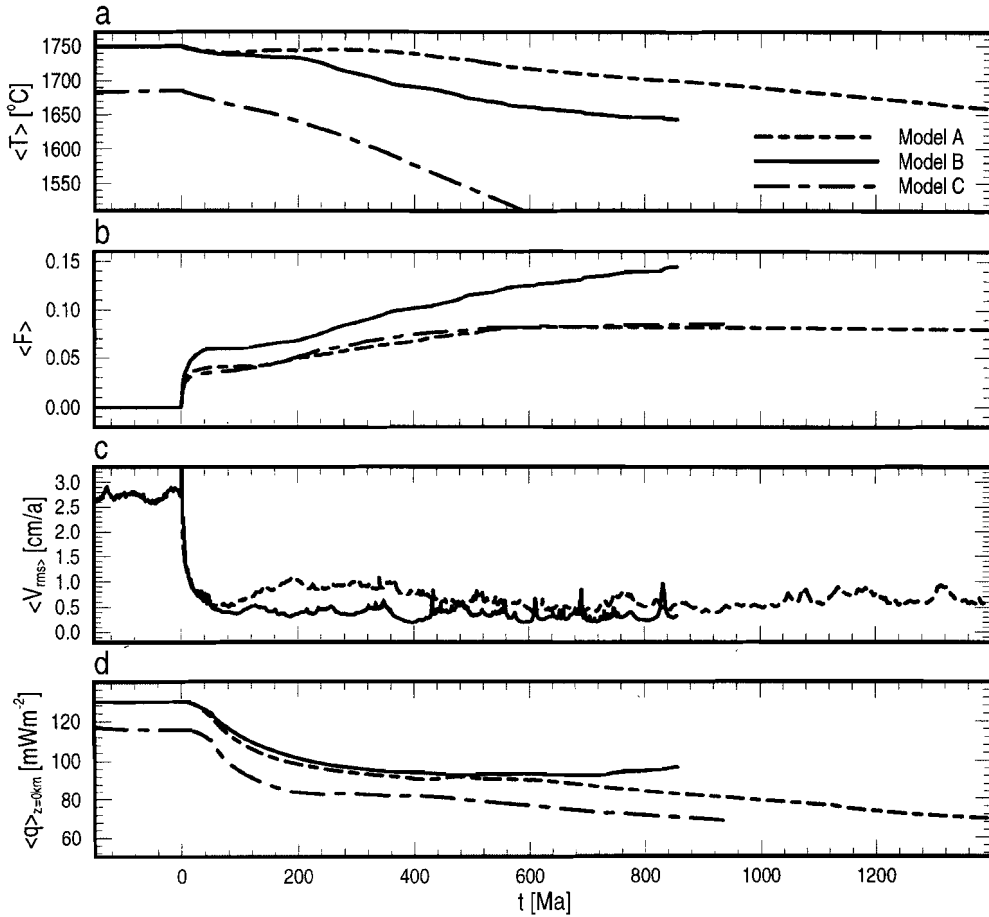


Figure 5.5: For both models the evolution of some volume averaged quantities are given. The results for Model A,B and C drawn with short dashed, solid, and long dashed lines respectively. Volume averages of the following quantities are depicted: a temperature, b degree of depletion, c velocity root-mean-square (Model C not shown). The averaged surface heat flow number is depicted in d.

depleted material.

Figure 5.5.c shows the root mean square velocity V_{rms} based on the volume average. After an initial spike shortly after $t = 0$ of 5 cm a^{-1} for Models A and B, truncated in the time series plot, the $\langle V_{rms} \rangle$ drops from 2.8 cm a^{-1} during the statistically steady-state before the onset of melting to a value lower than 1 cm a^{-1} . Small local maxima correspond to pulsating diapiric events which also coincide with small shifts in the time series of $\langle F \rangle$ (i.e. increasing) and $\langle T \rangle$ (i.e. decreasing). The $\langle V_{rms} \rangle$ for Model C (not shown) depicts a similar pattern. Relative high advection rates are found before a continental root appears, although the value is lower ($\langle V_{rms} \rangle = 1.8$) than in Models A and B due to the thicker MBL. After the formation of the root advection rates are of the same value as in Models A and B.

The V_{rms} values are of the order of 1 cma^{-1} . The strong decrease of the V_{rms} after the initial spin-up at $t = 0 \text{ Ma}$, which corresponds to the onset of differentiation, is due to the formation of a stably stratified layering with a top layer subjected to cooling from the top down. This reduces the effective depth of the convecting layer by almost a factor 2. Applying simple boundary layer theory, with $V_{rms} \sim Ra^{\frac{2}{3}} \sim h^2$ and h the depth of the convecting layer (Turcotte and Schubert 1982), predicts a decrease of V_{rms} by a factor 1/4. This approximates the velocity amplitude reduction after $t = 0 \text{ Ma}$ as observed in Figure 5.5.c.

The bottom part of the model forms a relatively slowly convecting layer, and therefore has no pronounced Thermal Boundary Layer (TBL) (Figure 5.3.a.4).

The heat flow density through the Earth's surface is shown in Figure 5.5.d. Values decrease considerably after the formation of the stable continental root that prevents whole layer convection. During later evolution the strong MBL grows from the top down and a more conductive regime, with reduced heat flow, develops. The increase in $\langle q \rangle$ for Model B corresponds to the acceleration in the convective heat flow at approximately $t = 700 \text{ Ma}$ discussed above. The heat influx from the lower mantle in Model A is less than 7.5 % of the heat outflow through the surface, whereas Model B has a zero heatflow contribution from the lower mantle. Nevertheless, the surface heat flow in Model B is slightly higher than in Model A. This is due to the modestly higher advection rates in the very shallow part of the root in Model B compared to Model A (Figure 5.3.a.4,b.4), which transports heat more efficiently through this thin shallow layer. Continental heat flow values range between approximately 25 and 75 mW m^{-2} at present for cratons (Pollack, Hurter, and Johnson 1993) and the here observed values should reach this range after approximately 2 to 3 Ga which is reasonable. Model C follows Model A but with an approximately constant heat flux difference of 15 to 20 mW m^{-2} . This is mainly due to the reduced radiogenic heat production in the crust of Model C.

5.4 Concluding remarks

Our numerical modelling results show that a hot convecting mantle will produce a compositional layering which is similar to the layered model of the continental tectosphere (Jordan 1975). It is found that this layering remains stable on a time scale greater than one billion year. These results support the conclusion that present day cratonic continental roots revealed by seismology are relicts of a hotter Archaean mantle.

We have investigated different parameterizations of the melting phase diagram of mantle peridotite. For the more realistic parameterization we found an increase in melt

production which also occurs over a larger depth range, compared to the simpler linear parameterization. This model also shows significant partial melting in the transition zone of the upper mantle ($p > 15 \text{ GPa}$), for a sufficiently high initial potential temperature (Model B). This model needs to be explored further in the future. In particular the solid state exothermic phase transition near 400 km depth and the associated latent heat effects on warm diapiric upwellings and the occurrence of deep melting requires further investigation.

Simulations with a simple melting phase diagram (Model A) show a compositional layering that becomes more pronounced until partial melting stops at about 650 Ma, which results from a progressive secular cooling that eventually brings the average geotherm below the solidus. This resulting layering remains stable for the duration of the computations (1400 Ma), but some small-scale delamination of the continental root and re-mixing of depleted material is observed.

In the interpretation of the observed long-term stability of the continental layering, we should keep in mind some limitations of the model. In the real Earth continents break up. This may be related to the interaction of large scale mantle plumes with continental roots and a certain degree of freedom for continental blocks to migrate laterally (Ebinger and Sleep 1998). In our model lateral migration is limited by the symmetry condition applied on the vertical boundaries of the computational domain. At the same time only relatively small mantle diapirs interact with the continental root and they cannot sufficiently affect the root to result in continental break up.

The continental root grows by means of relatively small scale diapiric upwellings which cross the solidus near the lower boundary of the root. These diapiric flows are then accelerated by the density reduction effect of the partial melting process on the residual matrix, resulting in a positive buoyancy which dominates the effects of latent heat consumption and adiabatic decompression, both included in our models. The amount of melt produced in a single diapiric event is significantly smaller than the estimated amounts produced during events that are related to continental flood basalts.

A clear correlation was found between lateral variations of the temperature and of the thickness of the continental root. Cold areas coincide with an increased thickness of the root and warm areas show a thinned root.

Chapter 6

A CHARACTERISTICS-BASED METHOD FOR SOLVING THE TRANSPORT EQUATION AND ITS APPLICATION TO THE PROCESS OF MANTLE DIFFERENTIATION AND CONTINENTAL ROOT GROWTH

¹ **Summary:** Purely advective transport of composition is of major importance in the geosciences and efficient and accurate solution methods are needed. A characteristics-based method is used to solve the transport equation. We employ a new hybrid interpolation scheme, which allows for the tuning of stability and accuracy through a threshold parameter ϵ_{th} . Stability is established by bilinear interpolations and bicubic splines are used to maintain accuracy. The principal effects of this hybrid interpolation method are illustrated and some tests are presented for numerical solutions of the transport equation. Finally, the method is applied to a model for the continental upper mantle system including differentiation by partial melting. In this case the transport equation describes the advective transport of material composition in a convecting medium. The equation contains a source term, which describes the melt production in pressure-released partial melting. Small-scale melting diapirs have been previously observed, which added differentiated material to an already existing continental root extending to approximately 200 km. We have verified the previous results with low resolution by comparing them with high resolution outcomes. The new high density grid used to solve the equations for mantle differentiation have grid cells down to 700 m horizontally and 515 m vertically, whereas the previous horizontal cell size was approximately ten times coarser. Experiments with this new high density grid results in highly detailed observations of the diapiric melting phenomenon. With this scheme, numerical instabilities can be suppressed by allowing numerical diffusion to work in time and locally in space. The scheme can be applied efficiently for preliminary modelling purposes. This can be followed by detailed high resolution experiments. We illustrate that this approach works successfully for the continental evolution model. We have demonstrated that the mechanism for continental root growth by melting and rising diapirs is robust in the presence of the higher resolution.

¹Part of this Chapter has been submitted for publication in *Geophysical Journal International*

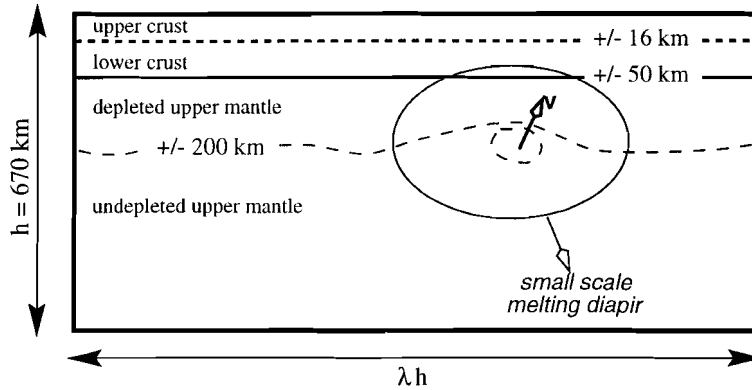


Figure 6.1: Schematic diagram of the numerical model sketching the investigated continental model. The crust forms a high viscosity layer with high radiogenic heat sources and the upper part of the upper mantle is a depleted layer with an intrinsically lower density than the deeper undepleted part of the upper mantle. The process of diapir growth of the depleted continental root is illustrated.

6.1 Introduction

The transport of heterogeneities by convective velocities arise in many diverse circumstances in the geosciences, ranging from the advection of heat sources (Honda and Yuen 1990), magmatic melts (Spiegelman 1993c; Ogawa 1993; Kameyama et al. 1996; Ogawa and Nakamura 1998), compositional fields in thermo-chemical convection (Hansen and Yuen 1989; Christensen 1992; Kellogg and King 1993) and the mixing of passive scalar fields in thermal convection (Ten et al. 1996). A review of the classical methods used for advection schemes has been given by Lenardic and Kaula (1993). A comparison of the different numerical methods for a thermo-chemical convection problem has been given in (Van Keken et al. 1997). A state-of-the-art treatise on this type of problem can be found in the recent book by Sethian (1996).

In previous works (Chapters 4 and 5) we have presented a model for monitoring the stability and growth of continents in which recurrent melt production and differentiated material transport play a significant role. We have employed there a numerical method based on finite elements and a characteristics-based method, which is a hybrid scheme consisting of both bilinear and bicubic spline interpolations for advecting the mantle composition in the course of differentiation. In this Chapter we will elaborate on the technical aspects of the advection scheme employed in Chapters 4 and 5, display the benchmark results and present high-resolution applications on the transport of compositional heterogeneities during partial melting in the subcontinental upper-mantle.

6.2 Conceptual model and equations

In the course of describing the dynamics of the growth of the continental lithosphere, we must include a transport equation in the numerical model. This transport equation describes the changing degree of depletion F together with a source term for prescribing the differentiation of the upper mantle by partial melting. This is given by

$$\frac{D F(p, T)}{Dt} = \mathcal{P}(p, T) \quad (6.1)$$

where D/Dt is the Lagrangian derivative and contains explicitly the advection term for F by the mantle velocity. F is defined to be the mass fraction of the melt generated in a material volume of mantle rock. The right-hand-side contains the source term for F . This source $\mathcal{P}(p, T)$ term is determined by equilibrium thermodynamics through an empirically known phase diagram and its precise formulation is given in Appendix A. The degree of depletion does exert a compositional density effect and together with the thermal buoyancy term, they constitute the driving force in the Stokes equation

$$\nabla \cdot (\eta(p, T)(\nabla \vec{u} + \nabla \vec{u}^T)) - \nabla \Delta p = (Ra T + Rb F) \hat{z} \quad (6.2)$$

in which we apply a pressure- and temperature-dependent viscosity

$$\eta(p, T) = \mathcal{B}(F) \cdot \exp \left[\frac{E + pV}{RT} \right] \quad (6.3)$$

Definitions of the symbols used are given in Table 2.1. The differentiation process also consumes latent heat which is incorporated in the energy equation in which the adiabatic compression term is also included

$$\frac{dT}{dt} - Di(T + T_0)u_z = \nabla^2 T + \mathcal{R}H(\vec{x}, t) - (T + T_0) \frac{\Delta S}{c_p} S(p, T) \quad (6.4)$$

The term $H(\vec{x}, t)$ represents the radiogenic heat production, starting with initial distribution $H_0 = H(z, 0)$, representing an estimate for the Archaean upper mantle and crust with a depth of 670 *km*.

The equations and the parameter settings used are identical with those used in Chapter 4. Figure 6.1 depicts schematically the upper-mantle continental model, as described in Chapter 4.

The high viscosity continental crust consists of an upper and lower layer with different radiogenic heat production values. The upper and lower crustal layers have initial thicknesses of 16 *km* and 34 *km*, respectively. These crustal layers are subject to deformation due to convective stresses from the mantle below. This crustal system overlays a partly differentiated mantle. The differentiated part is the result of the partial melting process occurring at depths up to approximately 200 *km* and forms a non-uniformly depleted layer with low compositional density. The principal mechanism in which depleted material is added to the already differentiated layer which forms the continental root is sketched in Figure 6.1. The addition of depleted material is established by melting in small-scale upwelling diapirs that are formed in the convecting mantle below the continental root during secular cooling of the upper mantle. The transport/melt equation (Equation 6.1) describes the compositional evolution of the differentiated layer. The method of numerical solution applied to this transport equation is highlighted in this Chapter.

The transport equation is solved over a structured non-equidistant grid. The density of this grid can be changed independently on the finite element meshes used for the Stokes and energy equation. The energy and Stokes equation for thermal convection are solved using finite element methods (Van Den Berg et al. 1993). The accuracy and stability of the characteristics-based method which has been applied here to the transport equation for the composition can be affected by the grid density on the one hand, and the combination of high and low order interpolations on the other hand. This combination of different interpolation types into a hybrid scheme is chosen in an adaptive way, which is explained below.

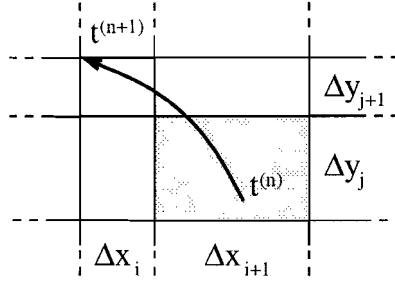


Figure 6.2: Schematic figure showing a small part of the the unequally spaced structured grid over which the transport equation is solved. Grid spacings are indicated by Δx and Δy in the x - and y -directions respectively. The part of a characteristic for a timestep $\Delta t = t^{n+1} - t^n$ is drawn. The characteristic is determined by numerical integration with a fourth order time dependent Runge-Kutta scheme. At the so-found starting point $\mathbf{x}(t^n)$ of this segment of the characteristic an interpolation of the compositional field is performed. The four grid points spanning the grey shaded cell are interpolated to the position $\mathbf{x}(t^{n+1})$ by bilinear or bicubic spline interpolation depending on the value of ϵ_{th} . This interpolated value is the new updated value in $\mathbf{x}(t^{n+1})$.

Firstly, a simple one-dimensional illustration of the method is given followed by a two-dimensional benchmark problem from the literature. Secondly, the feasibilities of the method are illustrated in the evolving continental upper mantle model for which high resolution grids have been applied.

6.3 The characteristics-based hybrid scheme

In our previous work on mantle differentiation in mantle convection models (Chapter 4) the right-hand-side (*RHS*) of Equation 6.1 represents a source term describing the change of F due to mantle differentiation by partial melting. In the following discussion of the numerical method, we will assume that there are no source terms ($RHS = 0$). This discussion is valid, as long as the *RHS* term is small compared to the advective terms. Otherwise, one would have to balance the *RHS* with the dominant term in the advective equation. The solution method is a characteristics-based method that used previously by Sotin and Parmentier (1989), Malevsky and Yuen (1991), Sparks and Parmentier (1993) and Ten et al. (1996). We will discuss below the two separate numerical steps involved: time-integration and interpolation.

Figure 6.2 highlights a part of the unevenly spaced structured grid employed. The arrow in Figure 6.2 depicts schematically a flow characteristic followed by a particle over the time-interval $\Delta t = t^{(n+1)} - t^{(n)}$ and is derived by direct numerical integration of the velocity field. Starting from the grid point where the particle is located at $t^{(n+1)}$ the characteristic of the time dependent velocity field is integrated backward in time up to $t^{(n)}$. This is accomplished by a fourth-order Runge-Kutta scheme, which is accurate (Waugh and Plumb 1994) and robust (Canuto et al. 1988; Press et al. 1992) for our applications.

For the resulting particle location at $t^{(n)}$, the F -field can be computed in terms of the known values at the structured grid at $t^{(n)}$. This interpolation involves the four grid points covering the grey-shaded grid cell in Figure 6.2. Replacing the F -value at $t^{(n+1)}$ with the interpolated value at $t^{(n)}$, we can now update one grid point. Repeating this

same procedure for all the other points yields a complete update of the field at $t^{(n+1)}$. Both the accuracy and stability of this scheme are determined by the interpolation employed.

Firstly, when bilinear interpolations are used, the method turns out to be unconditionally stable. However, a serious draw-back is that in this way the scheme suffers from a large degree of numerical diffusion (Calfin 1988). Secondly, a higher order technique, such as bicubic spline interpolation effectively reduces the degree of numerical diffusion. It turns out now that the stability of the method is not guaranteed. Both the amount of numerical diffusion and unstable behavior in both methods depend on: the grid spacing, the time step size in combination with the evaluated time-span, the characteristics of the advected field, and the flow regime. The practical application then determines the optimal solution method.

For example, in the continental upper mantle model the degree of depletion is coupled with the Stokes equation through the compositional buoyancy, and wiggles due to instabilities in the F -field may have an important numerically induced dynamical effect. Numerical diffusion on the other hand, will smear out the depletion field with a loss of amplitude of local maxima and details cannot be resolved. Here an incorrect buoyancy coupling is established, and this feedback may result in incorrect dynamics. Very high grid densities in combination with bicubic spline interpolations (Ten et al. 1996) can in general solve the stability problem for a certain class of problems. Nevertheless, for many practical applications this is either impossible because of characteristics of the advected field or it is not efficient enough.

Combining both interpolations into a hybrid scheme, in which bilinear interpolations or bicubic spline interpolations form two end-members, brings together the accuracy feature of the latter and the stability of the former. Suppose that the bilinear method results in a value of $F_b(t^{(n)})$ and the value $F_s(t^{(n)})$ follows from the bicubic spline interpolation. The difference between both values, i.e. $\epsilon = |F_b - F_s|$, is used to decide which one will be used for the update $F(t^{(n+1)})$ of the field value $F(t^{(n+1)})$. The essential part of the hybrid scheme is defined as

$$F(t^{(n+1)}) = \begin{cases} F_b(t^{(n)}) & \text{for, } \epsilon \geq \epsilon_{th} \\ F_s(t^{(n)}) & \text{for, } \epsilon < \epsilon_{th} \end{cases} \quad (6.5)$$

where ϵ_{th} is an empirically determined threshold value. This choice for either one of the two interpolations is determined locally and therefore the scheme is adaptive to the local conditions governing stability and accuracy. The hybrid scheme reduces to the bilinear scheme for $\epsilon_{th} = 0$, and the bicubic spline scheme follows when, in theory, $\epsilon_{th} \rightarrow \infty$. Effectively, any value in between induces numerical diffusion in cases where the bicubic spline interpolation gives under- or overshoots.

An advantage is that less dense grids are needed depending on the required accuracy, e.g. during development more efficient low density meshes can be used while stability is guaranteed. Expensive high grid densities are only applied for detailed final experiments. In addition, the method easily allows for the introduction of sources and sinks, as required in our application to a differentiating upper mantle.

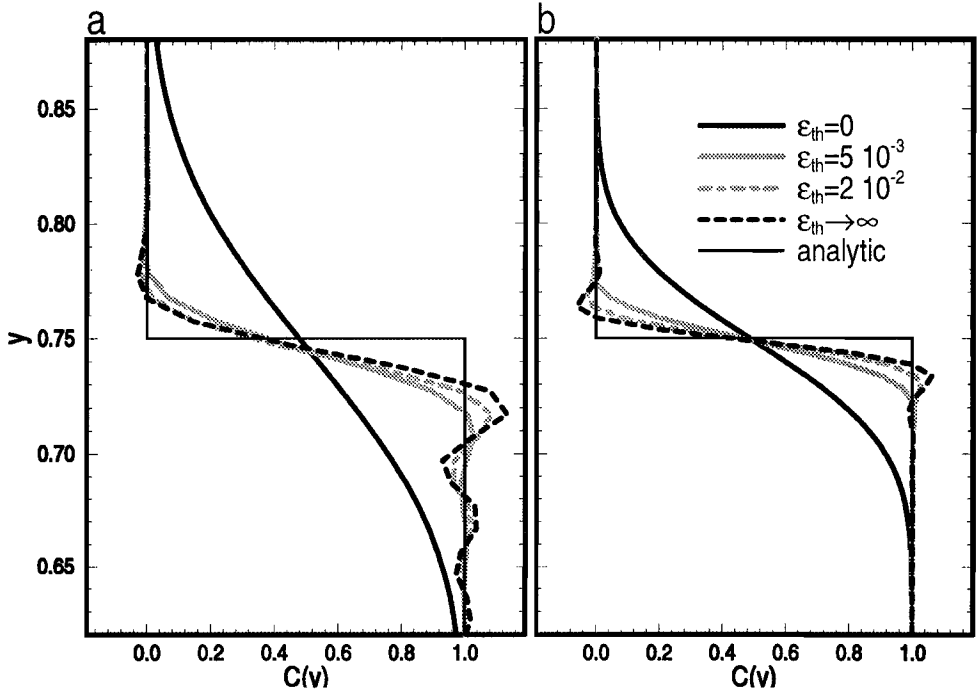


Figure 6.3: Results at $t = 0.5$ of the advected Heaviside function in a one-dimensional stationary uniform upward flow. Results for different values of ϵ_{th} are illustrated for different grid densities and time stepping. Frame **a** shows the result over 100 node mesh with $\Delta t = 1 \cdot 10^{-3}$ and **b** is for the same schemes as in **a** but with a 200 node grid and a larger constant time step of $\Delta t = 2.5 \cdot 10^{-3}$. This is equivalent with 500 time steps and 200 time-steps for Figure **a** and **b** respectively. Note that the location of the instability wiggles are different, when the time step size and grid spacing are modified and bicubic splines are used.

6.4 Test applications

6.4.1 A one-dimensional test case

To illustrate the hybrid scheme, we will conduct a simple one-dimensional experiment. A concentration function $C(y)$ is transported without any sources. Thus, the equation to be solved is Equation 6.1 with $RHS = 0$ and F is replaced by C . The initial function value is defined by $C(y) = 1$, for $0 \leq y < 0.25$ and $C(y) = 0$, for $0.25 \leq y < 1$. This Heaviside function is transported by advection in the positive y -direction with a uniform and constant upward velocity $v = 1$. At the inflow boundary we impose $C(0) = 1$ and at the boundaries natural splines ($\partial^2 C / \partial y^2 = 0$, see (Press et al. 1992)) are applied when cubic spline interpolation is used. The solution is computed at $t = 0.5$ when the Heaviside function should be centered at $y = 0.75$. We emphasize that the method is not optimal for transporting sharp interfaces and better methods are available for this specific case (Van Keken et al. 1997; Lenardic and Kaula 1993) and (Vreugdenhil and Koren 1993). This case is only studied because it demonstrates nicely the concept. Furthermore, a sharp interface is also involved in the two-dimensional benchmark problem discussed in the next section.

N	K	hybrid				$\epsilon_{th} \rightarrow \infty$			$\epsilon_{th} = 0$
		ϵ_{th}	$C_{min} [\%]$	$C_{max} [\%]$	$L_2 [10^{-4}]$	$C_{min} [\%]$	$C_{max} [\%]$	$L_2 [10^{-4}]$	$L_2 [10^{-4}]$
100	98	$1 \cdot 10^{-2}$	-2.22	1.25	61.9	-4.09	9.31	203	48.7
200	198	$5 \cdot 10^{-3}$	-0.71	0.66	39.4	-6.04	6.08	114	22.8
400	159	$1 \cdot 10^{-3}$	-2.86	2.11	3.81	-21.7	2.79	5.46	7.00
800	127	$2 \cdot 10^{-4}$	-1.47	0.07	2.66	-21.7	2.79	2.73	3.50
1600	102	$4 \cdot 10^{-5}$	-0.19	0.02	1.36	-21.7	2.79	1.36	1.75

Table 6.1: The values for the threshold parameter of the hybrid scheme with the number of nodes N and the corresponding value of K according to Expression 6.6. All results are for a constant $\Delta t = 0.0125$. Also listed are the maximum overshoot (C_{max}) and undershoot (C_{min}) values found for these experiments for the hybrid and the bicubic spline scheme. They are expressed in percentage of the maximum analytic function value $C = 1$. In this test case the bilinear scheme preserves the minimum and maximum function value.

Figure 6.3.a shows the results for a grid with $N = 100$ equidistant nodes and a constant time step $\Delta t = 1 \cdot 10^{-3}$. Four different values for the threshold criterion parameter ϵ_{th} have been applied. When the results are compared with the thin solid line corresponding to the analytical solution, we see that the purely linear scheme ($\epsilon_{th} = 0$) suffers from a large degree of numerical diffusion and the Heaviside function is severely smoothed. When more cubic splines interpolations are allowed, i.e. ϵ_{th} is increased, the wiggles indicate that the method becomes unstable. The steepness of the Heaviside function is increased, indicating that less numerical diffusion is induced.

Figure 6.3.b shows the results obtained over a equally spaced grid which is twice as dense ($N = 200$) and for which a larger time step of $\Delta t = 0.025$ was used. Grid refinement for fixed ϵ_{th} results in smaller wiggles since the cubic spline interpolations are more accurate, reducing the instabilities in the purely cubic spline experiment. Linear interpolations are also more accurate at a denser grid, leading to a reduction of the numerical diffusion, as shown by the steeper Heaviside function.

The difference between Figure 6.3.a and 6.3.b cannot be due entirely to the denser mesh. A constant but larger discrete time step used in Figure 6.3.b would mean that fewer time steps n_t are used to reach $t = 0.5$: $n_t = 200$ and $n_t = 500$ in Figure 6.3.b and 6.3.a, respectively. Fewer time steps result in a smaller accumulated or global error. The global error is dependent on the total number of time steps accumulated. The spatial and temporal discretization also influences the locations of the numerical instabilities around the step-function. In Figure 6.3.a the oscillations are accumulating downstream of the interface in C , whereas they are more centered around this jump in the step-function in Figure 6.3.b.

Finding the optimal parameter for the hybrid scheme

In order to determine a near optimal value for ϵ_{th} , we have quantified the errors in a series of experiments. First, we fixed the time step, since this simplifies the analysis for this coupled time-dependent problem involving both F and T fields. We have therefore varied only the equally spaced grid density and the hybrid threshold parameter for determining the optimal parameter at the fixed time step delta $\Delta t = 0.00125$.

In the following, we will define the criteria for determining the optimum. In the series of experiments with fixed $\Delta t = 0.00125$ we determined the maximum overshoot (C_{max}) and undershoot (C_{min}) and the relative error between the analytic and numerical solution defined according to the L_2 norm. By varying the ϵ_{th} from zero to infinity, we have tested the hybrid scheme.

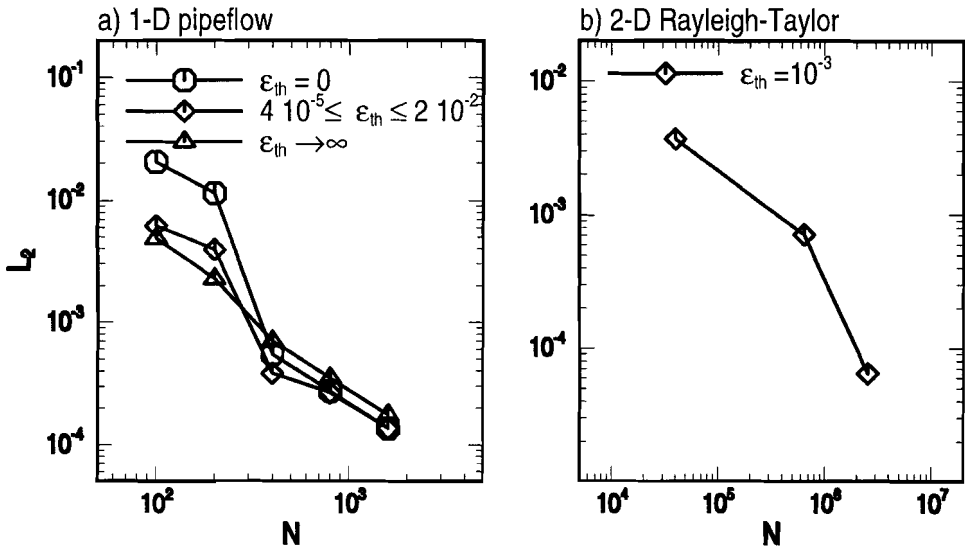


Figure 6.4: Convergence patterns of the relative L_2 -norm as function of grid points N for a) the one-dimensional pipe-flow for different values of ϵ_{th} and b) the isoviscous Rayleigh-Taylor benchmark for $\epsilon_{th} = 1 \cdot 10^{-3}$. The error in a) is determined by comparison with the analytical solution. In b) we determined the error at $t = 100$ by comparison with a numerical reference solution obtained with 60×60 quadratic velocity elements and 1000×1000 nodes for the compositional field. Both meshes were equidistant.

First, we stated that both over- and undershoots must be lower than 2.5% of the maximum value of the analytic function $C = 1$. Second, one solution was isolated as the best by taking the lowest L_2 norm. In Table 6.1 we list these relevant quantities for the selected solutions along with the relevant numbers for the two end-members obtained with only the linear and cubic splines, i.e. $\epsilon_{th} = 0$ and $\epsilon_{th} = \infty$, respectively. The over- and undershoot values for the linear end-member are not provided in the table, since for this specific test case the minimum and maximum function values are preserved. However, in other problems the numerical diffusion may become so large that the maximum and minimum values are no longer maintained. The numerical solutions, which were classified as successful, turned out to obey the following empirical relation

$$\epsilon_{th} = K \cdot (\Delta y)^2 \quad (6.6)$$

where Δy is the grid spacing and K a constant ranging from around 100 to 200. The corresponding values for K are given in Table 6.1.

The values of the L_2 norm as listed in Table 6.1 are used for a convergence test. The three error curves are depicted in Figure 6.4.a. The curve for the hybrid scheme is always close to the curve of the one end-member which has the lowest error for that grid density. Therefore, the hybrid scheme is, in general, more accurate than either one of the two end-members. For high grid resolutions the differences disappear. Thus, asymptotically all methods show approximately the same L_2 error. Note, however, that for ϵ_{th} tending toward infinity, the solution develops unnecessarily and unwanted large over- and undershoots.

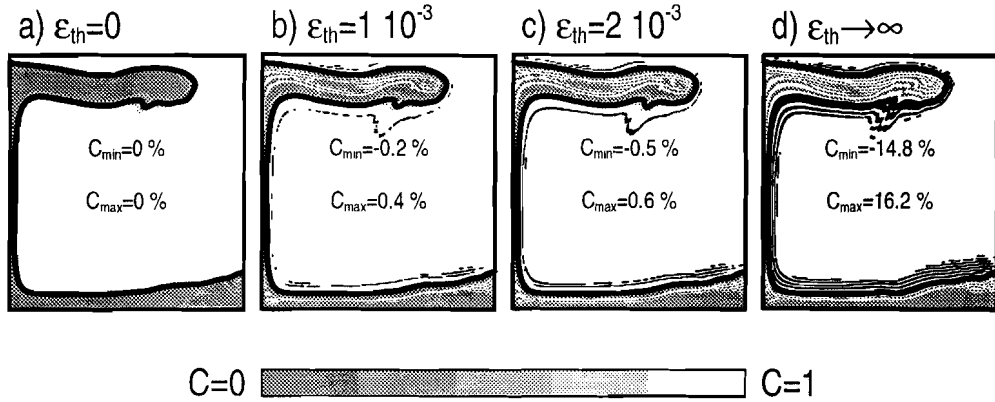


Figure 6.5: Results for the isoviscous Rayleigh-Taylor instability problem for $t = 500$. from **a-d** an increasing number of bicubic spline interpolation is applied. Around the interface, which is a Heaviside function of C , instability wiggles originate which become larger in amplitude (as indicated in each frame) when more bicubic spline interpolations are used. The wiggles in the composition field are depicted as white areas in the grey (i.e. $C = 0$) zone and black areas in the white (i.e. $C = 1$) zone. These results have been obtained with a relative low resolutions of 10×10 quadratic velocity elements and 200×200 nodes for the transport equation.

6.4.2 A two-dimensional benchmark

We have conducted one of the benchmarks cases as presented in Van Keken et al. (1997) for evaluating the hybrid scheme. We have extended the problem in two ways. First, we now solve a two-dimensional problem with a velocity field that varies spatially and temporally as well. Second, the Stokes equation has to be solved, since the compositional function C now couples to the buoyancy term, i.e. the *RHS* of Equation 6.2 in which C replaces F .

The benchmark problem is an isoviscous and isothermal Rayleigh-Taylor instability problem in which a low density layer is initially positioned underneath a thicker layer with a higher density. By virtue of its being gravitationally unstable, the lower layer then rises. This takes place in the form of pulsating diapirs. In this isothermal case the coupling to the Stokes equation takes place by means of the compositional buoyancy.

The compositional function C is defined as before, where now $C = 0$ and $C = 1$ represent the low and high density layers respectively. In Figure 6.5 we give for the four different hybrid schemes the results for the compositional field at $t = 500$ for relatively low resolution; $N = 100$ along both spatial dimensions for the equidistant grid used for C and the velocity is solved with 20×20 equally sized quadratic finite elements. Figure 6.5.a is only for bilinear interpolations ($\epsilon_{th} = 0$) and degrades the most from numerical diffusion, while no oscillations are observed. The thick solid black line in Figure 6.5 denotes the position of the interface at $C = 0.5$. By increasing ϵ_{th} more bicubic spline interpolations are involved and more under- and overshoot is generated in the form of wiggles near the sharp interface (Figures 6.5.b-d). The interface is drawn with the same thick solid black line as in Figure 6.5.a. These wiggles in the composition field are depicted as white areas in the grey (i.e. $C = 0$) zone and black areas in the white (i.e. $C = 1$) zone. Although the wiggles induce a locally non-physical effect in the buoyancy, the overall solution in the C -field does not suffer too much. This

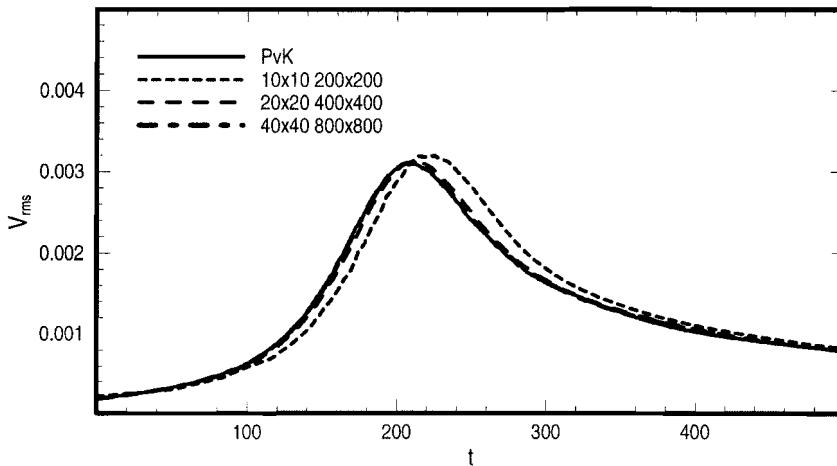


Figure 6.6: The V_{rms} as function of time for the isoviscous Rayleigh-Taylor benchmark. PvK is the result as obtained by Van Keken in the benchmark and is given as a reference. The other curves are for the hybrid scheme with $\epsilon_{th} = 10^{-3}$ and indicated resolutions for the number of quadratic velocity elements and number of nodes of the compositional grid respectively.

compensation effect is due to each velocity element covering an area which overlaps several wiggles and the averaging out of the buoyancy instabilities over the element.

Thus, reasonable results are obtained as shown by a comparison of the root-mean-square velocity as a function of time shown in Figure 6.6 for various resolutions and $\epsilon_{th} = 0.001$. Also plotted for reference in this figure is the V_{rms} curve obtained by Peter van Keken and given in (Van Keken et al. 1997). It can be seen that very good agreement is obtained between the solutions obtained with the hybrid scheme and Van Keken's results.

A convergence test at $t = 100$ has also been performed for the hybrid scheme. The result is shown in Figure 6.4.b where the reference solution was obtained with a equidistant grid of 1000×1000 nodes for C and 80×80 quadratic velocity elements and constant $\epsilon_{th} = 10^{-3}$. The value for K of the empirical expression 6.6 ranges from around 40 to 700 and $K = 1000$ for the reference solution. This value of K apparently does not need to remain constant for guaranteeing the convergence in the L_2 -norm.

6.5 Application of the hybrid scheme to the continental upper mantle model

We will now discuss the application of the hybrid method to the continental upper mantle model. This problem is concerned with an advected F -field, which develops in excess of a time-dependent run and has no specific characteristics, whereas the above

a	old and new vertical resolutions		
	N_y	$\Delta y_{min} [km]$	$\Delta y_{min} [km]$
F	159	0.515	44.5
\vec{u}	44	3.00	25.0
T	88	1.50	12.5

b.1	old horizontal resolutions		
	N_x	$\Delta x_{min} [km]$	$\Delta x_{min} [km]$
F	300	6.72	6.72
\vec{u}	60	33.5	33.5
T	120	16.75	16.75

b.2	new horizontal resolutions		
	N_x	$\Delta x_{min} [km]$	$\Delta x_{min} [km]$
F	978	0.700	9.60
\vec{u}	80	4.24	30.0
T	160	2.12	15.0

Table 6.2: Resolutions used in the previous (**old**) and the present work (**new**) for vertical (Table 6.2.a) and horizontal (Tables 6.2.b1 and 6.2.b2). The number of gridpoints used for F is given by N_x and N_y for x and y -directions, respectively. Finite elements were used to solve for \vec{u} and T and in these cases N_x and N_y refer to the number of elements.

benchmark situation focuses on thermo-chemical convection problems including only a sharp interface. The physics of the model have already been described in Chapter 4. One of the major conclusions was that small-scale upwellings from the deeper undepleted zone could add depleted material to an already differentiated continental root by means of small-scale partial melting events in the upwelling diapiric heads. We will now focus in some details of the numerical resolution aspects of these small-scale melting events in diapirs. We will study the effects of the numerical parameter ϵ_{th} in two high resolution numerical experiments by comparison these results with results obtained in the previous work using lower spatial resolution.

The modelling results of Chapter 4 are used here for comparison. At $t = 107 Ma$ we interpolated the previous results obtained previously with $\epsilon_{th} = 4 \cdot 10^{-4}$ to new structured grids for F and finite elements meshes for T and \vec{u} . Starting at this point, short model evolutions were recomputed until a small diapiric melting event occurred in the region where numerical resolutions were high. The old (i.e. Chapter 4) resolutions were as given in Tables 6.2.a and 6.2.b.1. The energy equation (Equation 6.4) is solved over linear triangular elements which are nested in the velocity elements: four temperature elements are placed in each \vec{u} -element (Van Den Berg et al. 1993). The employed finite element resolutions are also given in Tables 6.2.a and 6.2.b.1. In the following, the resolutions in the y -direction have been kept the same, since they were considered sufficient, whereas higher x resolutions were considered desirable.

Due to the differences in the spatial resolutions as well as the threshold parameter ϵ_{th} , small local differences in the degree of depletion evolved. Since this also effects the local dynamics, the diapirs did not occur at exactly the same place and time in models with different numerical parameters. However, the results show that that the phenomenon of continental root growth through small-scale diapirism remains unchanged. Figure 10.5 shows the snapshots of the temperature and the depletion field.

The modified temperature field of Figure 10.5.a is the T -field reduced by the horizontally averaged geotherm to emphasize the small lateral differences. The arrow in Figure 10.5 points at a hot anomaly in a rising diapir in which depleted material is formed shown in Figure 10.5.b at the same position. A typical time-span during which

poly-baric melting in the diapiric head occurs is approximately $20 Ma$ and after this stage the newly formed depleted material is added to the already depleted layer. Figure 10.5.b corresponds to the situation sketched in Figure 6.1. The shallow white and black layers are the upper and lower crust, respectively.

In Figure 10.6 we show three close-up shots of equal size but with horizontally shifted spatial windows, displaying the area surrounding the melting event at nearby times and at identical depths. Figure 10.6.a is for the same spatial resolutions as used in Chapter 4. The other two (i.e. Figure 10.6.b and 10.6.c) are for identical very high spatial resolutions of the structured grid and the finite element meshes as given in Table 6.2.b.2. These highest resolutions always coincided with the locations of the diapirs as depicted in Figure 10.6. Also different values of ϵ_{th} are used: $\epsilon_{th} = 5 \cdot 10^{-6}$, $\epsilon_{th} = 1 \cdot 10^{-3}$, $\epsilon_{th} \rightarrow \infty$ in Figures 10.6.a, 10.6.b and 10.6.c, respectively. The resulting wide range of K -values is listed in Table 6.3.

The combination of a small ϵ_{th} together with a low resolution in Figure 10.6.a results in relatively large degree of numerical diffusion and gives a more vague diffusive formation of diapirs compared to the event highlighted in Figure 10.6.b. In this figure panel we can see much greater detail in the melting plume head and the surroundings. This sharpness increases even further, when only bicubic splines are employed as shown for the case for Figure 10.6.c. This is possible at places with very high densities of grid points, which has been applied in the top portion of the figure panel at approximately $200 km$ depth. At depths greater than $200 km$, there is insufficient resolution for F and the numerical scheme then becomes unstable. The resulting oscillations are revealed by the grey-tomes at $250 km$ and deeper in Figure 10.6.c. These grey areas even show non-physical negative F -values ($F_{min} = 0.6\%$) and positive wiggles or overshoots must be also present. However, overshoots cannot be readily discerned from the physically correct F -values.

It is important to note that the size of the diapirs, say $100 km$ in width and $60 km$ in height, is sufficiently large as not to be influenced by the change in numerical parameters. One important conclusion is that the previously found growth mechanism of the continental root is of the same type and approximately the same size in all the studied models. The amount of melt generated, however, does depend on the numerics. The amount of generated melt was $50,000$, $31,000$, and $76,000 km^3$ for Figures 10.6.a to 10.6.c, respectively. Since the differences in the evolution of the degree of depletion in the diapiric heads, also different buoyancy couplings are established, and it is therefore not possible to isolate the different numerical effects that affect the evolutions.

Another point to stress is that the velocity mesh and corresponding temperature mesh in Figure 10.6.b and 10.6.c are also denser over the shown area than in Figure 10.6.a. This may also have affected the shapes and volumes of the diapirs. However,

	old	new		
refers to Figure	10.5.b	10.6.a	10.6.b	10.6.c
ϵ_{th}	$4 \cdot 10^{-4}$	$5 \cdot 10^{-6}$	$1 \cdot 10^{-3}$	∞
$K_{x_{min}}$	3.98	0.0244	4.87	∞
$K_{x_{max}}$	3.98	4.58	916.	∞
$K_{y_{min}}$	0.0907	0.00113	0.227	∞
$K_{y_{max}}$	677.	8.40	1693.	∞

Table 6.3: The thres-hold parameter ϵ_{th} together with resulting maximum and minimum K -values according to Equation 6.6 and the grid resolutions as given in Tables 6.2.a and 6.2.b. Again, **old** refers to the previous results as discussed in the text and **new** refers to the present expirements.

because the finite elements have the same sizes in Figure 10.6.b and 10.6.c, and both differ in the parameter ϵ_{th} , this would mean that the difference in the hybrid scheme is more importance.

To provide a detailed view in the F -field surrounding the diapir depicted in Figure 10.6.c, we now zoom into this event in Figure 10.7. This figure portrays the event with the highest resolution in the visualization. Note how the diapir impinges on the already depleted layer and squeezes the lightly depleted diapiric front zone between the shallow layer driven by the high compositional buoyancy in the head of the diapir, which is stopped by the cold mechanical boundary layer induced by the temperature-dependent viscosity.

6.6 Concluding Remarks

We have demonstrated that the hybrid interpolation scheme based on the method of characteristics works well for different types of advecting fields, involving composition and degree of depletion in melting processes. With the threshold parameter ϵ_{th} , we find it possible to employ efficient low density grids and obtain low accuracy results while maintaining numerical stability. Very detailed fields can be obtained by high density grids with a local spatial resolution of the order of one kilometer.

This procedure is demonstrated to be reliable from our tests. Previous low resolution experiments (Chapter 4) whose resolution was about ten times coarser in the horizontal direction than the highest resolution used here still reveal the same diapiric melting events as the ones presented here within the framework of an upper-mantle continental model. The same type of melting phenomenon is found as in the models of Chapter 4.

Chapter 7

EARLY FORMATION AND LONG-TERM STABILITY OF CONTINENTS RESULTING FROM DECOMPRESSION MELTING IN A CONVECTING MANTLE

¹ **Abstract:** The origin of stable old continental cratonic roots is still debated. We present numerical modelling results which show rapid initial formation during the Archaean of continental roots of about 200 km thick. These results have been obtained from an upper mantle thermal convection model including differentiation by pressure release partial melting of mantle peridotite. The upper mantle model includes time-dependent radiogenic heat production and thermal coupling to a heat reservoir representing the Earth's lower mantle and core. This allows for model experiments including secular cooling on a time-scale comparable to the age of the Earth. The model results show an initial phase of rapid continental root growth of about 0.1 billion year, followed by a more gradual increase of continental volume by addition of depleted material produced through hot diapiric convective upwellings which penetrate the continental root from below. Within about 0.6 Ga after the start of the experiment, secular cooling of the mantle brings the average geotherm below the peridotite solidus thereby switching off further continental growth. At this time the thickness of the continental root has grown to about 200 km. After 1 Ga of secular cooling small scale thermal instabilities develop at the bottom of the continental root causing continental delamination without breaking up the large scale layering. This delaminated material remixes with the deeper layers. Two more periods, each with a duration of about 0.5 Ga and separated by quiescent periods were observed when melting and continental growth was reactivated. Melting ends at 3 Ga. Thereafter secular cooling proceeds and the compositionally buoyant continental root is stabilised further through the increase in mechanical strength induced by the increase of the temperature dependent mantle viscosity. Fluctuating convective velocity amplitudes decrease to below 1 cm a^{-1} and the volume average temperature of the sub-continental convecting mantle has decreased about 340 K after 4 Ga. The modelling results show that the combined effects of compositional buoyancy and strong temperature dependent rheology result in continents which overall remain stable for a duration longer than the age of the Earth. Tracer particles have been used for studying the patterns of mantle differentiation in greater detail. The observed (p, T, F, t) -paths are consistent with proposed stratification and thermo-mechanical history of the depleted continental root, which have been inferred from mantle xenoliths and other upper man-

¹Part of this Chapter has been submitted for publication to *Tectonophysics* Special Issue on 'Continental Formation, Growth and Recycling' (1999)

tle samples. In addition, the particle tracers have been used to derive the thermal age of the modelled continental root, defined by a hypothetical closing temperature.

7.1 Introduction

The oldest continental shields have been stable for several billion years. The origin of these regions and the reason for their long term stability is still debated. From seismological evidence (Jordan 1975; LeFevre and Helmberger 1989; Anderson 1990; Woodhouse and Trampert 1995; Polet and Anderson 1995) and interpretation of the gravity field (Doin et al. 1996), and surface heat flow data (Pollack and Chapman 1977; Nyblade and Pollack 1993; Rudnick et al. 1998) for continental regions it has been concluded that continents are underlain by thick roots of compositionally distinct material. Analysis of mantle xenoliths from different continental regions (Jordan 1979; Griffin et al. 1996) has shown that the continental roots consist of residual material from pressure release partial melting of mantle peridotite.

We have developed a numerical mantle convection model to investigate the formation of continents during the Archaean and their subsequent thermo-mechanical evolution since the late Archaean and Proterozoic.

In Chapters 4 to 6 we have presented results which are focussed on the formation and early evolution in the first several hundred million years after the initiation of continental formation. It was shown there that after initiation, continental roots may have grown rapidly by addition from below of depleted peridotite in relatively small scale (± 50 km), hot and melt producing diapiric upwellings which intermittently penetrate the growing continental root.

Here we present results of numerical modelling which deal with the long term evolution of continents from their formation in the early Earth until the present. We also present an analysis of detailed temporal and spatial evolution of tracer particles which sample several physical quantities in the diapiric melting process.

Finally we have investigated the evolution of the ‘thermal age’ of evolving continental roots defined as the elapsed time since a sample of mantle rock has cooled below a hypothetical closing temperature. The results show a vertical layering in the thermal age, related to the mechanism of growth from below. This layering is disturbed laterally by thermal rejuvenation by hot diapiric upwellings which overprint existing thermal age during the later evolution.

7.2 Model description

The model used here is similar to the model described in more detail in Chapter 5. Important features of the model are: the use of a melting phase diagram for mantle peridotite with linear solidus and liquidus which practically limits occurrence of partial melting to the upper mantle above the transition zone at about 400 km depth. The mantle model is truncated at the upper to lower mantle boundary at 670 km depth. Thermal coupling between the upper mantle and the lower mantle and core is important in the thermal evolution models which operate on a time scale of several billion years where secular cooling of the Earth is significant. Therefore, we have extended the upper mantle model with a simple isothermal heat reservoir which accounts for the influence of lower mantle and core on the secular cooling of the upper mantle. The applied

	$t < 1150 \text{ Ma}$	$t > 1150 \text{ Ma}$
lowest x -resolution	3.116 km	
highest x -resolution	1.111 km	
N_x	698	
lowest y -resolution	15.0 km	1.764 km
highest y -resolution	0.922 km	0.922 km
N_y	302	590

Table 7.1: Used F -grid resolutions. The number of grid-points is given by N_x and N_y for x - and y -directions, respectively.

numerical modelling techniques (Chapters 6) consist of finite element solutions for the temperature T and the convective velocity field \vec{u} . The degree of depletion F is defined as the mass fraction of melt extracted from the partially melted mantle material. Due to the occurrence of small (km -) scale structure the F field is computed on a high resolution (sub- km -scale) structured grid. Passive particle tracers are advected with the mantle flow in order to monitor the F , T , pressure p , and thermal age t_{close} for several hypothetical closing temperatures T_{close} .

The total number of grid points of the F -grid was increased once during the model computations. The non-equidistant structured grid had relatively low resolution in the lower half of the upper mantle domain with respect to the shallower region during the first 1150 Ma of evolution. After $t = 1150 \text{ Ma}$ also small compositional structures develop in this deeper region. Therefore, the vertical grid resolution was increased for the lower half for the rest of the evolution up to $t = 4000 \text{ Ga}$. The minimum and maximum resolutions and the number of involved grid points are given in Table 7.1.

55,000 tracer particles were randomly distributed over the $2010 \times 670 \text{ km}$ large domain, and were used to track several quantities. On average, each particle thus represents an area of about 5^2 km^2 .

7.3 Modelling results

7.3.1 Model evolution up to 4 billion years

Figure 10.8 shows the long-term evolution of the continental upper mantle model. The left-hand-side column shows snapshots of the compositional field from 0.7 Ga to 4.0 Ga . On top of the depleted mantle the lower and upper crustal layers are represented as black and white areas, respectively. At corresponding times the lateral variations in the temperature fields, i.e. $T - \langle T \rangle_{hor}$, are depicted in the right-hand-side column of Figure 10.8. All frames for both the temperature and composition contain also instantaneous stream-lines of the convective velocity. Black and white lines correspond to clock and counter-clock wise flows, respectively.

Following the evolution in the F -field from 0.7 Ga to 2.5 Ga we see that the total volume of depleted continental root increases. After 2.5 Ga , this increase of the depleted volume has stopped. Mantle differentiation has apparently ceased between 2.5 Ga and 3.0 Ga .

The transition from root to mantle is set at the depth where $F \approx 10 \%$. Up to approximately 2.0 Ga the compositional layering is relatively undisturbed and the root extends to depths varying between 150 and 300 km . Afterwards, larger lateral variations

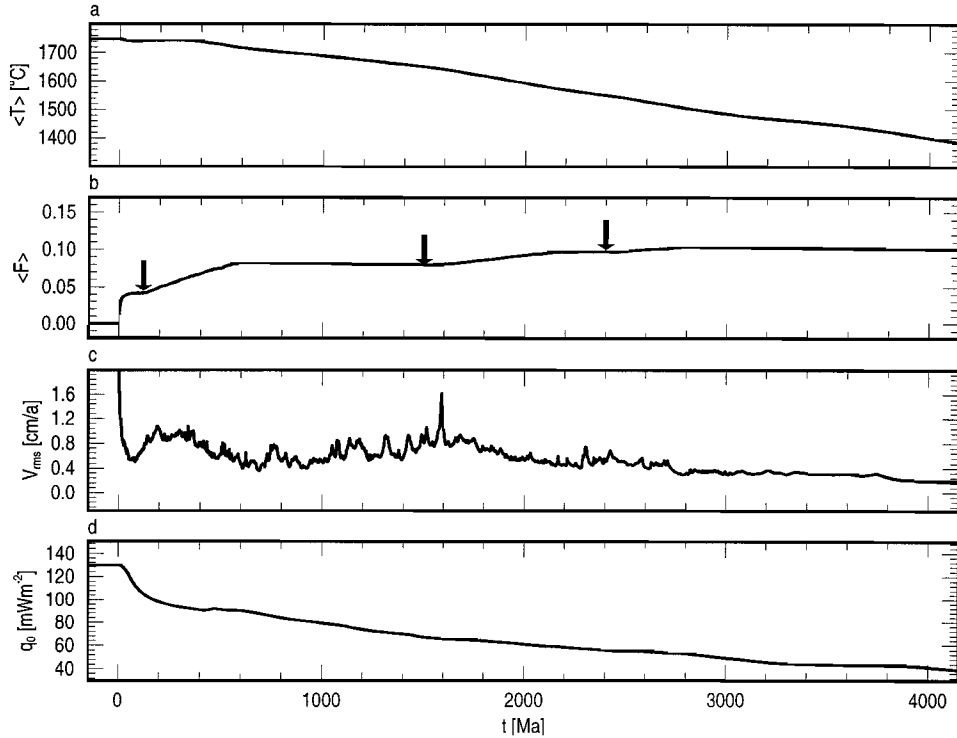


Figure 7.1: Evolution of some volume averaged quantities. **a** Temperature. **b** Degree of depletion. **c** Root-mean-square velocity for which the off-scale part is shown in (De Smet et al., 1998b). The averaged surface heat flow value is depicted in **d**.

in the depth extend evolve as a result of large broad upwellings in the undepleted mantle. A catastrophic large-scale overturn is, however, not observed during the investigated time-window. Depleted continental root delaminates by relatively small thread-like structures, which sometimes reach the upper to lower mantle transition depth. As a result, spirals of delaminated depleted material develop slowly as is observed in the F -field at 4.0 Ga .

From the decrease in the density of stream-lines in Figure 10.8 with proceeding evolution it is concluded that the vigor of convection is gradually decreasing. Despite these sluggish convection rates, the compositional state of the upper mantle does show significant variations during the last one billion years of evolution shown.

The lateral variations of temperature in the right-hand-side column of Figure 10.8 show that cold areas coincide with thick depleted continental roots. The maximum temperature is $2216^{\circ}C$ at $t = 1.5 Ga$ and decreases to $2058^{\circ}C$ at $t = 4.0 Ga$. Most thermal anomalies have amplitudes of about $300^{\circ}C$, and the maximum positive thermal anomaly of the shown snapshots is $616^{\circ}C$ at $t = 2.0 Ga$.

Figure 7.1 shows the evolution of several global quantities. The volume averaged temperature in Figure 7.1.a illustrates that secular cooling occurs at an almost constant rate. The drop in the volume averaged temperature due to cooling from the top is $340^{\circ}C$ from $1740^{\circ}C$ to $1400^{\circ}C$.

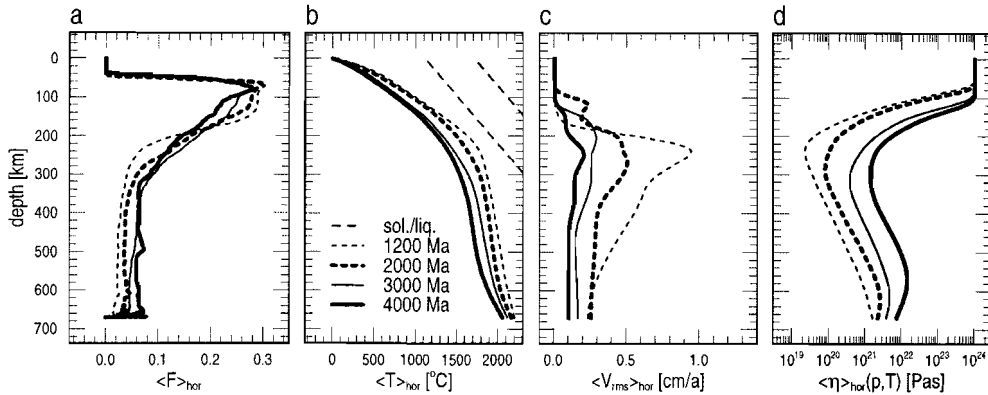


Figure 7.2: Horizontally averaged profiles at several stages of the model evolution. **a** Degree of depletion. **b** Temperature. **c** Velocity root-mean-square. **d** Viscosity. The dashed curves in **b** are the solidus and liquidus equilibrium lines.

Figure 7.1.b shows the evolution of the volume averaged degree of depletion $\langle F \rangle$. After the initial generation of the continental root, completed at about 50 *Ma*, three episodes follow during which the total volume of depleted material increases. The onset of these partial melting periods is marked with arrows. In spite of the overall secular cooling, upwellings apparently still cross the solidus. During the last 1.2 *Ga* of evolution the value for $\langle F \rangle$ remains constant because mantle differentiation has stopped after 2.8 *Ga* of evolution. If we assume that the initiation of continent formation in the model corresponds to 4.0 *Ga b.p.*, the melt production stopped 1.2 *Ga b.p.*, i.e. the late Proterozoic. Several suggested continental growth curves (Windley 1995) show a major surge of continental growth during the Mid and Late Archaean followed by a more slowly and steadily increase in crustal volume.

Figure 7.1.c illustrates that convection rates slowly decrease. Besides, the amplitude of the variations in the V_{rms} decrease with time. This is caused by the progressive cooling, which results in a significant increase in the overall viscosity.

Figure 7.1.d shows the averaged heat flow through the Earth's surface q_0 . Starting at high values of about 120 mWm^{-2} , values decrease to approximately 40 mWm^{-2} after 4.0 *Ga*. Such a low surface heat flow value is reasonable for a present-day cratonic shield area (Chapman 1986; Pollack et al. 1993). The steep decrease in q_0 during the early evolution of the model is followed by a much more steady decrease.

Figure 7.2 shows several horizontally averaged quantities at four moments in time. Figure 7.2.a shows the horizontally averaged profiles for F . Due to delamination vertical redistribution of depleted rock occurs. This results in an increase in $\langle F \rangle_{hor}$ in the 300 to 650 *km* depth range.

Figure 7.2.b shows the horizontally averaged temperature of the upper mantle model. Although the geotherm is below the solidus (dashed), partial melting events take place in upwellings associated with thermal anomalies that cross the solidus. After prolonged evolution, a thermal boundary layer (TBL) develops at the bottom. This is due to the thermal inertia of the heat reservoir of the lower mantle and core which buffers the cooling of the upper mantle. The decrease in temperature of the shallow model region is enhanced by the decrease in radiogenic heating, which is concentrated in the crustal layers.

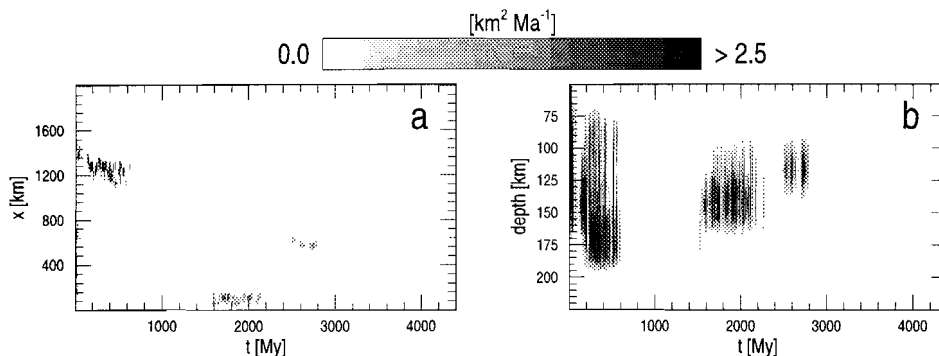


Figure 7.3: The horizontal (a) and the 1-D depth (b) melt production distribution as a function of time. Note the three long distinct periods of partial melting (a + b), and the decrease in time of the depth range of melt production (b).

Figure 7.2.c shows a dramatic decrease of the horizontally averaged convection rates from a maximum value of about 1 cma^{-1} at $t = 1.2 \text{ Ga}$ to 0.2 cma^{-1} at 4.0 Ga . Also the vertical variations in convective velocities diminish with proceeding evolution.

Figure 7.2.d shows the evolving viscosity profile. The strong increase in viscosity is the main cause for the decrease in V_{rms} . The decrease in averaged mantle temperature results in a less pronounced minimum viscosity in the asthenospheric layer underneath the growing MBL. The minimum value of the viscosity increases considerably by approximately two orders of magnitude from $5 \cdot 10^{19}$ to $5 \cdot 10^{21} \text{ Pas}$ during 3 Ga . The shallow region of the continental root is stabilised by the growth of the MBL at the top. The slowly evolving TBL at the bottom causes an inversion in the deeper upper mantle viscosity profile.

Figure 7.3 shows the distribution of melt productivity versus time integrated over vertical columns (7.3.a) and horizontal rows (7.3.b). Up to 2.8 Ga three episodes of upper mantle differentiation can be recognized: from $120 - 600 \text{ Ma}$, $1.5 - 2.2 \text{ Ga}$, and $2.5 - 2.8 \text{ Ga}$. Apparently, the continental upper mantle system experiences quiescent periods during which no intermittent melting occurs. During evolution the maximum depth of melting decreases (Figure 7.3.b) because of the decrease in mantle potential temperature with time. At the same time the growth of the MBL increases the minimum depth to which melt producing diapirs can rise.

7.3.2 Detailed dynamics of diapiric partial melting

In order to investigate the patterns of mantle differentiation in greater detail we applied a set of tracer particles. Each single tracer in the set tracks the histories of the degree of depletion F , the temperature T , and its position (x, z) .

Figure 10.9 shows several enlargements of a region where mantle differentiation occurs. The time-window from 401 to 500 Ma is part of the first period of intermittent melting events shown in Figure 7.3. The positions of nine tracers are shown for eight snapshots, which are unevenly spaced in time. The relation between tracer symbols and corresponding numbers is given in the red legend at the bottom right-hand-side of Figure 10.9.

In Figure 10.9.a four tracers (# 1, 4, 6, 7) are situated in the undepleted mantle at

about 350 km depth at $t = 401 \text{ Ma}$. Following the tracer positions in time shows that they are part of a hot melt producing diapir that impinges on the continental root (Figures 10.9.b-h). They reach depths between 60 and 100 km and spread both laterally and vertically in the root. Their relative positions illustrate the vorticity of the mantle flow in the region where melting occurs. Furthermore, the central region of the mantle diapir, which exhibits a low F value during early ascend does not differentiate much further during the remaining ascend. This is illustrated by the F -values of tracers 1 and 4 in Figures 10.9.c and 10.9.e.

The tracers 2 and 3 are in close proximity to each other at $t = 401 \text{ Ma}$ (Figure 10.9.a) where they are part of the lowly depleted deeper part of the root. At $t = 420 \text{ Ma}$ (Figure 10.9.f) they have a much larger mutual distance. During the time-window shown, they are mainly subject to lateral movement in the deeper part of the root where their degree of depletion is not altered.

Tracers 8 and 9 are subject to recurrent melting. Figure 7.4.a and 7.4.b shows the (p, T, t) - and (p, F, t) -paths of tracer number 9 for the 401-500 Ma time-window. At point **A** the tracer has a low value of F and it slowly ascends to point **B** ($t = 413 \text{ Ma}$). At this point, the tracer starts to rise much faster and it crosses its solidus at $F = 10 \%$. This ascend stops at point **C** where $F = 19 \%$. Here, a relatively slow vertical movement around a depth of 125 km (4.2 GPa) is observed until $t = 450 \text{ Ma}$, when a further ascend to point **D** starts. Recurrent melting from **C** to **D** increases the degree of depletion to 26 %. The uprise continues more slowly and without melting to point **E** after which the tracer descends to higher pressure (point **F**). It circulates back upward to point **G**, but is too cold to initiate another cycle of recurrent melting.

Three (p, T, t) -paths and corresponding (p, F, t) -paths are given in Figure 7.5.a and 7.5.b, respectively. Each tracer is approximately situated in the center of a melting diapir. They correspond to the three main periods of differentiation (see Figure 7.3). The final position of each tracer for the displayed time-window corresponds to the indicated time. The path marked with open squares corresponds to tracer # 1 which is indicated with the same symbol in Figure 10.9.

The subsolidus ascend of material occurs adiabatically and the corresponding potential temperatures T_{pot} are given in Figure 7.5.a. The mantle temperature decreases with time and partial melting therefore starts at shallower depths, since the solidus is crossed at lower pressures. A hotter upwelling is capable of producing more melt over a larger depth interval and reaching higher degrees of depletion (Figure 7.5.b). This was also observed in the melt productivity shown in Figure 7.3. When the upper mantle cools further, the MBL at the top of the mantle grows (Figure 7.2.d), which prevents the diapirs from penetrating the root to shallow levels. The presence of the MBL at the end of the melting path prevents further ascend after which the tracer becomes part of the stagnant layer and cools further by conductive heat loss. This is consistent with the (p, T, t) -paths derived for upper mantle samples described by Roermund and Drury (1998).

Highly depleted material is positioned directly underneath the crust during early evolution. After cooling from the top this material is trapped and can be brought to the surface during later evolution in the form of xenoliths. Bernstein et al. (1998) describes such xenoliths that contain highly depleted mantle material ($\sim 40 \%$) originating from depths of 1 – 2 GPa.

After melting has stopped, the depleted residual material becomes part of the continental root. It maintains its attained F -value except for small effects of numerical diffusion, which causes the slow decrease in depletion observed at low pressures for the

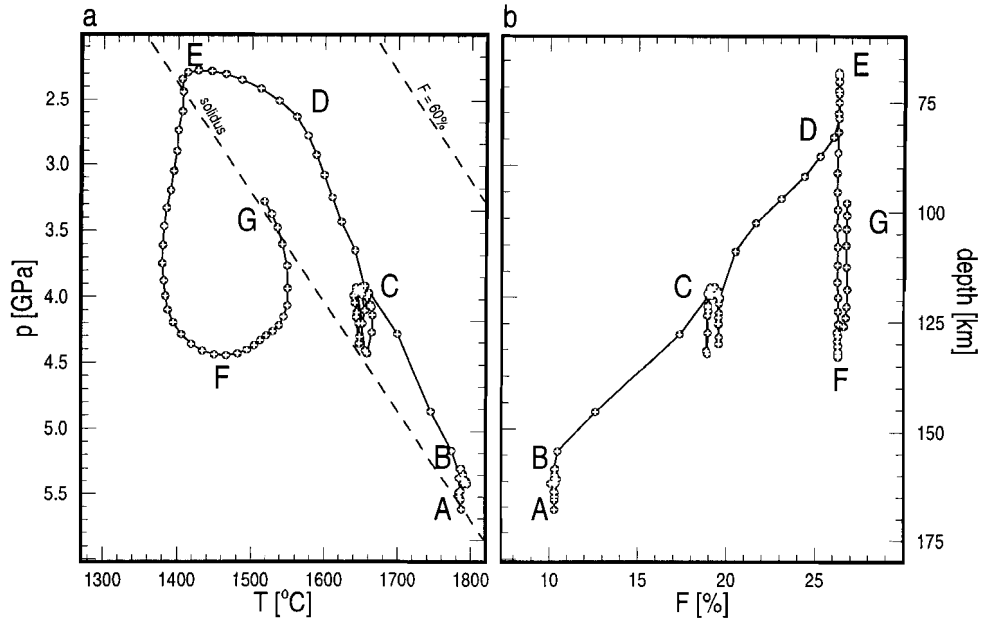


Figure 7.4: **a** (p, T, t) -path for tracer that represents a mantle volume subject to recurrent melting. Time increment between symbols as indicated in the paths is 1 Ma . **b** To **a** corresponding (p, F, t) -path. The symbol used in **a** and **b** corresponds to the tracer depicted with the same symbol in the contour plots for the F -field in Figure 10.9.

tracer path marked with crosses in Figure 7.5.b. The two cold tracers in Figure 7.5.b are already modestly depleted ($F = 3.5\%$) during upwelling before reaching the solidus. This is caused by the mixing of delaminated depleted material in the deeper mantle due to the finite amount of numerical diffusion, which acts as an artificial mixing mechanism in the numerical model.

Tracers in Figure 7.6.a and 7.6.b are involved in convective cycles with an aspect ratio of about one. During the 4 Ga of evolution they experience approximately nine overturns.

7.3.3 Comparison with theoretical geotherms

We compare the global and local thermal state of the upper mantle model at $t = 4\text{ Ga}$ with theoretically derived continental geotherms for present-day cratonic situation. The heat flow through the surface of the model has dropped to an averaged value of 41 mWm^{-2} at this point in the evolution. Surface heat flow measurements for cratonic shields with an age of more than 3.5 Ga range between 30 and 50 mWm^{-2} (Pollack et al. 1993). Since the model heat flow value is within this interval after 4 Ga of evolution, we compare this model state with the theoretical cratonic thermal model used by Chapman (1986) and Pollack et al. (1993). This model is thought to be valid for the relatively shallow part of the shield where conductive heat transport is dominant.

The model crustal thicknesses and heat flow values in combination with the incorporated radiogenic heat generation at $t = 4\text{ Ga}$ are used as the parameters for the

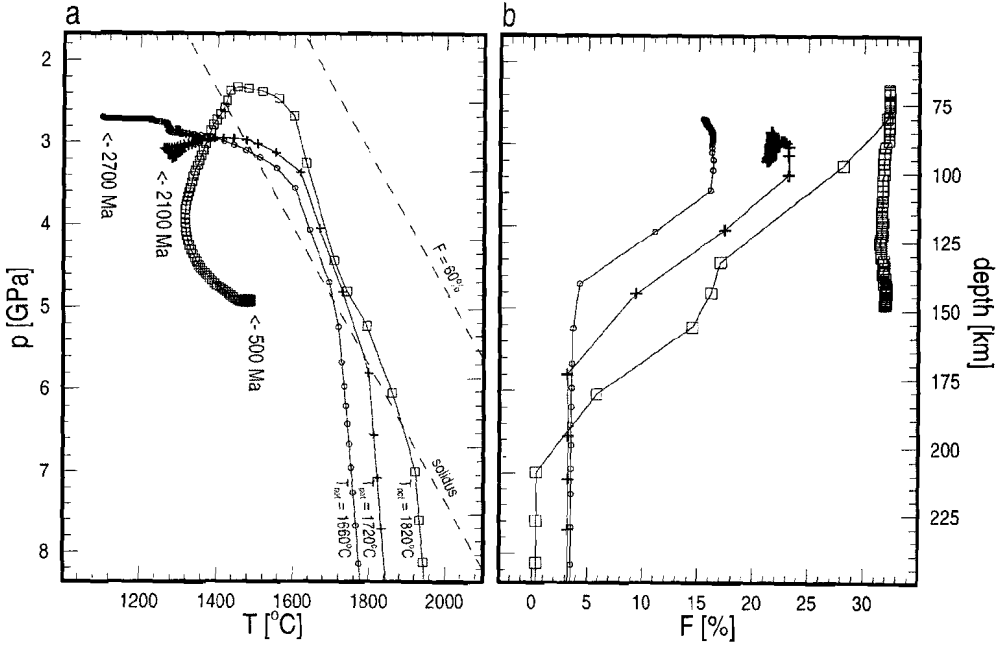


Figure 7.5: a (p, T, t) -paths for three tracers. They correspond to tracers approximately positioned in the heart of different melt producing diapirs that impinge on the continental root. The final position of each tracer for the displayed time-window corresponds to the indicated time. Elapsed time between the symbols is 1 *Ma*. The hot and cold tracer correspond to the first and last period of melting, respectively. Tracer potential temperatures are indicated. Time increment between symbols is 1 *Ma*. b (p, F, t) -paths corresponding to a. The tracer path indicated with open squares in a and b is the tracer depicted with the same symbol in the contour plots for the F -field in Figure 10.9.

theoretical geotherm computation as given by Chapman (1986). Note that the heat productivity in the 2-D convection models is based on the data also given by this author. In the model the exponential depth distribution of the heat productivity in the upper crust is simplified to an equivalent uniform value. We therefore give two theoretical geotherms: one corresponding to the exponential distribution of radiogenic heating according to Chapman (1986) and one with the equivalent uniform value. Furthermore, at large depths advective heat transport becomes more important and the theoretical geotherm deviates significantly from the results derived from the convection model.

Figure 7.7 shows three temperature profiles derived from the convection model (Figure 7.7.a to 7.7.c), and Figure 7.7.d is the horizontally averaged state of the model. They can be compared to the corresponding theoretical geotherms defined by Chapman (1986). The thin solid lines are for an exponential distribution of radiogenic heating in the upper crust. The surface heat flow of the model are given in each frame. Lateral variations of the lower and upper crustal thicknesses in the model (see Figure 10.8) are taken into account. It can be concluded from Figure 7.7 that for shallow depths (< 200 km) the geotherms derived from the convection model are in reasonable agreement with the continental geotherms according to Chapman (1986).

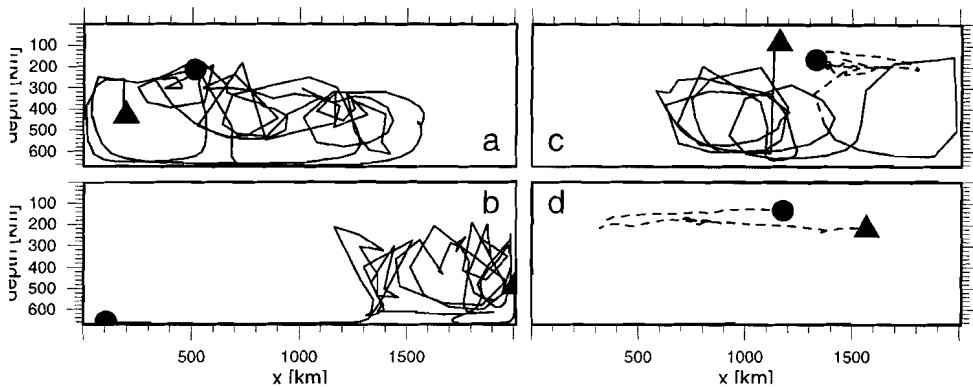


Figure 7.6: Tracer location during the model evolution. Circles and triangles indicate start ($t = 50 \text{ Ma}$) and end ($t = 4 \text{ Ga}$) positions. Solid lines indicate that a tracer is part of the mobile part of the upper mantle (not necessarily $F = 0$). Dashed lines indicate that a tracer is located in a stable part of the continental root. The connects tracer locations separated by 25 Ma . **a+b** Two tracers which remain part of the undepleted mantle. **c** A tracer which is part of the depleted root during the first 2150 Ma after which time it is transported in a delamination event into the mobile mantle below the root where it remains. **d** Tracer which is part of the stable continental root.

7.3.4 Age and compositional structure of continental roots

The mechanism of continental formation and evolution resulting from the mantle convection model presented here produces a specific structure of the continental root expressed in the thermally defined age and the composition. Samples of deep continental root material brought up as xenoliths and peridotite massifs have been used to derive information about (p, T)-conditions (Finnerty and Boyd 1987; Boyd 1987) age (Boyd et al. 1985; Boyd and Gurney 1986; Pearson 1997) and composition (Jordan 1979; Griffin et al. 1984; Griffin et al. 1996) of the upper mantle below continents. Here we present similar observables derived from the numerical modelling results.

The same set of tracers used in the previous section has been used to investigate the structure and evolution of the thermally defined age of the continental root. The thermal age t_{close} is defined here as the time elapsed since a rock sample cooled below a hypothetical closing temperature T_{close} . In the model calculations, the temperatures of a set of tracer particles is monitored at every time-step. When a tracer cools below the closing temperature the current model time value is stored. The closure time is reset when the closing temperature is exceeded during a later event. This thermal rejuvenation can occur by reheating during thermal events. Results are presented for several hypothetical closing temperatures ranging from 600 to 1200°C with intervals of 200°C . This is within suggested upper mantle ranges (Mezger et al. 1992). The state of the model after 4 Ga of evolution is assumed to correspond to the present-day situation, i.e. $t = 4 \text{ Ga} = 0 \text{ Ma b.p.}$

In the left-hand-column of Figure 7.8 the evolution of the closure time is given for $T_{close} = 1200^\circ\text{C}$ for snapshots starting at 2.5 Ga b.p. and ending at 0 Ga b.p. with 0.5 Ga intervals. Note that the depth-scale is twice the x -scale to emphasize the details. Deep, white coloured areas indicate that the temperature of the material is higher than T_{close} . White upper mantle areas just underneath the crustal layers have temperatures below the T_{close} from the onset of evolution. The corresponding temperature fields are

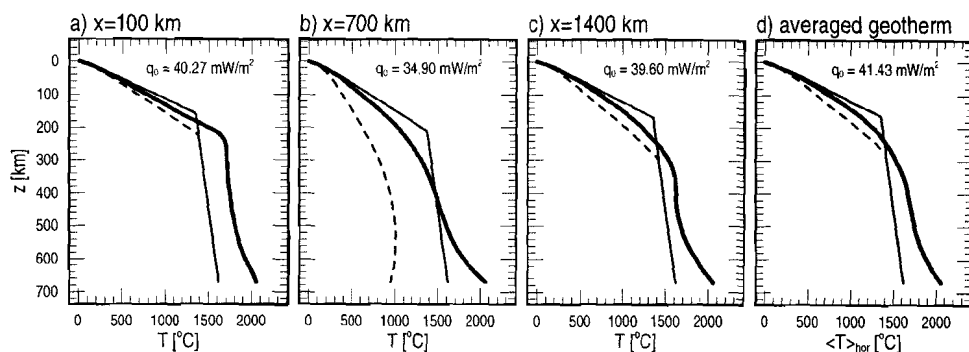


Figure 7.7: a + b + c Geotherms derived from the convection model (thick solid line) at 4000 *Ma* at several *x*-locations as indicated above each frame. The last frame (d) shows the averaged temperature profile. The thin dashed and solid lines are theoretical continental geotherms as described by the model of Chapman (1986) where the heat flux at the surface (q_0) is obtained from the model. The deeper part of the theoretical curves are defined by an adiabatic geotherm corresponding to a present-day potential temperature of 1280°C (McKenzie & Bickle 1988). The colder dashed geotherms corresponds to the uniform upper crustal radiogenic heat production at 4000 *Ma* as incorporated in the model. The solid thin line corresponding to an exponential distribution in the upper crust.

given in the right-hand-side column.

At 2.5 *Ga b.p.* there is a shallow feature in the 1200 < *x* < 1400 *km* range, which reaches the lower crust. This is the result of an older hot temperature anomaly, the remnant of a mantle diapir timed at 3.5 *Ga b.p.*, no longer visible in the temperature field. A similar event is observed from 2.5 to 1.0 *Ga b.p.* at a slightly greater depth in the 100 < *x* < 300 *km* range. The thermal anomaly that caused this feature is slowly disappearing as is illustrated by the temperature field at 2.5, 2.0, and 1.5 *Ga b.p.*. This region at the left ‘closes’ within 1 *Ga* up to a depth of almost 200 *km*.

Over a depth range of 125 < *z* < 225 *km* between *x* = 1000 *km* and *x* = 1300 *km* rock has reached temperatures less than 1200°C at 1.0 *Ga b.p.*. During the next 500 *Ma* of evolution, a hot upwelling resets these closure times after which the rock ‘closes’ again from 0.5 *Ga b.p.* on. A similar smaller scale process has been active between 2.0 and 1.0 *Ga b.p.* around *x* = 600 *km*.

Similar patterns are also observed for the lower range of T_{close} . Figure 7.9 shows continental thermal age structures for different closing temperatures (600, 800, and 1000 °C) at 0 *Ma b.p.*. The effect of cooling from the top is reflected in the differences between the patterns of closure times at different closing temperatures.

Vertical profiles of the closure times and degree of depletion at 0 *Ma b.p.* are given in Figure 7.10.a at three horizontal positions identical to those given in Figure 7.7.

Lateral variations in thermal history are illustrated by the differences between the frames in Figure 7.10.a1-a3. The sub-horizontal parts of these curves are the result of thermal rejuvenation, resetting the thermal age beneath the secularly growing MBL. For instance, the fast drop to greater depth of the t_{close} -curves in Figure 7.10.a2 at $t_{close} = 1.3$ *Ga b.p.* is related to the accelerated shift of the isotherms to greater depth. This thermal shift starts between 1.5 *Ga b.p.* and 1.0 *Ga b.p.*, at *x* = 700 *km* as shown in the temperature frames of Figure 7.8.

The stratification of the compositional layering in the continental root and its lateral variation are illustrated in Figure 7.10.b1-b3 for the same horizontal positions as those

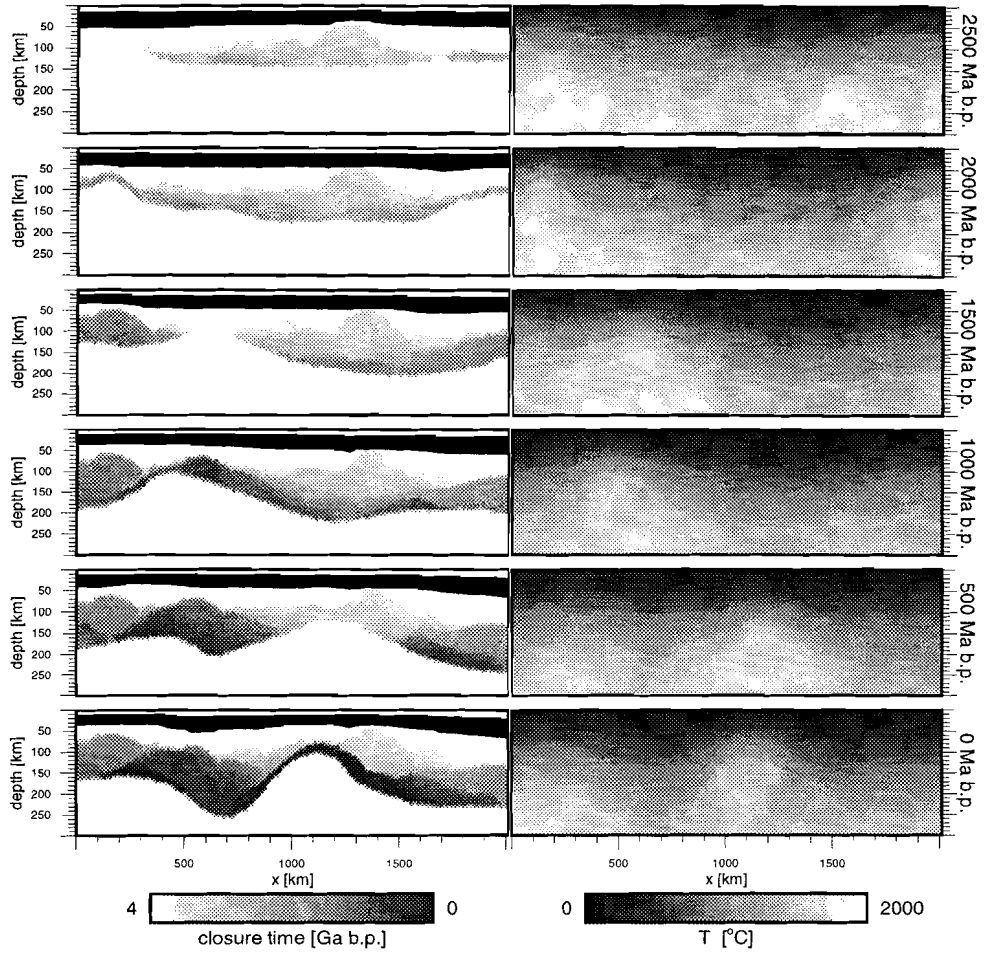


Figure 7.8: Evolution of the closure time (left-hand-side column) for a closing temperature of 1200°C at the same times as in Figure 10.8 when $4000 \text{ Ma} = 0 \text{ Ma b.p.}$ is assumed. The white deep regions are still above the closure temperature. The corresponding temperature fields are depicted in the right-hand-side column. Note that the depth-scale is exaggerated twice with respect to the x -axis to emphasize the details.

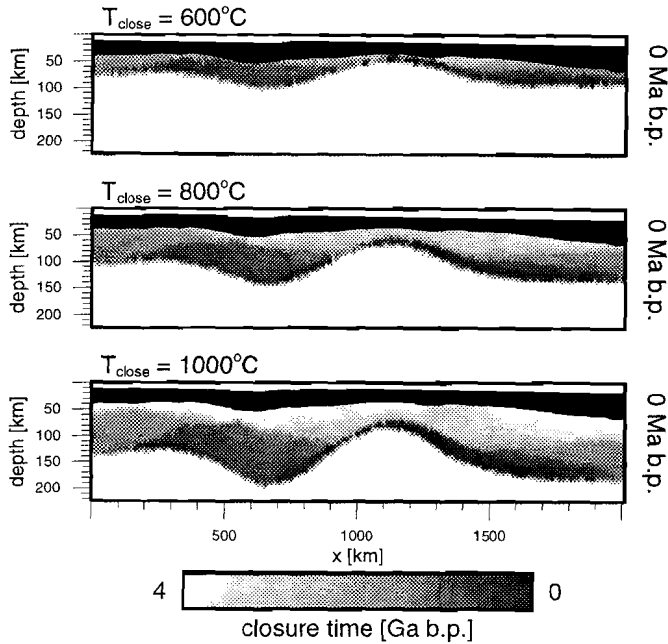


Figure 7.9: The closure time fields at 0 Ma b.p. for closing temperatures of 600, 800, and 1000°C from top to bottom when $4000 \text{ Ma} = 0 \text{ Ma b.p.}$ is assumed. The depth-scale is exaggerated twice with respect to the x -axis. The white deep regions have not yet cooled far enough and therefore not sank below the closure temperature.

given in Figure 7.10.a1-a3. The detailed structure shown in these profiles is numerically well resolved. Maximum values of $F = 30\%$ are found at shallow sub-crustal levels corresponding to the oldest depleted material in the model that was in a hot mantle during the initial phase of continental formation. This material might correspond to the strongly depleted material found in mantle xenoliths originating from shallow depths as reported by Carswell et al. (1984) and Bernstein et al. (1998). The results of partial remixing of material that delaminated from the continental root is illustrated by the finite amounts of F in the subcontinental mantle.

7.4 Discussion and conclusions

The numerical modelling results show that continental upper mantle which has been formed in a relatively short period during the Archaean remains gravitationally stable for at least 4 Ga . Although small scale delamination events occur, which result in remixing of depleted continental root material in the subcontinental mantle, no large scale collapse of the continental root occurs for the observed time window. This long term stability is due to the effect of the low density of the depleted residual peridotite. This is reinforced by the effect of the temperature dependence of the viscosity which results in the growth of the strong mechanical boundary layer during secular cooling. The thickness of the resulting continental root ($200 - 250 \text{ km}$) corresponds to similar

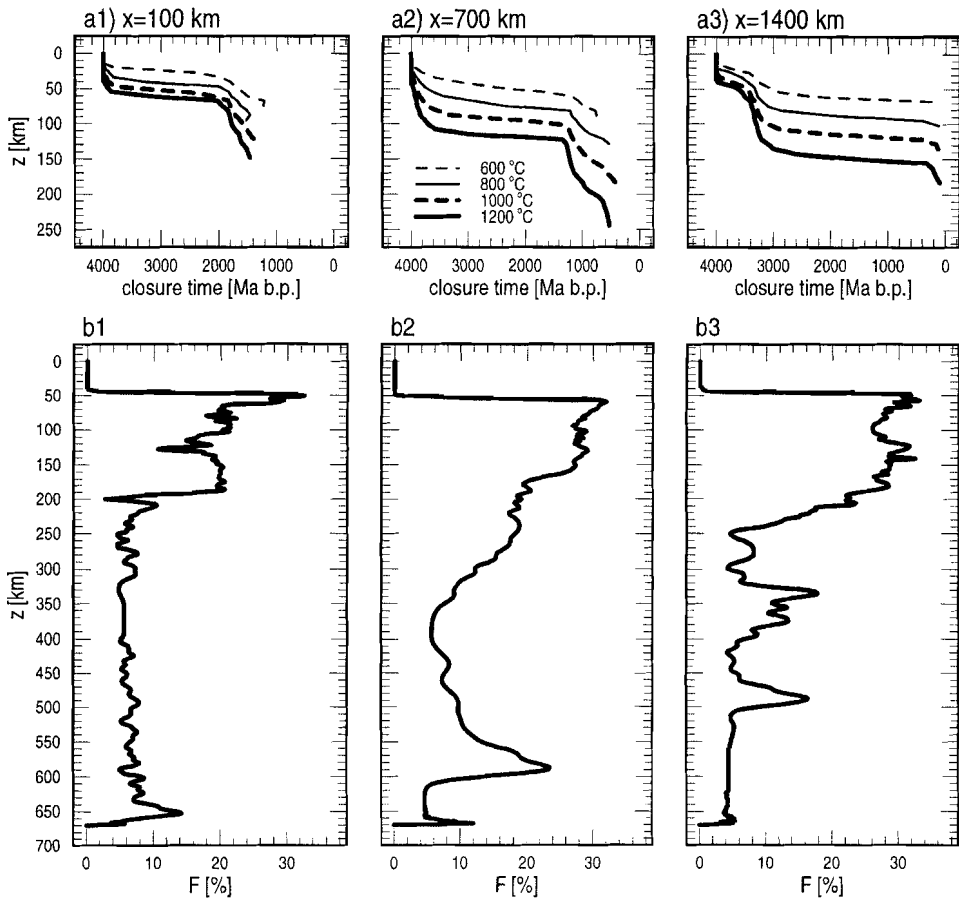


Figure 7.10: Profiles of the F -field (b) and four closure times (a) at three x -locations identical to the locations used for the profiles as given in Figure 7.7. The profiles correspond to $t = 4000 \text{ Ma} = 0 \text{ Ma b.p.}$ for which the closure temperature fields are depicted in Figures 7.8 and 7.9. The deeper region for which the closure time profile is not shown has temperatures higher than the indicated closing temperatures. The wiggles in the F -profiles (b) are resolved by the numerical method.

values reported from seismological observations (Woodhouse and Trampert 1995) although larger values have been reported also (Durrheim and Mooney 1994; Polet and Anderson 1995).

Detailed analyses of the (p, T, F, t) -paths illustrate the nature of recurrent melting in mantle diapirs which penetrate the continental root from below. The results show that partially melted material in the root can be entrained in diapiric upwellings, resulting in recurrent melting. The model (p, T, F, t) -paths show similarities with recent peridotite samples found in mantle xenoliths (Bernstein et al. 1998) and peridotite massifs (Roermund and Drury 1998). The analysis of the thermal age of the model continental root reveals a definite layering in the thermal age with the oldest material of about 4 Ga situated at shallow depth directly beneath the crust. This reflects the mechanism of continental growth from below. Lateral variation of the thermal age increases with depth in the continental roots due to thermal rejuvenation by diapiric events in the weaker deeper parts of the root during later evolution.

Several limitations of the model should be considered. First the model configuration is limited to a completely continental upper mantle. This prevents lateral heat transport from the subcontinental mantle, which would enhance the secular cooling (Nyblade and Pollack 1993; Pollack 1997). On the other hand the strengthening effect of devolatilization on the rheology of the depleted mantle root, which would slow the convective cooling and increase the mechanical stability has also been neglected in the present model (Karato, Paterson, and Fitz Gerald 1986; Pollack 1986; Karato and Jung 1998). Geotherms derived from the numerical modelling results after 4 Ga of secular cooling are in agreement with the theoretical present-day geotherms as given by (Chapman 1986), at least for the shallow lithospheric regime, where conductive transport is dominant. Thermal evolution of the upper mantle shows a drop in average temperature of about 340 K and a decrease in surface heat flow from 100 to about 40 mWm^2 after 4 Ga. This is in reasonable agreement with estimates from whole mantle parameterized convection models (Jackson and Pollack 1984).

Chapter 8

SEISMIC VELOCITY STRUCTURE OF THE ROOT INFERRED FROM THE MODEL

8.1 Introduction

The parameterization of the gradual decrease in the density of the residual upper mantle rock ρ_s with increasing degree of depletion F (Equation 2.1) is based on the work presented by Jordan (1979). He also relates the degree of depletion to other relevant quantities. Here, his results are used to determine the structure of the seismic compressional wave velocity V_p , and the seismic shear wave velocity V_s at reference pressure ($p_{srf} = 0 \text{ Pa}$) and temperature ($T_{srf} = 0^\circ\text{C}$) from the model values of F . The effects of the pressure p , and temperature T on the velocities is superpositioned onto the effect of F . The (p, T, F) -state is given by the modelling results for $t = 4 \text{ Ga}$ (i.e. $t = 0 \text{ Ga b.p.}$, see Chapter 7). The resulting first order approximation of the seismic wave velocity structure is compared to observations.

8.2 Seismic velocity parameterizations

The data presented by Jordan (1979) that relate density and magnesium number $Mg\#$ of residual mantle rocks are shown as dots in Figure 8.1.a. Also shown is the linear fit, which is determined here. Equating the determined $\rho(Mg\#)$ and $\rho_s(F, T_{srf}, p_{srf})$ yields the following relation:

$$Mg\#(F) = 0.868 + 0.153 \cdot F \quad (8.1)$$

plotted in Figure 8.1.b. Other compositional effects and the effect of anelasticity are not taken into account here.

The change in seismic velocities with varying $Mg\#$ has also been determined by Jordan (1979). His data are shown in Figure 8.2.a and 8.2.b together with a linear fit for both seismic velocities, respectively. The fits determined here result in the following linear relations:

$$\begin{aligned} V_p(F, T_{srf}, p_{srf}) &= V_p(T_{srf}, p_{srf}) + \Delta V_p \cdot F = 8.210 + 0.290 \cdot F \text{ km.s}^{-1} \\ V_s(F, T_{srf}, p_{srf}) &= V_s(T_{srf}, p_{srf}) + \Delta V_s \cdot F = 4.758 + 0.268 \cdot F \text{ km.s}^{-1} \end{aligned} \quad (8.2)$$

These relations are shown in Figure 8.3.

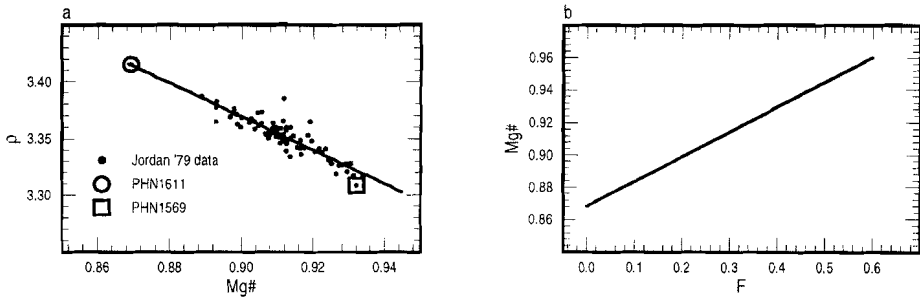


Figure 8.1: **a** Data relating density and Magnesium number according to Jordan (1979) are plotted as dots. The open circle indicates the relatively undepleted rock PHN 1611. The relatively far depleted rock PHN 1569 plots at the open square. The line is the linear fit to these data. **b** The linear fit of **a** results in this linear relation between degree of depletion and Magnesium number after equating the two density relations: $\rho(F) = \rho(Mg\#)$.

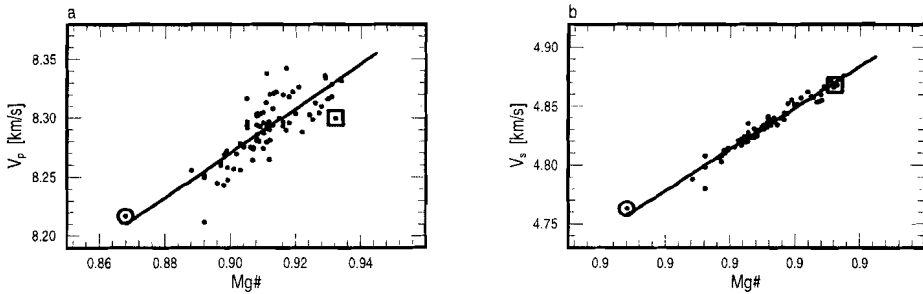


Figure 8.2: Data and parameterization of the residual rock composition versus the seismic velocities according to Jordan (1979). **a** Compressional wave velocity. **b** Shear wave velocity. Symbols are as given in Figure 8.1

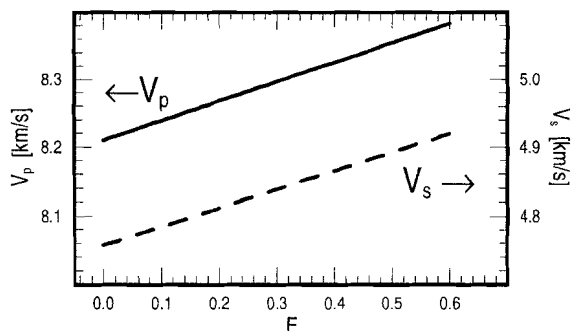


Figure 8.3: Parameterizations of the seismic velocities with varying degree of depletion. Both the compressional wave velocity and the shear wave velocity follow a linear relation over this F -interval.

In the following we neglect the effect that anelasticity has on the velocities, which is thought to be a good approximation for depths up to about 200 km (Karato 1993; Goes, Govers, and Vacher 1999). From $\rho_s(F, T_{srf}, p_{srf})$ the shear modulus G_m is determined by the expression for the shear wave velocity at reference temperature and pressure:

$$V_s(F, T_{srf}, p_{srf}) = \sqrt{\frac{G_m(F, T_{srf}, p_{srf})}{\rho(F, T_{srf}, p_{srf})}} \quad (8.3)$$

The corresponding bulk modulus K_m follows from the found value for G_m and the compressional velocity V_p . The expression for the pressure wave velocity is:

$$V_p(F, T_{srf}, p_{srf}) = \sqrt{\frac{K_m(F, T_{srf}, p_{srf}) + \frac{4}{3}G_m(F, T_{srf}, p_{srf})}{\rho(F, T_{srf}, p_{srf})}} \quad (8.4)$$

The ranges in bulk and shear modulus determined this way are:

$$\begin{aligned} 125.8 &< K_m(F, p_{srf}, T_{srf}) < 127.1 \text{ GPa} \\ 77.33 &< G_m(F, p_{srf}, T_{srf}) < 78.6 \text{ GPa} \end{aligned} \quad (8.5)$$

They follow from the range in F at $t = 4 \text{ Ga}$: $0 < F < 35.7 \%$. They are consistent with the data compiled by Vacher et al. (1998) when we assume that olivine is the abundant mineral. Pressure and temperature effects are incorporated through p, T -dependencies of K_m, G_m , and ρ_s :

$$\begin{aligned} K_m(F, T, p) &= K_m(F, T_{srf}, p_{srf}) + \left(\frac{\partial K_m}{\partial p}\right)_{T_{srf}} (p - p_{srf}) + \left(\frac{\partial K_m}{\partial T}\right)_{p_{srf}} (T - T_{srf}) \\ G_m(F, T, p) &= G_m(F, T_{srf}, p_{srf}) + \left(\frac{\partial G_m}{\partial p}\right)_{T_{srf}} (p - p_{srf}) + \left(\frac{\partial G_m}{\partial T}\right)_{p_{srf}} (T - T_{srf}) \\ \rho_s(F, T, p) &= \rho_s(F, T_{srf}, p_{srf}) + \frac{1}{K(F, T_{srf}, p_{srf})} (p - p_{srf}) - \alpha (T - T_{srf}) \end{aligned} \quad (8.6)$$

Note that the pressure effect in ρ_s is not incorporated in the numerical model. Vacher et al. (1998) give values for the partial derivatives which we adopted:

$$\begin{aligned} \left(\frac{\partial K_m}{\partial T}\right)_{p_{srf}} &= -0.016 \text{ GPaK}^{-1} & \left(\frac{\partial K_m}{\partial p}\right)_{T_{srf}} &= 4.5 \\ \left(\frac{\partial G_m}{\partial T}\right)_{p_{srf}} &= -0.014 \text{ GPaK}^{-1} & \left(\frac{\partial G_m}{\partial p}\right)_{T_{srf}} &= 1.45 \end{aligned} \quad (8.7)$$

With these values the seismic velocities are given by:

$$V_s(F, T, p) = \sqrt{\frac{G_m(T, p)}{\rho_s(F, T, p)}} \quad V_p(F, T, p) = \sqrt{\frac{K_m(T, p) + \frac{4}{3}G_m(T, p)}{\rho_s(F, T, p)}} \quad (8.8)$$

where F, T , and p are determined by the model.

8.3 Results

8.3.1 Vertical velocity profiles

Figure 8.4.a and 8.4.b show the resulting profiles for V_p and V_s , respectively. The thick and thin lines are the profiles with and without incorporating the effect of F ,

respectively. They correspond to the modelling results at $t = 4 Ga = 0 Ma b.p.$. Snapshots of $T - \langle T \rangle_{hor}$ and F are shown in Figure 10.8. The two local profiles at $x = 100$ and $1810 km$ show a sharp minimum at the depth where the transition from depleted root to the deeper upper mantle takes place. The F -field at $t = 4 Ga$ (Figure 10.8) shows that the depth extend of the root at $x = 100 km$ and $x = 1810 km$ is $\sim 220 km$ and $\sim 320 km$, respectively. The horizontally averaged profiles given in Figure 8.4 (grey lines) show a less clear minimum due to the large variations in model continental root thicknesses.

Velocity profiles corresponding to a present-day oceanic lithosphere are also given in Figure 8.4 for comparison. They correspond to the thermal situation at a MOR when conductive cooling from the top down has not yet effected the geotherm. The potential upper mantle temperature is $T_{pot} = 1280^\circ C$ and the same partial melting phase diagram as used in the continental model is applied. The velocity profiles are determined for T - and F -profiles that follow from the 1-D model as used in Chapter 9. In the deeper part of the upper mantle the oceanic seismic velocities are higher than the continental velocities due to the higher modelled continental temperatures in this depth range (see Figure 7.7). The temperature at large depths in the continental model is closer to a $1450^\circ C$ adiabat (see Figure 7.7). The corresponding velocity profiles for this hotter situation is also given. In the shallower part, the large difference in seismic velocities is caused by the relatively high oceanic mantle temperatures. They are overestimated, due to the absence of conductive cooling of the oceanic lithosphere.

Comparison of the thin and thick lines in Figures 7.10.a and 7.10.b shows the effect that the compositional variation has on the seismic velocities. Disregarding the compositional effect results in a reduction of seismic velocities. The maximum differences in V_p and V_s are located just underneath the crust and are approximately 1 % ($0.08 km s^{-1}$) and 1.7 % ($0.08 km s^{-1}$), respectively. V_s is affected more by the composition than V_p . The overall pattern in the profiles, i.e. the low velocity zone, is caused by the T - and p -effects on the velocities, The F -field with its fine structures causes the small variations in the seismic velocity.

8.3.2 Seismic reflection coefficients

As suggested earlier (Section 4.4), the small-scale structure in F might be responsible for P-wave reflections found in continental lithosphere. P-waves are reflected when they cross an interface that separates two layers with distinct seismic impedances $I = \rho V_p$. The seismic reflection coefficient is given by $c = (I_2 - I_1)/(I_1 + I_2)$, where I_2 is the impedance of the layer underneath the layer with impedance I_1 .

Figure 10.10.b shows the c -field for a computation with $3.37 km$ thick layers. Crustal velocities are $6.2 km s^{-1}$ and $6.8 km s^{-1}$ for upper and lower crust (Mooney et al. 1998), respectively. The c -field corresponds to the result at $t = 4 Ga$ for which the F -field is shown in Figure 10.10.a. When layers twice as thick are used, only the amplitude of c changes. It clearly shows the relative impedance changes at the upper-lower crust transition and the transition from the lower crust to the lithospheric mantle. The elongated feature in c on the right-hand-side of the center (marked with an **A**) is caused by the large hot upwelling. It follows the transition from depleted to non-depleted material. The density and P-velocity vary more sharply than the pressure and temperature over this region where the sharp interface in degree of depletion is located. Separate changes in $V_p(F)$ or $\rho_s(F)$ result in negative and positive c -values, respectively. The effect of $\rho_s(F)$ on I is apparently dominant, since the relative impedance change

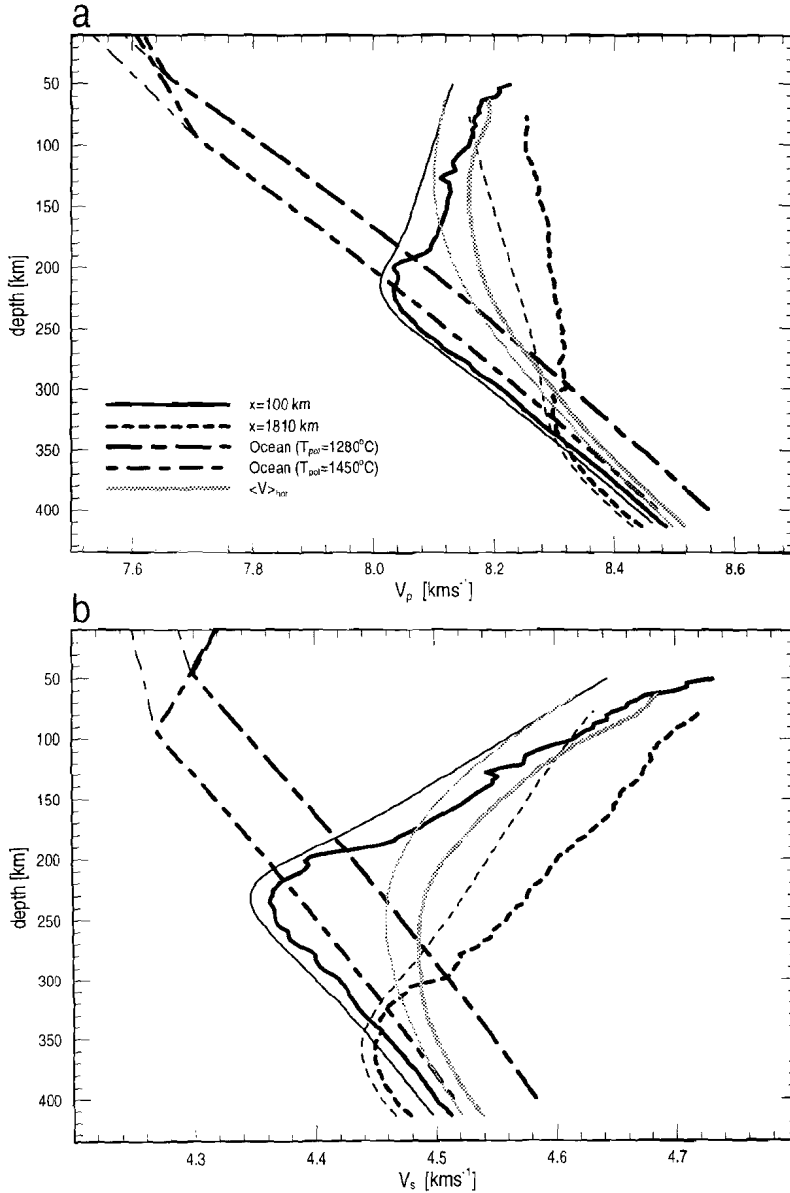


Figure 8.4: Seismic velocity profiles corresponding to the model results for $t = 4 \text{ Ga} = 0 \text{ Ma b.p.}$. Corresponding T - $\langle T \rangle_{\text{MOR}}$ - and F -fields are shown in Figure 10.8. The thick and thin lines are profiles determined with and without the effect of F , respectively. The result for two oceanic profiles following from the same model parameterization are given as thick dashed lines for comparison. They correspond to the MOR location, i.e. no effect of conductive cooling is incorporated, for a potential mantle temperature of 1280 and 1450°C. The former is thought to be representative for a present day situation. **a** Longitudinal wave velocity profiles. **b** Shear wave profiles.

in the results is positive.

In region **B** on the left many impedance changes are present up to a depth of ~ 200 km which are caused by the large compositional variations in that region (see Figure 10.10.a). The thick compositional continental root on the right ends at a depth of ~ 310 km where a change in relative impedance is present (**C**). The intermittent melting events that took place between $t = 120$ to 600 Ma resulted in the non-uniform distribution of depleted material in region **C** of the root. This compositional structure is still present at $t = 4$ Ga around zone **D** and it results in impedance discontinuities shown in the c -field. The impedance structure marked **E** is caused by a small thread-like volume of depleted material that previously delaminated for the root (see also Figure 10.8).

8.4 Concluding remarks

The first order velocity parameterization applied to the model result at 0 Ga *b.p.* shows that both the compositional and the thermal state of the modelled continental upper mantle determine the seismic velocities. The distinct seismic characteristic of the continental lithosphere, i.e. the high velocities (Zhang and Tanimoto 1993; Su et al. 1994; Polet and Anderson 1995; Woodhouse and Trampert 1995), is mainly determined by the thermal state of the model. A low velocity zone at the root-mantle transition is observed in velocity profiles inferred from the model. Such a zone has been reported by LeFevre and Helmberger (1989). The compositional effect results in localized velocity variations. Other upper mantle seismic features have been discussed by Revenaugh and Jordan (1991c), Karato (1992) and Gaherty and J. (1995).

The total volume of depleted root increases through a intermittent process of diapiric melting (Chapters 4 to 7). If the produced melt can segregate to the crustal regions, it can contribute to the total continental crustal volume (Drummond and Collins 1986; Behrend et al. 1990; Nelson 1991). If this melt cannot reach the crustal level, it will be trapped in the continental root where it forms layers or regions with distinct composition. Under high pressure, i.e. in the continental root, this underplated basaltic melt probably solidifies in the form of high density eclogite.

It is illustrated here that variations in the degree of depletion of the lithospheric harzburgite may act as seismic P-wave reflectors. In reality, solidified melt might be trapped in the root when it is not capable of segregating to crustal levels. The reflection coefficient and the seismic velocities can be effected by this dense solidified melt. Deep upper mantle seismic reflections and seismic velocity variations have been observed underneath several Precambrium shields at depths from 50 to 200 km (Pavlenkova and Yegorkin 1983; Ellis et al. 1996; Pavlenkova et al. 1996). This depth range corresponds to the modelled continental root depths where impedance variations are observed.

Chapter 9

GENERATION OF KOMATIITE IN THE TRANSITION ZONE

9.1 Introduction

It is widely held that pressure release partial melting in the upper mantle starts at higher pressure in a hotter Earth. The pressure where fertile upper mantle peridotite starts to melt is between 2 and 10 *GPa* for a realistic solidus and potential temperatures between 1300 and 1750°C, respectively. Upper mantle dynamics, the composition of the extracted melt, the amount of melt, and the associated differentiated layer are directly influenced by the total pressure interval where the partial decompression melting occurs. The pressure range where partial melting occurs is therefore relevant for the Earth's upper mantle evolution.

Several authors have argued that the total thickness of the differentiated layer is important for oceanic upper mantle dynamics throughout the Earth's evolution. Vlaar and Van Den Berg (1991) demonstrated that in a hotter Earth this layer is gravitationally stable for much longer periods of time compared to the much thinner present-day equivalent. The deepest part of the thicker basaltic crust generated in a hot Earth will be in its eclogitic phase, which results in compositionally driven instabilities at relative shallow depths as shown by Vlaar et al. (1994). This might be an effective mechanism to transport heat from the mantle to the surface through this relatively thin and shallow layer. Hoffman and Ranalli (1988) argued that the rheological difference between thick and thin differentiated layers is significant. Hence, the rheology supposedly has a large effect on the Archaean style of upper mantle dynamics.

In Chapters 4, 5 and 7 it is demonstrated that the pressure range where partial melting occurs in the mantle throughout the Earth's evolution can also explain several well known features of old continental roots. Especially their depth extend, their long-term stability, and their degree of depletion are among these features.

The compositions of the generated melt and its residue are influenced by the pressure range where partial melting takes place (O'Hara et al. 1975; O'Hara 1985; McKenzie and Bickle 1988; Calin 1991). Komatiitic melt is formed when high degrees of depletion are established when melting starts at high pressures (~ 6 *GPa*) (Bickle et al. 1977; Takahashi 1990; Hirose and Kushiro 1993; Herzberg 1992; Nisbet et al. 1993; Herzberg et al. 1990). Still partly unsolved is the effect the dynamics of melt segregation has on the melt composition after melt extraction (McKenzie and Bickle 1988; Hirschmann et al. 1998).

The parameterization involved in most relatively simple isentropic 1-D models includes two parts that determine the pressure where the onset of melting takes place: the incorporated thermal expansion coefficient, and the positioning of the solidus in the $p - T$ -plane. The former determines the adiabat and is normally taken constant. For a known adiabat the latter determines its intersection with the solidus and is, up to pressures of about 10 *GPa*, relatively well established for dry peridotite. Reported uncertainties normally are in the order of ± 100 *K*.

The total amount of melt that can be generated in a 1-D isentropic upwelling depends on several other parts of the model description. Firstly, the positioning of the liquidus with respect to the solidus is important and in general their isobaric separation is decreasing with increasing pressure (Ohtani et al. 1986; Gasparik 1990; Herzberg and Zhang 1996). Secondly, a highly unknown parameter is the total entropy change upon melting (McKenzie 1984). In general this parameter is taken to be constant, but is known to be both pressure- and temperature-dependent, and it has a large effect on the latent heat consumption and therefore on the adiabat in the melt region (McKenzie and Bickle 1988). An extensive discussion of the basic thermodynamics of batch and fractional melting is given by Asimow et al. (1997). Lastly, the parameterization of the change in degree of depletion with increasing supersolidus temperature has a direct influence on the degree of depletion and thermal state of the differentiated layer. At relatively low pressures, experimentally found trends (Jacques and Green 1980; McKenzie and Bickle 1988) can be compared with theoretically determined relations (Kostopoulos 1991; Hirschmann et al. 1998). Effects of increasing pressure are not precisely known.

Although, the phase-diagram becomes more uncertain with increasing pressure, all experimentalists find a kink in the solidus around $p = 15$ *GPa*. This kink reflects the effect the solid-state phase-transition (from α -olivine to β -spinel) has on the equilibrium lines (Ohtani et al. 1986; Ohtani and Sawamoto 1987; Gasparik 1990). At increasing pressure the transition from β -spinel to γ -spinel takes place. Kinks in the solidus and liquidus are also found for this change in the state of olivine. Both phase-transitions are exothermal and an adiabatically upwelling mantle rock will consume latent heat that is extracted from its own volume and the temperature therefore decreases over the pressure ranges where the phase-transitions take place.

Here, the implications of the presence of these phase-transitions for the pressure ranges where partial melting takes place are discussed in the context of a simple 1-D model for isentropically upwelling rock.

9.2 Model description

The 1-D model has a constant thermal expansion coefficient α and a total constant entropy change upon melting ΔS as used before (Table 2.1). The parameterizations of the solid-state phase-transitions for olivine are described in Section 2.2.2 and parameter values are given in Table 2.2. The effect of a variable thermal expansion coefficient $\alpha(p, T)$ is minor compared to the exact melting parameterization. (Dietrich and Arndt 1982) and (Chopelaz and Boehler 1992) showed that α decreases with increasing p . An increasing temperature has the reverse effect (Ketcham et al. 1995; Bouhifd et al. 1996). Dynamical modelling of the mantle with variable thermodynamical properties has been done by Steinbach and Yuen (1994) and Dubuffet et al. (1999). The kinematic framework of the model used here is identical to the 1-D models as used before by (Vlaar and Van Den Berg 1991; Vlaar et al. 1994)

The phase-diagram consists of three different parts (Figure 2.1.c). Each part corresponds to a certain pressure interval with a different phase of olivine. The polynomial phase-diagram parameterization is based on data given by Herzberg and Zhang (1996). The first part is for the pressure range of 0 to 15.5 *GPa*, i.e. the α -olivine region. The second and third part are for the β - and γ -spinel regions and correspond to pressure ranges of 15.5 – 20.5 *GPa* and > 20.5 *GPa*, respectively. With $\vec{p} = (1, p, p^2, p^3)^T$ the solidus and liquidus are given by

$$T_s(p) = \vec{a}_s \cdot \vec{p} \quad (9.1)$$

$$T_l(p) = \vec{a}_l \cdot \vec{p} \quad (9.2)$$

where the different values of \vec{a}_s and \vec{a}_l are given in Table 9.1 The phase-diagram becomes more uncertain at larger pressures.

\vec{a}_s	$0 < p < 15.5$ [<i>GPa</i>]	$15.5 < p < 20.5$ [<i>GPa</i>]	$p > 20.5$ [<i>GPa</i>]
a_0	1125.43	-4755.413	-31281.69
a_1	166.020	994.428	4379.2337
a_2	-10.256	-47.6734	-190.88904
a_3	0.2189	0.76419	2.7750866

\vec{a}_l	$0 < p < 15.5$ [<i>GPa</i>]	$15.5 < p < 20.5$ [<i>GPa</i>]	$p > 20.5$ [<i>GPa</i>]
a_0	1709.5508	-940.29972	-36587.811
a_1	54.46215	408.49314	5219.0979
a_2	-1.8660616	-17.075809	-234.05408
a_3	0.008104124	0.22736821	3.5024492

Table 9.1: Coefficients of the solidus (\vec{a}_s) and liquidus (\vec{a}_l) parameterization.

9.3 Results

9.3.1 Upwelling from the deepest upper mantle

Figure 9.1 shows the result for increasing temperatures in the upper mantle. The temperature at the transition from upper to lower mantle at 670 *km* depth is the investigated variable in the model. The three coldest geotherms in Figure 9.1.a correspond to potential temperatures of 1320, 1480, and 1640 °C for which melting starts at pressures of 1.6, 3.0, and 5.5 *GPa*, respectively. Latent heat effects of the phase transitions are taken into account in determining the potential temperatures.

If the temperature at 670 *km* depth is increased further, the solidus is crossed, which implies that the material must be partially molten in this very deep region. If a partially molten rock is subject to adiabatical uplift it would typically follow geotherms corresponding to the two hot inflow temperatures of 2225 and 2235 °C. Since the thermal effect of the initial melting process is not incorporated at the inflow condition, we cannot compare the potential temperatures of these partially molten rocks with the three colder geotherms for the inflow of undifferentiated rock. The temperatures are referred to as apparent potential temperatures of 1645 and 1665 °C corresponding to the inflow temperatures of 2225 and 2235 °C, respectively.

A constraint of this phase-diagram is that the zone between 6 to 15 *GPa* cannot be a pressure range where partial melting takes place when the process of upwelling

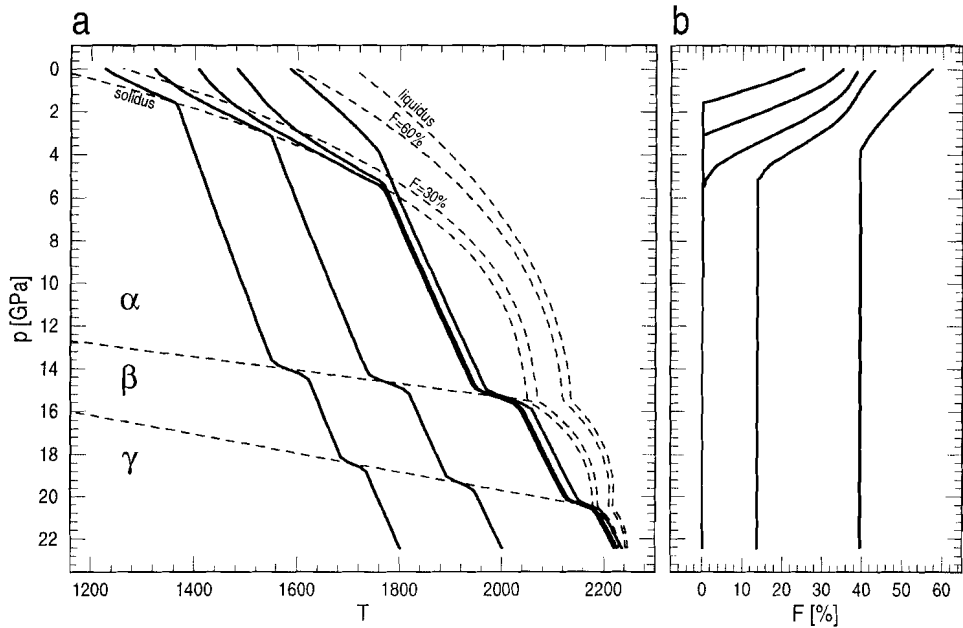


Figure 9.1: **a** Geotherms for different potential temperatures. From the coldest to the hottest geotherm the values for T_{pot} are: 1320, 1480, 1640, 1645, and 1665°C (see also text for further explanation). The dashed lines are solidus ($F = 0\%$) and liquidus ($F = 100\%$) with two in between phase-equilibrium lines as indicated. **b** Degree of depletion profiles corresponding to the geotherms of **a**. No crustal pressure correction is applied.

is isentropic and starts in the deep γ -spinel region of the upper mantle. For melting in this pressure interval a higher potential temperature is needed. For these higher temperatures the adiabat crosses the solidus in the deepest region of the upper mantle. This is the case for the two hottest temperature profiles. This is caused by the curvature of the phase-equilibrium lines in combination with the latent heat effects of the solid-state phase-transitions of olivine.

This phase-diagram puts a constraint on the maximum depth where relative shallow (< 12 GPa, i.e. the α -olivine region) melting can occur. If melting occurs at much deeper levels the ascending material is already partially molten. The uprising depleted material starts melting at the solidus corresponding to its degree of depletion. This is illustrated by the two hottest geotherms for which the onset of continued melting takes place at 5.1 and 3.8 for apparent potential temperatures of 1645 and 1665, respectively. This is also reflected in the corresponding depletion profiles in Figure 9.1.b.

This situation can change when the deepest part of the upper mantle is not adiabatic as discussed in the next section.

9.3.2 Melting in the upper mantle transition zone

If the temperature in the deepest part of the upper mantle is subsolidus and super-adiabatic, adiabatically upwelling material can probably cross the solidus in different pressure ranges. A super-adiabatic deep upper mantle can occur when vertical advection

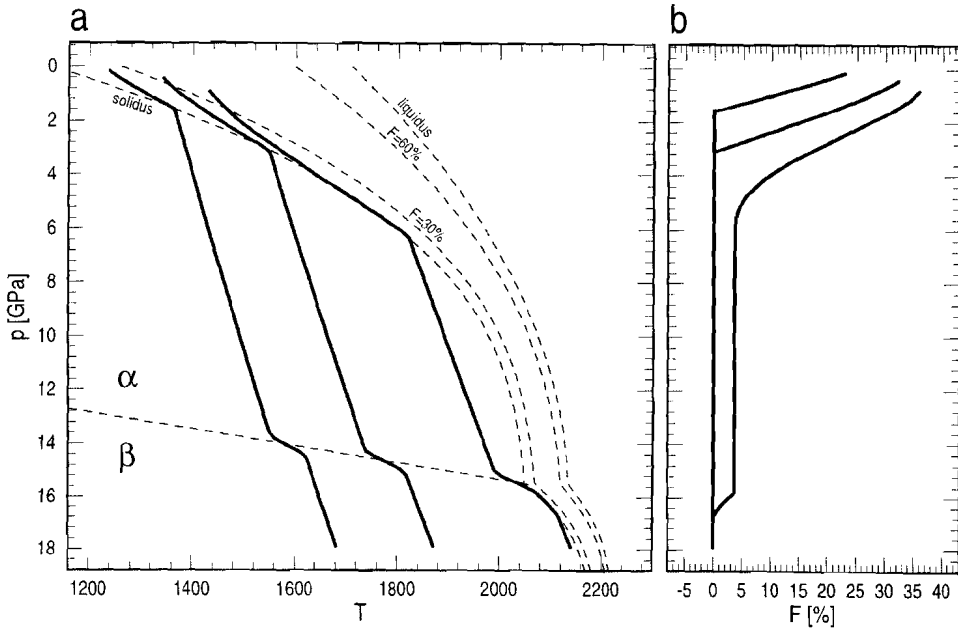


Figure 9.2: **a** Geotherms for different potential temperatures. From the coldest to the hottest geotherm the values for T_{pot} are: 1320, 1480, and 1700°C. The dashed lines are solidus ($F = 0\%$) and liquidus ($F = 100\%$) with two in between phase-equilibrium lines as indicated. **b** Degree of depletion profiles corresponding to the geotherms of **a**.

rates are very low for a long period of time. The jump in the geotherm corresponding to the transition from β - to γ -spinel might not be present since the heat is then transported conductively finally.

Melting of undepleted upwelling rock in the transition zone can also occur in model computations when the solidus at $p > 20.5 \text{ GPa}$ as used here, is chosen too low. Takahashi (1986) suggests a much higher solidus temperature at 22 GPa and that the slope of the β - γ Clausius-Clapeyron equilibrium line is steeper than assumed here and does therefore not reach the solidus.

Here, we assume that undepleted material starts its adiabatic ascend at a depth of 535 km (17.9 GPa) in the β -spinel region of the upper mantle. Figure 9.2.a and 9.2.b shows the geotherms and corresponding depletion profiles, respectively. The corresponding potential temperatures are 1320, 1480, and 1720°C. Here, the crustal pressure correction as described by (Vlaar and Van Den Berg 1991) is applied. The two coldest geotherms in Figure 9.2.a are the same as the two for same potential temperatures as shown in Figure 9.1.a.

The hottest geotherm in Figure 9.2.a is crossing the solidus very briefly in the deep β -spinel region. It therefore obtains a finite low degree of depletion of $F = 4\%$ (Figure 9.2.b) at about $p = 16 \text{ GPa}$. After subsequential uprise melting continues when the solidus is crossed again at deep levels in the α -olivine region.

Figure 9.3 shows the relative contribution to the crustal production as a function of pressure. The total crustal thickness is indicated at the left of each curve. The

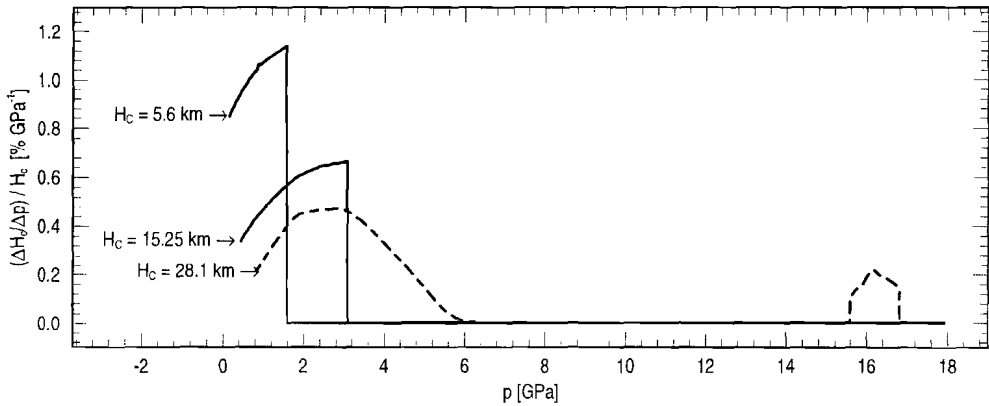


Figure 9.3: Relative crustal production as function of pressure. The curves correspond to the geotherm and F -profiles given in Figure 9.2.a and 9.2.b, respectively. Total crustal thickness H_C are indicated. Potential temperatures of 1320, 1480, and 1700°C correspond to crustal thicknesses of 5.6, 15.25, and 28.1 km, respectively.

crustal thicknesses of 5.6, 15.25, and 28.1 km correspond to the geotherms given in Figure 9.2.a with potential temperatures of 1320, 1480, and 1700°C, respectively.

The pulse in productivity around 16 GPa (dashed line) is caused by melting just underneath the β -spinel to α -olivine phase-transition. After subsequential uprise the melting slowly starts again around 6 GPa and reaches its maximum where the geotherm separates from the solidus around 3 GPa (see also Figure 9.2.a). The decreasing productivity at shallower depths in the three distinct upwellings is caused by the flattening of the $F(\theta)$ curve at higher values for θ as illustrated in Figure 5.2.b.

9.4 Conclusions

In spite of the uncertainties in the phase-diagram parameterization for the deeper part of the upper mantle, we can state that there exists a restriction on the maximum depth where melting occurs in the α -olivine region when isentropic upwelling is assumed. The curvature of the solidus and the thermal jumps due to latent heat effects associated with the solid-state phase-transitions of olivine make it impossible that partial decompression melting occurs in a pressure interval of about 6–13 *GPa* for the parameterization used.

If hot undepleted mantle rock can start its adiabatic ascend from depths where olivine is in the β -spinel phase, low degrees of partial melting ($\sim 2\%$) can be reached at a pressure of about 16 *GPa* and a potential temperature of 1700°C and if material did not cross the solidus at higher pressures. Komatiitic melts are probably generated when melting starts at high pressures. We suggest that in a hot Earth this deep melting process can start at pressures of $p = 16$ *GPa*. This places the origin of komatiitic lavas as found in Archaean shields at much higher pressures than assumed by most authors who suggest that melting starts at pressures of about 6 *GPa* (Bickle et al. 1977; Takahashi 1990; Hirose and Kushiro 1993; Herzberg 1992; Nisbet et al. 1993).

For an adiabatic geotherm we showed that partial melting in the deepest regions of the upper mantle can occur. This makes the concept of the presence of deep upper mantle magma oceans plausible during the very early stages of the Earth's evolution as suggested by (Abe 1997; Agee 1997). In addition to the adiabatic temperature increase, the latent heat effects of the solid-state phase-transition of olivine incorporated here are responsible for an extra isentropic increase of about 100 *K* over the upper mantle transition zone.

Chapter 10

COLOUR PLATES

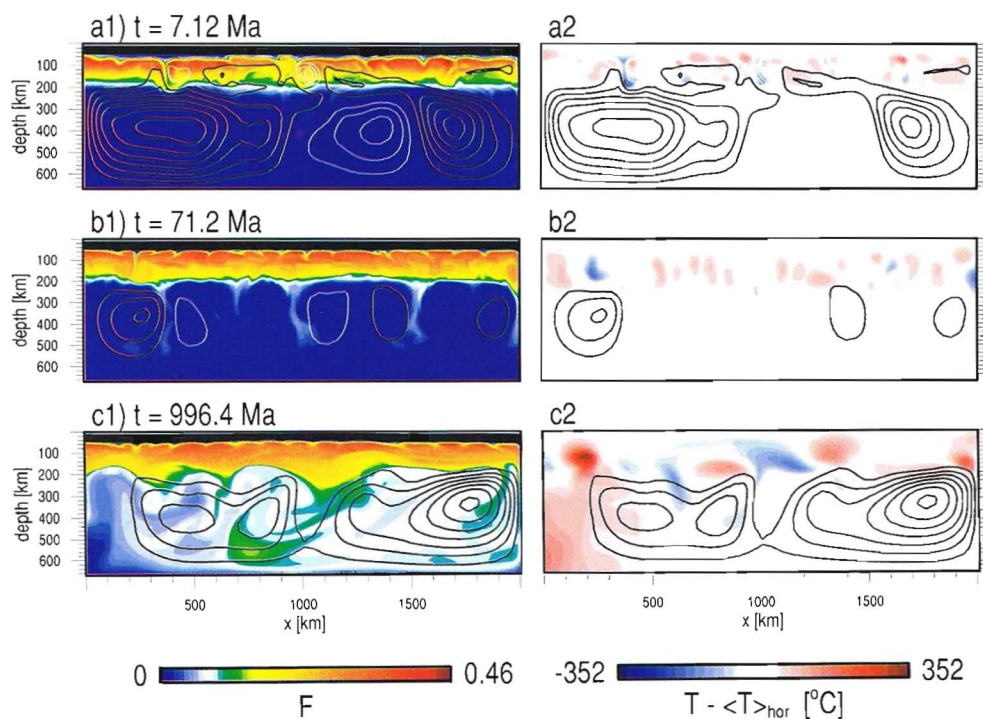


Figure 10.1: Contour-plots of F (a1-c1), $T - \langle T \rangle_{hor}$ (a2-c2) and streamlines during the spin-up phase (a), after 71.2 Ma evolution time (b), and after almost 1 Ga evolution (c). The black and white streamlines in all depictions indicate clockwise and counter-clockwise flows respectively. In a1-c1 the thin white layer on top is the upper crust and the lower crust is colored as a black layer underneath it. The harzburgite layer denoted dark grey is formed during a short period of time, and it continues to grow at a much slower rate. Cooling from the top penetrates through the continental root (a2-c2) creating a 200 km thick MBL.

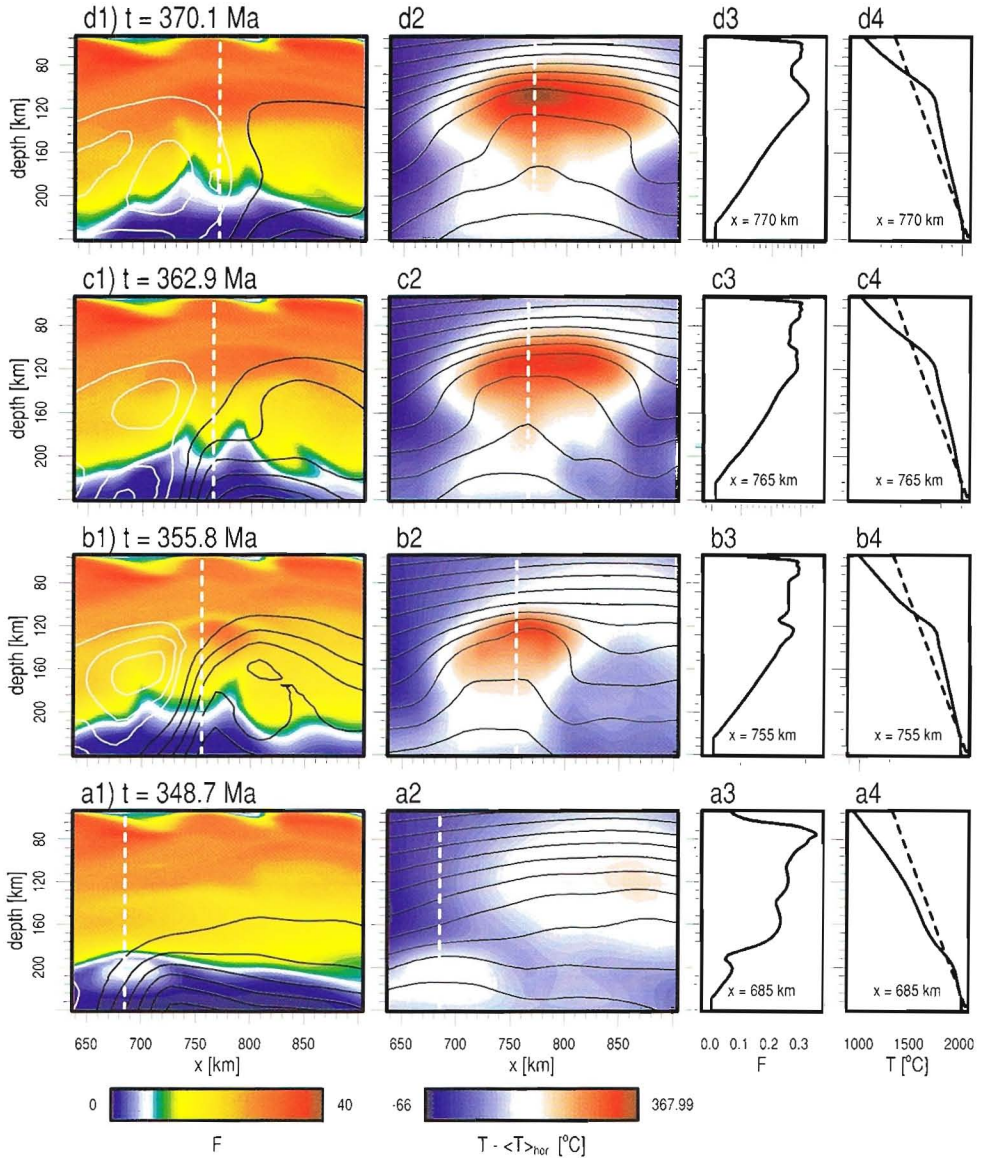


Figure 10.2: Evolution in time of the event indicated with black arrows in Figure 4.3 displayed in more detail. Streamlines in (a1-d1) are selected contours of the instantaneous stream function: black and white lines indicate clockwise and counter-clockwise flow respectively. The black isotherms in (a2-d2) have an increment of 110°C and put the colour contours of the modified temperature field into perspective. Figures (a3-d3) show vertical cross-sections of the degree of depletion through the center of the diapir at the x -coordinate shown in each figure. The cross-section locations are also shown as white vertical dashed lines in the contourplots. (a4-d4) Show cross-sections of the temperature at the same locations together with the solidus for undepleted material (dashed).

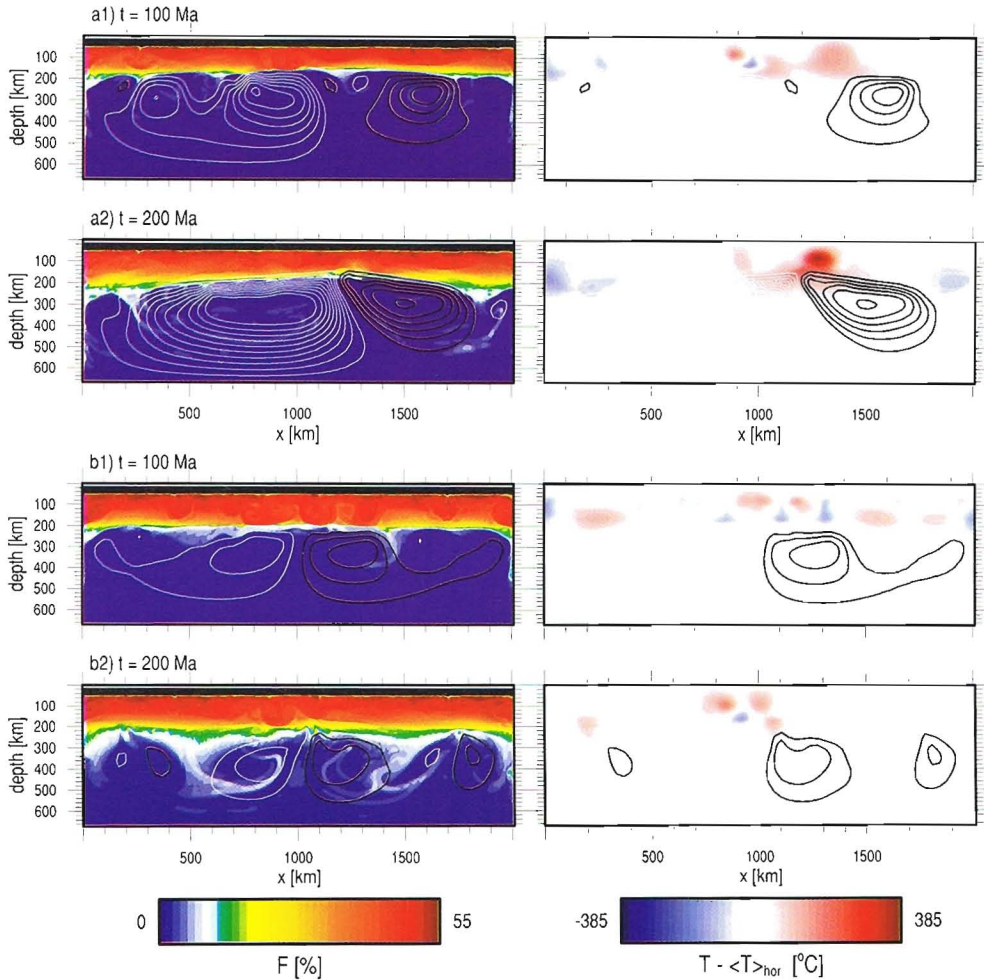


Figure 10.3: The depletion field and lateral variations of the temperature field (i.e. $\delta T = T - \langle T \rangle_{hor}$) at 100 Ma and 200 Ma for both parameterizations of the phase-diagram. Figures labeled a and b correspond to Model A and B respectively. Black and white contour lines indicate clockwise and counter clockwise flows, respectively. White F -field contouring corresponds to $9\% < F < 10\%$. The depletion for the polynomial case is larger than in the linear case due to the different F -dependency of θ (see the inset Figure 5.2.b). Also the thickness of the depleted layer is slightly thicker when the curved solidus/liquidus are used.

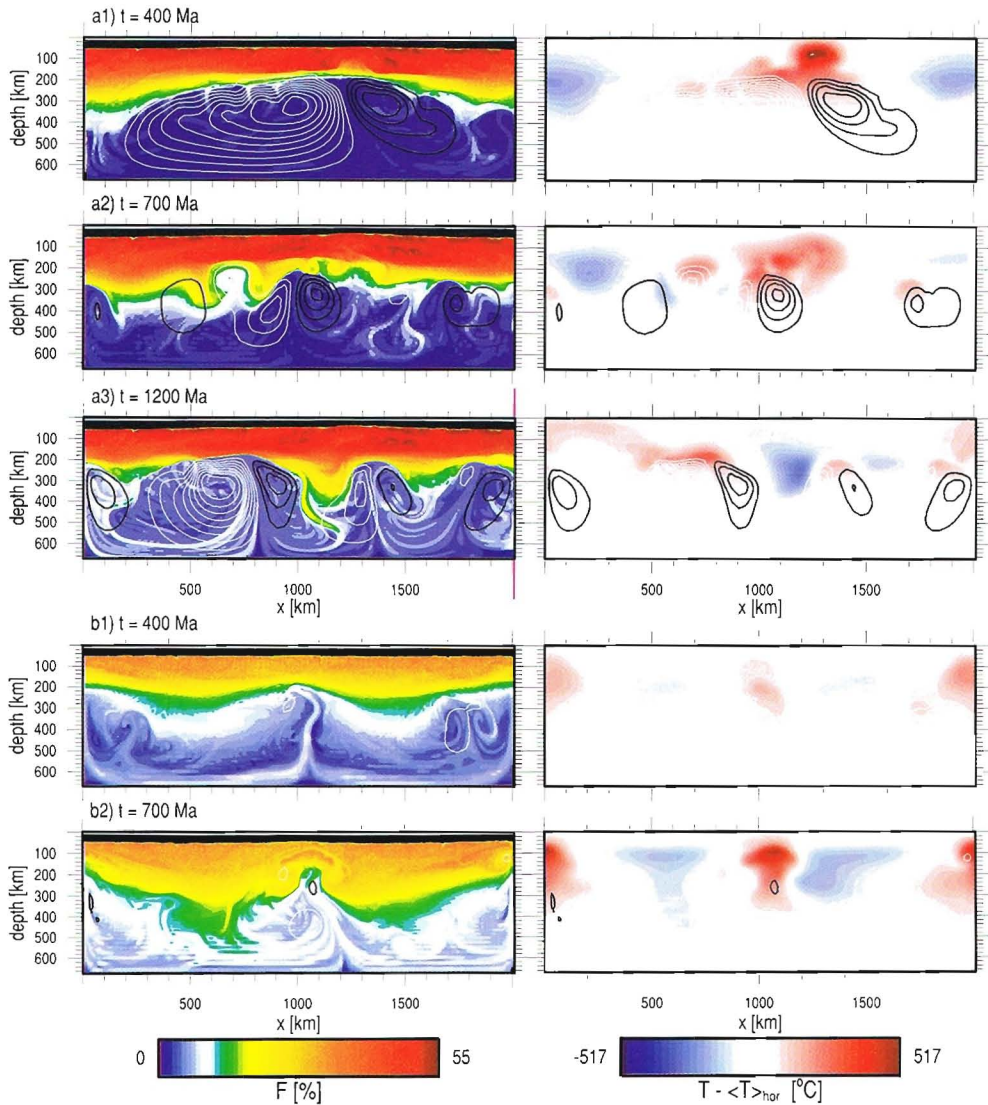


Figure 10.4: As in Figure 10.3 but now for $t = 400, 700$ Ma and for Model A also at 1200 Ma. Figures labeled a and b correspond to Model A and B respectively. Due to melting at large depths in Model B the lower half of the domain is also depleted. The wash-board effects visible in the degree of depletion of Figure 10.3.b.2 are numerical instabilities caused by the MoC-method applied over the too coarse grid in this lower part of the domain.

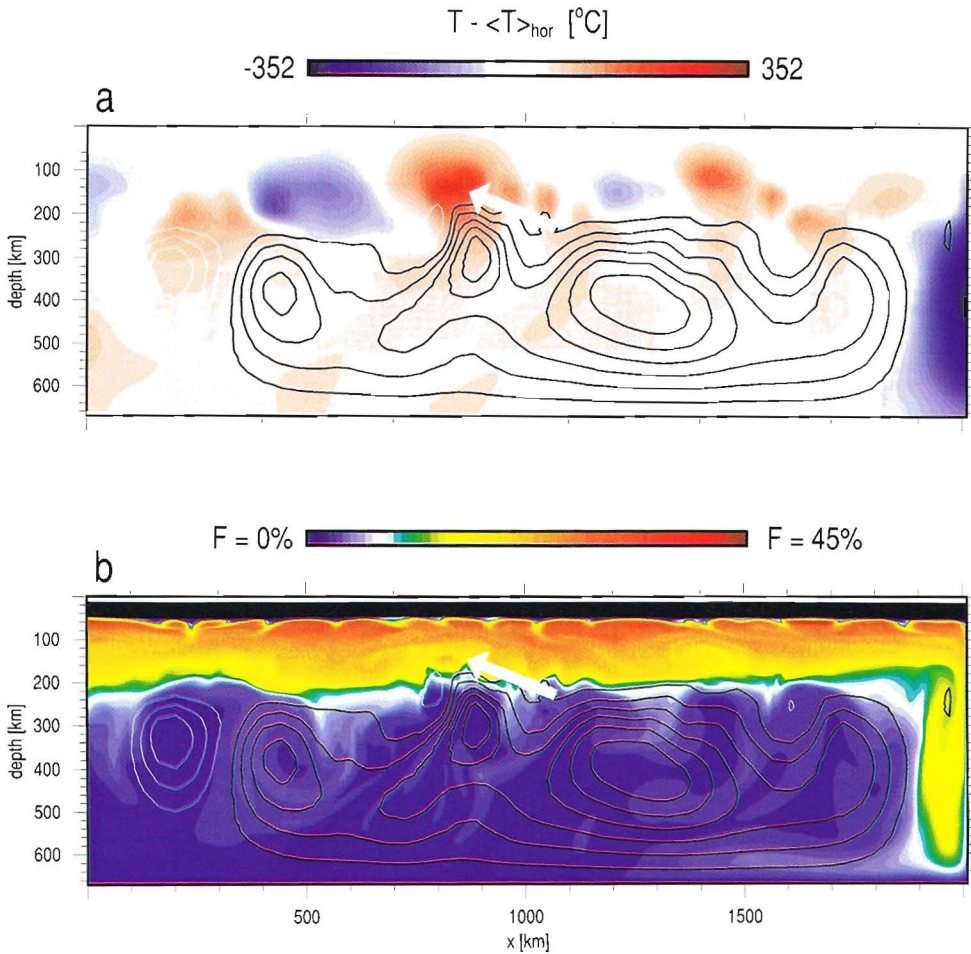


Figure 10.5: a) An overall snapshot of the lateral variations of the temperature field ($T - \langle T \rangle_{hor}$) at $t = 178 Ma$. The arrow points to the small-scale melting diapir which is the process through which the continental root grows. b) The corresponding degree of depletion field to Figure 10.5.a. White and black lines indicate counter-clockwise and clockwise flows, respectively. The thick black and thin white layers on top of the depleted zone in Figure 10.5.b are the lower and upper crust, respectively. A sketch of this situation has been given in Figure 6.1

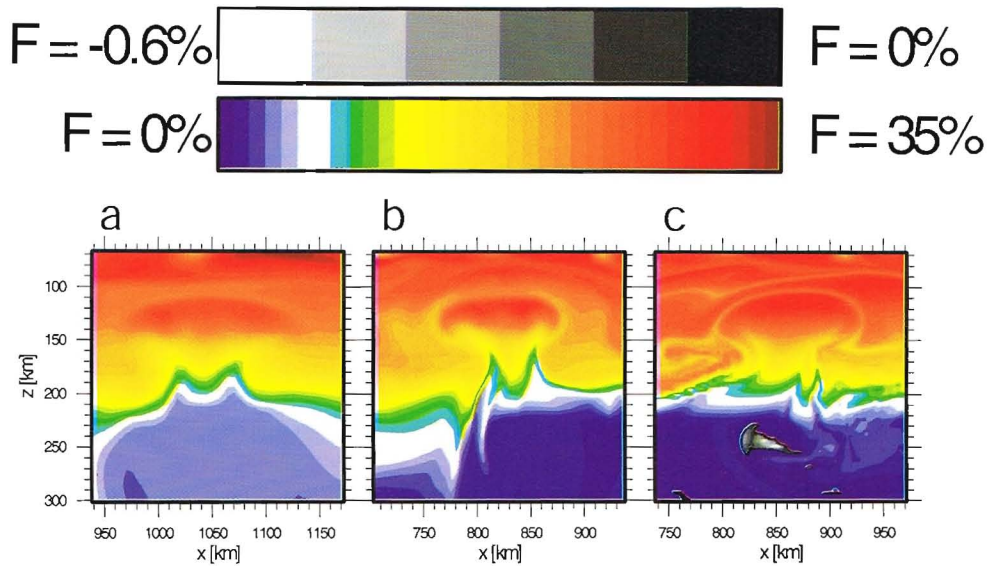


Figure 10.6: Blow-ups of melting diapirs that impinge the continental root and add depleted material to it. The events are for different mesh resolutions and interpolation schemes: a) ($t = 177.5 \text{ Ma}$) Low resolution and a hybrid scheme which is in favor of bilinear interpolations b) ($t = 180.8 \text{ Ma}$) High resolution and a hybrid scheme which is more in favor of the bicubic spline interpolations than the scheme used in Figure 10.6a). c) ($t = 217.8 \text{ Ma}$) High resolution and bicubic spline interpolations. In all frames the F -field has been plotted with less than the available resolution. The diapir highlighted in Figure 10.5.b corresponds to the one pointed at by the arrows in Figure 10.5.

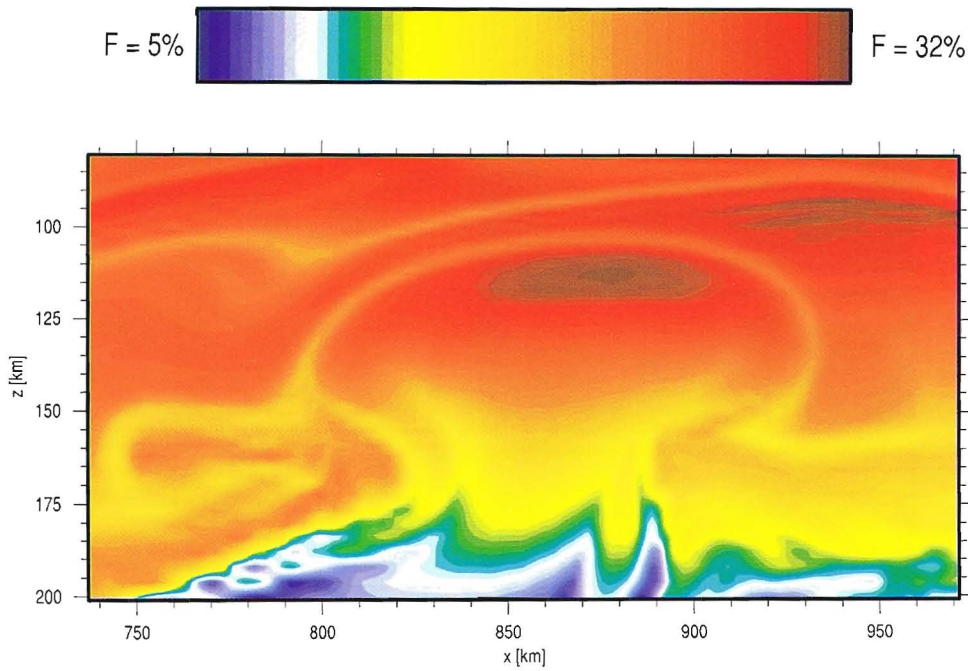


Figure 10.7: A further enlargement of the diapir as depicted in Figure 10.6 revealing the small-scale details on the very dense mesh 700×700 m on the average.

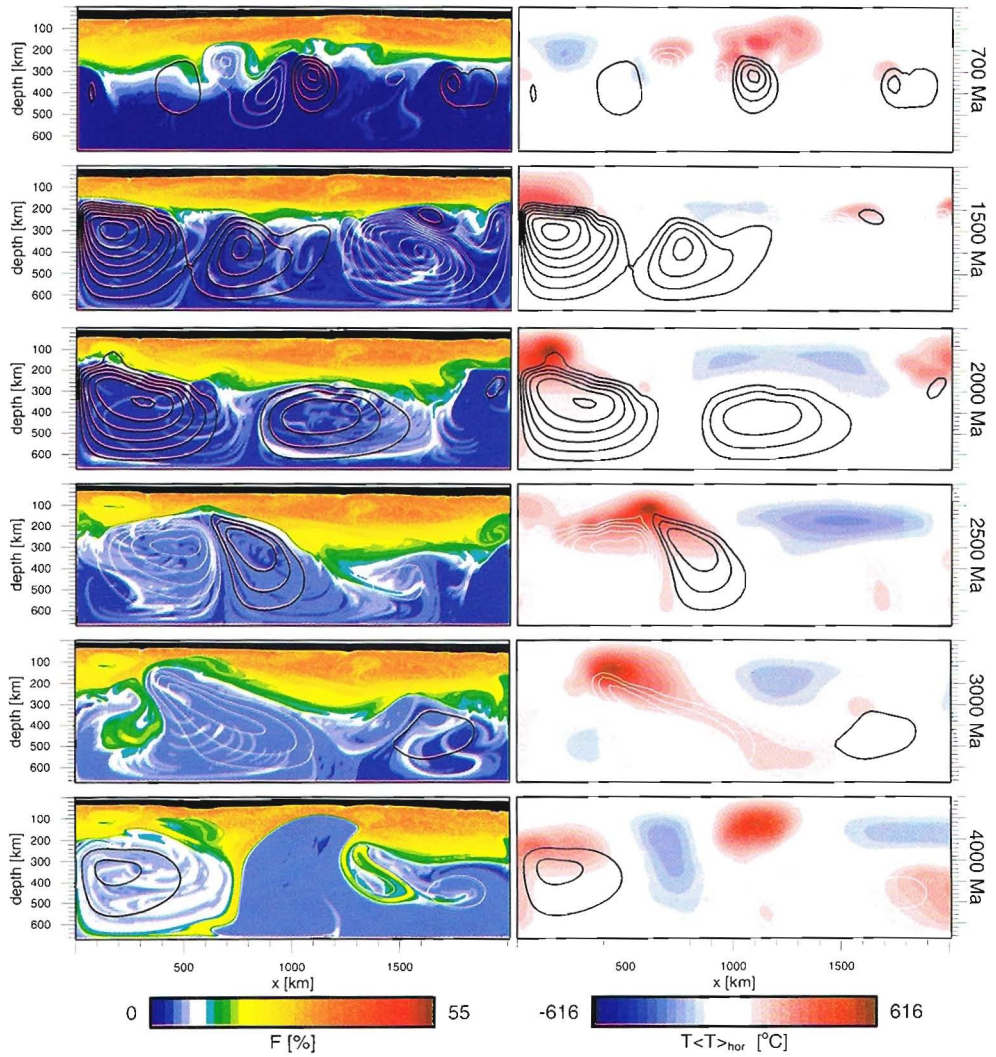


Figure 10.8: The left-hand-side column shows the F -field. Evolution times are given at each frame. The white and black layers at the top are the upper and lower crustal layers, respectively. White coloured F -field below the crust corresponds to $9\% < F < 10\%$. The corresponding lateral variations of the temperature field (i.e. $T - \langle T \rangle_{hor}$) are shown in the right-hand-side column. Black and white contour lines in all frames indicate clockwise and counter clockwise flows, respectively.

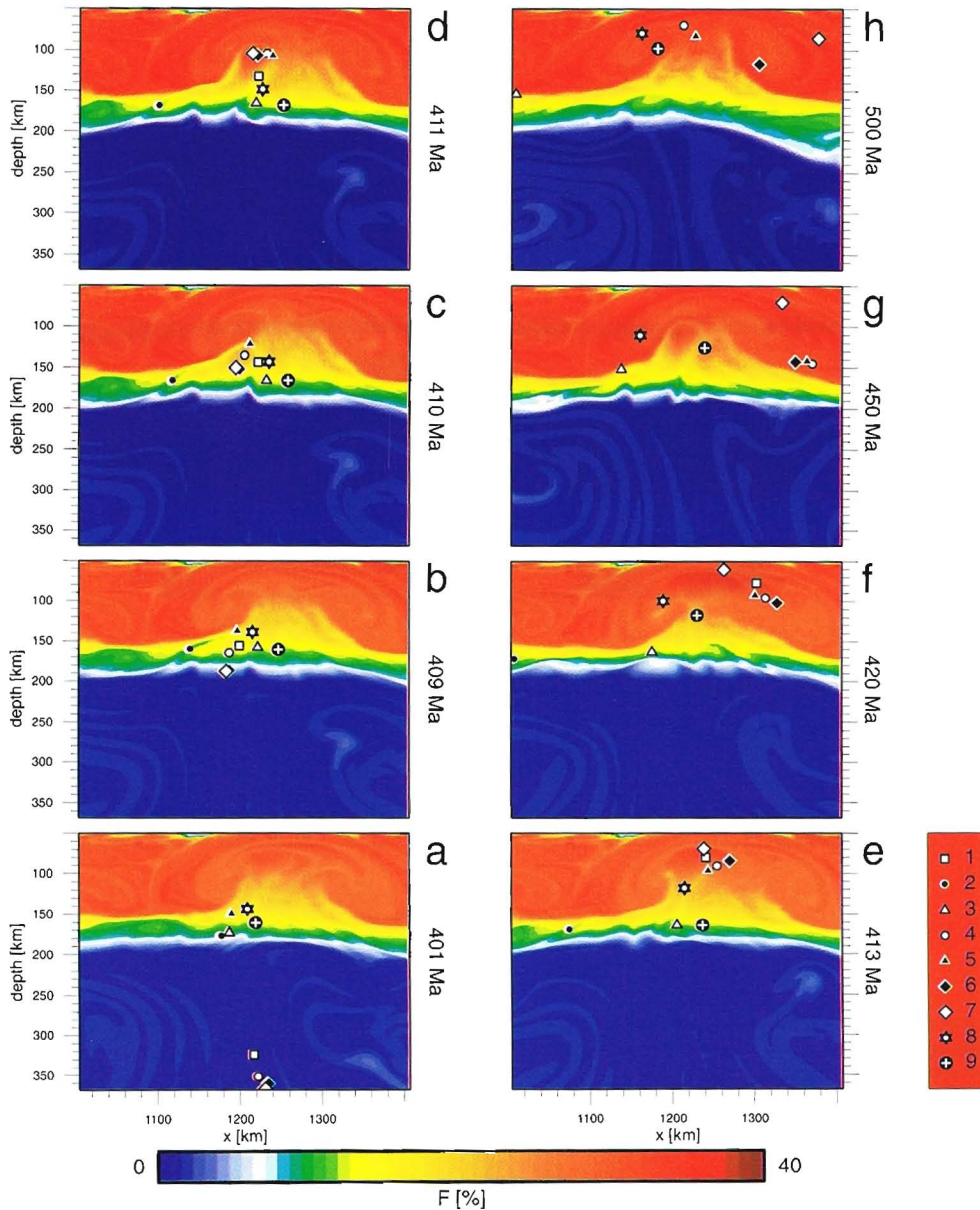


Figure 10.9: Several enlargements of F -field snapshots illustrating the evolution of the continental root where small-scale melting diapirs impinge the depleted layer between 401 and 500 Ma . The material that melts comes from the undepleted deeper region as is inferred from the flow pattern the nine tracers indicate. This melting event corresponds to the first long period of the model evolution during which episodically melting occurs and melting starts at relatively large depths (see also Figure 7.3). Not the full available grid resolution was used in these contour plots.

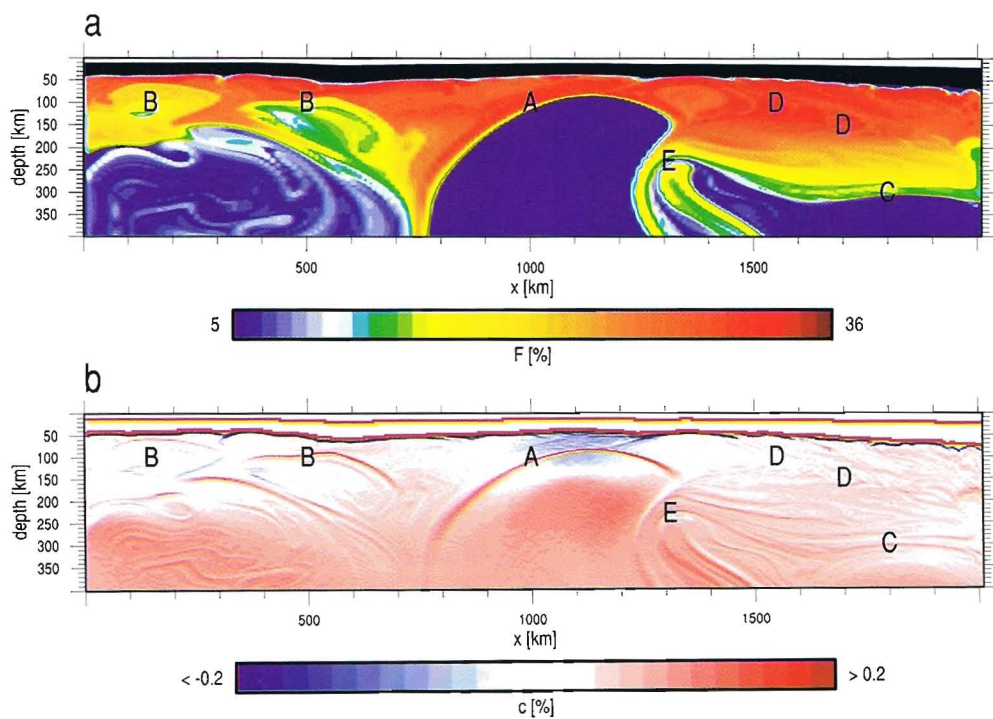


Figure 10.10: **a** Compositional field of the upper 400 km of the model. Note that the contour scale different from the scale used in Figure 10.9. **b** Seismic reflection coefficient field at $t = 4 \text{ Ga}$ for a horizontal layer thickness of 3.37 km.

BIBLIOGRAPHY

- Abbott, D. (1991). The case for accretion of the tectosphere by buoyant subduction. *Geophys. Res. Lett.* 18, 585–588.
- Abe, Y. (1997). Thermal and chemical evolution of the terrestrial magma ocean. *Physics of the Earth and Planetary Interiors* 100, 27–39.
- Agee, C. B. (1993). Petrology of the mantle transition zone. *Ann. Rev. Earth Planet. Sci.* 21, 19–41.
- Agee, C. B. (1997). Melting temperatures of the Allende meteorite: Implications for a Hadean magma ocean. *Physics of the Earth and Planetary Interiors* 100, 41–47.
- Anderson, D. L. (1990). *Continental mantle* (Ed. Menzies, M.), Chapter: Geophysics of the continental mantle: a historical perspective, pp. 1–30. Oxford, United Kingdom, Clarendon Press.
- Asimow, P. D., M. M. Hirschmann, and E. M. Stolper (1997). An analysis of variations in isentropic melt productivity. *Phil. Trans. R. Soc. Lond.* 355, 255–281.
- Behrend, J. C., D. R. Hutchinson, M. Lee, C. R. Thornber, A. Tréhu, W. Cannon, and A. Green (1990). GLIMPCE seismic reflection evidence of deep-crustal and upper-mantle intrusions and magmatic underplating associated with the midcontinent rift system of North America. *Tectonophysics* 173, 595–615.
- Bernstein, S., P. B. Kelemen, and C. K. Brooks (1998). Depleted spinel harzburgite xenoliths in tertiary dykes from East Greenland: Restites from high degree melting. *Earth Plan. Sci. Lett.* 154, 221–235.
- Best, J. A. (1991). Mantle reflections beneath the Montana great plains on consortium for continental reflection profiling seismic reflection data. *J. Geophys. Res.* 96, 4279–4288.
- Bickle, M. (1993). Plume origin for komatiites. *Nature* 365, 390–391.
- Bickle, M. J., C. E. Ford, and E. G. Nisbet (1977). The petrogenesis of peridotite komatiites: evidence from high-pressure melting experiments. *Earth Plan. Sci. Lett.* 37, 97–106.
- Bina, C. R. (1998). A note on latent heat release from disequilibrium phase transformations and deep seismogenesis. *Earth Planets Space Accepted*.
- Blatt, H. and R. J. Tracy (1996). *Petrology: igneous, sedimentary, and metamorphic*. New York, USA: Freeman (2nd edition).
- Bouhfid, M. A., D. Andrault, G. Fiquet, and P. Richet (1996). Thermal expansion of forsterite up to the melting point. *Geophys. Res. Lett.* 23, 1143–1146.
- Boyd, F. R. (1987). *Mantle Xenoliths* (Ed. Nixon, P. H.), Chapter: High- and low-temperature garnet peridotite xenoliths and their possible relation to the lithosphere-asthenosphere boundary beneath southern Africa, pp. 403–412. John Wiley & Sons.
- Boyd, F. R. (1989). Compositional distinction between oceanic and cratonic lithosphere. *Earth Plan. Sci. Lett.* 96, 15–26.
- Boyd, F. R. and J. J. Gurney (1986). Diamonds and the African lithosphere. *Science* 232, 472–477.
- Boyd, F. R., J. J. Gurney, and S. H. Richardson (1985). Evidence for a 150–200-km thick Archaean lithosphere from diamond inclusion thermobarometry. *Nature* 315, 387–389.
- Buick, R. (1984). Carbonaceous filaments from North Pole, Western Australia: are they fossil bacteria in Archean stromatolites? *Precambrian Research* 24, 157–172.
- Calfin, J. D. (1988). A quantitative analysis of the dissipation inherent in the semi-lagrangian advection. *Mon. Wea. Rev.* 116, 8330–8336.
- Calin, D. (1991). Experimental evidence for the exsolution of cratonic peridotite from high-temperature harzburgite. *Earth Plan. Sci. Lett.* 106, 64–72.
- Campbell, I. H., R. W. Griffiths, and R. I. Hill (1989). Melting in an Archaean mantle plume; heads it's basalts, tails it's komatiites. *Nature* 339, 697–699.
- Canuto, C., M. Y. Hussaini, A. Quarteroni, and T. A. Zang (1988). *Spectral Methods in Fluid Dynamics*. Springer Series in Computational Physics. New York, U.S.A.: Springer-Verlag.

- Carswell, D. A., W. L. Griffin, and P. Kresten (1984). *Kimberlites, II: The mantle and crust-mantle relationships*, Volume 11B of *Developments in petrology* (Ed. Kornprobst, J.), Chapter: Peridotite nodules from the Ngopetsoeu and Lipelaneng kimberlites, Lesotho: a crustal or mantle origin, pp. 229–243. Elsevier Science Publishers, The Netherlands.
- Chapman, D. S. (1986). *The Nature of the Lower Continental Crust* (Eds. Dawson, J. B., Carswell, D. A., Hall, J. & Wedepohl, K. H.), Volume 24, Chapter: Thermal gradients in the continental crust, pp. 63–70. Spec. Publ. Geol. Soc. London.
- Chopelaz, A. and R. Boehler (1992). Thermal expansivity in the lower mantle. *Geophys. Res. Lett.* 19, 1983–1986.
- Christensen, U. R. (1992). An Eulerian technique for thermomechanical modelling of lithospheric extension. *J. Geophys. Res.* 97, 2015–2036.
- Christensen, U. R. and Y. D. A. (1985). Layered convection induced by phase transitions. *J. Geophys. Res.* 300, 10,291–10,300.
- Condie, K. C. (1984). Archaean geotherms and supra crustal assemblages. *Tectonophysics* 105, 29–41.
- Curtis, A., B. Dost, J. Trampert, and R. Snieder (1998). Eurasian fundamental mode surface wave phase velocities and their relationship with tectonic features. *J. Geophys. Res.* 103, 26,919–26,947.
- Cuvelier, C., A. Segal, and A. A. Van Steenhoven (1988). *Finite element methods and Navier–Stokes equations*. Mathematics and its applications. Dordrecht, The Netherlands: D. Reidel Publishing Company (Kluwer academic publishers group).
- Dietrich, P. and J. Arndt (1982). *High-Pressure Research in Geosciences* (Ed. Schreyer, W.), Chapter: Effects of Pressure and Temperature on the Physical Behavior of Mantle-Relevant Olivine, Orthopyroxene and Garnet: I. Compressibility, Thermal Properties and Macroscopic Grüneisen Parameters, pp. 293–306. E.Schweizerbart'sche Verlagsbuchhandlung, Stuttgart.
- DiMarco, M. J. and D. R. Lowe (1989). Stratigraphy and sedimentology of an early Archean felsic volcanic sequence, Eastern Pilbara block, Western Australia, with special reference to the Duffer formation and implications for crustal evolution. *Precambrian Research* 44, 147–169.
- Doin, M.-P., L. Fleitout, and U. Christensen (1997). Mantle convection and stability of depleted and undepleted continental lithosphere. *J. Geophys. Res.* 102, 2771–2787.
- Doin, M.-P., L. Fleitout, and D. McKenzie (1996). Geoid anomalies and structure of continental and oceanic lithospheres. *J. Geophys. Res.* 101, 16,119–135.
- Drummond, B. J. and C. D. N. Collins (1986). Seismic evidence for underplating of the lower continental crust of Australia. *Earth Plan. Sci. Lett.* 79, 361–372.
- Dubuffet, F., D. A. Yuen, and Rabinowicz (1999). Effects of a realistic mantle thermal conductivity on the patterns of 3-D convection. *Earth Plan. Sci. Lett.* Submitted.
- Dupeyrat, L., C. Sotin, and E. M. Parmentier (1995). Thermal and chemical convection in planetary mantles. *J. Geophys. Res.* 100, 497–520.
- Durrheim, R. J. and W. D. Mooney (1994). Evolution of the Precambrium lithosphere: Seismological and geochemical constraints. *J. Geophys. Res.* 99, 15,359–15,374.
- Ebinger, C. J. and N. H. Sleep (1998). Cenozoic magmatism throughout east Africa resulting from impact of a single plume. *Nature* 395, 788–791.
- Ellis, R. M., Z. Hajnal, and M. G. Bostock (1996). Seismic studies on the trans-Hudson orogen of Western Canada (in 'Kimberlites and structure of cratonic lithosphere'). *Tectonophysics* 262, 35–50.
- Farnetani, C. G. and M. A. Richards (1994). Numerical investigations of the mantle plume initiation model for flood basalt events. *J. Geophys. Res.* 99, 13,813–33.
- Finnerty, A. A. and F. R. Boyd (1987). *Mantle Xenoliths* (Ed. Nixon, P. H.), Chapter: Thermobarometry for garnet peridotites: basis for the determination of thermal and compositional structure of the upper mantle, pp. 381–402. John Wiley & Sons.
- Flack, C. and M. Warner (1990). Three-dimensional mapping of seismic reflections from crust and upper mantle, northwest of Scotland. *Tectonophysics* 173, 469–481.
- Gaherty, J. B. and J. H. J. (1995). Lehman discontinuity as the base of an anisotropic layer beneath continents. *Science* 268, 1468–1471.
- Gasparik, T. (1990). Phase relations in the transition zone. *J. Geophys. Res.* 95(B10), 15,751–15,769.
- Goes, S., R. Govers, and P. Vacher (1999). Shallow mantle temperatures under Europe from P and S wave tomography. Submitted to *J.G.R.*
- Griffin, W. L., F. V. Kaminsky, S. Y. Ryan, C. G. O'Reilly, T. T. Win, and I. P. Ilupin (1996). Thermal state and composition of the lithospheric mantle beneath the Daldyn kimberlite field, Yakutia (in 'Kimberlites and structure of cratonic lithosphere'). *Tectonophysics* 262, 19–33.
- Griffin, W. L., S. Y. Wass, and J. D. Hollis (1984). Ultramafic xenoliths from Bullenmeri and Gnotuk Maars, Victoria, Australia: Petrology of a subcontinental crust-mantle transition. *Journal of Petrology* 25, 53–87.

- Gurnis, M. (1988). Large-scale mantle convection and the aggregation and dispersal of supercontinents. *Nature* 332, 695-699.
- Hansen, U. and D. A. Yuen (1989). Dynamical influences from thermal-chemical instabilities at the core-mantle boundary. *Geophys. Res. Lett.* 16, 629-632.
- Herzberg, C. (1992). Depth and degree of melting of komatiites. *J. Geophys. Res.* 97, 4521-4540.
- Herzberg, C., T. Gasparik, and H. Sawamoto (1990). Origin of mantle peridotite: Constraints from melting experiments to 16.5 GPa. *J. Geophys. Res.* 95(B10), 15,779-15,803.
- Herzberg, C. and J. Zhang (1996). Melting experiments on anhydrous peridotite KLB-1: Compositions of magmas in the upper mantle and the transition zone. *J. Geophys. Res.* 101, 8271-8295.
- Hirose, K. and I. Kushiro (1993). Partial melting of dry peridotites at high pressure: Determination of compositions of melts segregated from peridotite using aggregates of diamonds. *Earth Plan. Sci. Lett.* 114, 477-489.
- Hirschmann, M. M., M. S. Ghiorso, L. E. Waslylenki, P. D. Asimow, and E. M. Stolper (1998). Calculation of peridotite partial melting from thermodynamic models of minerals and melts. I: Review of methods and comparison with experiments. *Journal of Petrology* 39, 1091-1115.
- Hirth, G. and D. L. Kohlstedt (1996). Water in the oceanic upper mantle: Implications for rheology, melt extraction and the evolution of the lithosphere. *Earth Plan. Sci. Lett.* 144, 93-108.
- Hockney, R. W. and J. W. Eastwood (1988). *Computer simulation using particles*. London, England: Institute of Physics Publishing, Bristol and Philadelphia.
- Hoffman, P. F. and G. Ranalli (1988). Archean oceanic flake tectonics. *Geophys. Res. Lett.* 15, 1077-1080.
- Honda, S. and D. A. Yuen (1990). Mantle convection with moving heat-source anomalies: geophysical and geochemical implications. *Earth Plan. Sci. Lett.* 96, 349-366.
- Hughes, T. J. R. and A. Brooks (1979). *Finite Element Methods for Convection Dominated Flows* (Ed. Hughes, T. J. R.), Volume 34 of *Applied Mechanics Division*, Chapter: A multidimensional upwind scheme with no crosswind diffusion. American Society of Mechanical Engineers, New York.
- Hunter, D. R. and C. W. Stowe (1997). *Greenstone Belts* (Eds. De Wit, M. J. & Ashwal, L. D.), Chapter: A historical review of the origin, composition, and setting of Archaean Greenstone Belts (Pre-1980), pp. 5-29. Oxford University Press.
- Ita, J. and S. D. King (1994). Sensitivity of convection with endothermic phase change to the form of governing equations, boundary conditions and equation of state. *J. Geophys. Res.* 99, 15,919-938.
- Jackson, M. J. and H. N. Pollack (1984). On the sensitivity of parameterized convection to the rate of decay of internal heat sources. *J. Geophys. Res.* 89, 10,103-10,108.
- Jacques, A. L. and D. H. Green (1980). Anhydrous melting of peridotite at 0-15 kb pressure and genesis of tholeiitic basalts. *Contrib. Mineral. Petrol.* 73, 287-310.
- Jordan, T. H. (1975). The continental tectosphere. *Reviews of Geophysics and Space Physics* 13(3), 1-12.
- Jordan, T. H. (1978). Composition and development of the continental tectosphere. *Nature* 274, 544-548.
- Jordan, T. H. (1979). *The Mantle Sample: Inclusions in Kimberlites and Other Volcanics* (Eds. Boyd, F. R. & Meyer, H. O. A.), Chapter: Mineralogies, densities, and seismic velocities of garnet lherzolites and their geophysical implications, pp. 1-14. American Geophysical Union, Washington D.C.
- Jordan, T. H. (1988). *Journal of Petrology: 'Oceanic and Continental Lithosphere: Similarities and Differences'* (Eds. Menzies, M. A. & Cox, K. G.), Special volume 1988, Chapter: Structure and formation of the continental tectosphere, pp. 11-37.
- Kameyama, M., H. Fujimoto, and M. Ogawa (1996). A thermo-chemical regime in the upper mantle in the early earth inferred from a numerical model of magam-migration in a convecting upper mantle. *Physics of the Earth and Planetary Interiors* 94, 187-215.
- Karato, S. (1990). The role of hydrogen in the electrical conductivity of the upper mantle. *Nature* 347, 272-273.
- Karato, S. (1992). On the Lehman discontinuity. *Geophys. Res. Lett.* 19, 2255-2258.
- Karato, S. (1993). Importance of anelasticity in the interpretation of seismic tomography. *Geophys. Res. Lett.* 20, 1623-1626.
- Karato, S. and H. Jung (1998). Water, partial melting and the origin of the seismic low velocity and high attenuation zone in the upper mantle. *Earth Plan. Sci. Lett.* 157, 193-207.
- Karato, S., M. S. Paterson, and J. D. Fitz Gerald (1986). Rheology of synthetic olivine aggregates: influence of grain size and water. *J. Geophys. Res.* 91, 8151-8176.
- Karato, S. and P. Wu (1993). Rheology of the upper mantle: A synthesis. *Science* 260, 771-778.
- Kellogg, L. H. and S. D. King (1993). Effect of mantle plumes on the growth of D" by reaction between the core and mantle. *Geophys. Res. Lett.* 20, 379-382.
-

- Ketcham, R. A., E. C. Beam, and M. A. Kominz (1995). Effects of temperature-dependent material properties and radioactive heat production on simple basin subsidence models. *Earth Plan. Sci. Let.* 130, 31-44.
- Kostopoulos, D. K. (1991). Melting of the shallow upper mantle: A new perspective. *Journal of Petrology* 32, 671-699.
- Kusky, T. M. (1993). Collapse of Archean orogens and the generation of late postkinematic granitoids. *Geology* 21, 925-928.
- Lambeck, K., P. Johnston, C. Smither, and M. Nakada (1996). Glacial rebound of the British Isles - III: Constraints on mantle viscosity. *Geophys. J. Int.* 125, 340-354.
- LeFevre, L. V. and D. V. Helmberger (1989). Upper mantle *P* velocity structure of the Canadian shield. *J. Geophys. Res.* 94, 17,749-17,765.
- Leitch, A. M., G. F. Davies, and M. Wells (1998). A plumehead melting under a rifting margin. *Earth Plan. Sci. Let.* 161, 161-177.
- Lenardic, A. (1997). On the heat flow variation from Archean cratons to Proterozoic mobile belts. *J. Geophys. Res.* 102, 709-721.
- Lenardic, A. and W. M. Kaula (1993). A numerical treatment of geodynamic viscous flow problems involving the advection of material interfaces. *J. Geophys. Res.* 98, 8243-8260.
- Malevsky, A. V. and D. A. Yuen (1991). Characteristics-based methods applied to infinite Prandtl number thermal convection in the hard turbulent regime. *Phys. Fluids A* 3(9), 2105-2115.
- Matyska, C. (1994). *Gravimetry and Space Techniques Applied to Geodynamics and Ocean Dynamics*, Volume 17 of *Geophysical Monograph Series*, Chapter: Topographic Masses and Mass Heterogeneities in the Upper Mantle, pp. 125-132. American Geophysical Union, Washington D.C.
- McKenzie, D. (1984). The generation and compaction of partially molten rock. *J. Geophys.* 25, 713-765.
- McKenzie, D. and M. Bickle (1988). The volume and composition of melt generated by extension of the lithosphere. *J. Geophys. Res.* 29, 625-679.
- Mezger, K., E. J. Essene, and A. N. Halliday (1992). Closure temperatures of the Sm-Nd system in metamorphic garnets. *Earth Plan. Sci. Let.* 113, 397-409.
- Mooney, W. D., G. Laske, and T. G. Masters (1998). Crust 5.1: A global crustal model at 5° × 5°. *J. Geophys. Res.* 103, 727-747.
- Moresi, L. and V. Solomatov (1997). Mantle convection with a brittle lithosphere: Thoughts on the global tectonic styles of the Earth and Venus. *Geophys. J. Int.* (Submitted).
- Müller, R. D., W. R. Roest, J. Y. Royer, L. M. Gahagan, and J. G. Sclater (1996). Age of the ocean floor. Technical Report MGG-12, World Data Center A for Marine Geology and Geophysics, 325 Broadway, Boulder, CO 80303-3328, U.S.A.
- Muyzert, E. (1996). A seismic cross section through the East European continent. *Geophys. J. Int.* (Submitted).
- Nelson, K. D. (1991). A unified view of craton evolution motivated by recent deep seismic reflection and refraction results. *Geophys. J. Int.* 105, 25-35.
- Nisbet, E. G., M. J. Cheadle, N. T. Arndt, and M. J. Bickle (1993). Constraining the potential temperature of the Archaean mantle: A review of the evidence from komatiites. *Lithos* 30, 291-307.
- Niu, Y. (1997). Mantle melting and melt extraction processes beneath ocean ridges: evidence from abyssal peridotites. *Journal of Petrology* 38, 1047-1074.
- Niu, Y. and R. Batiza (1991). In situ densities of MORB melts and residual mantle: Implications for buoyancy forces beneath mid-ocean ridges. *Journal of Petrology* 99, 767-775.
- Nyblade, A. A. and H. N. Pollack (1993). A global analysis of heat flow from Precambrian terrains: Implications for the thermal structure of Archean and Proterozoic lithosphere. *J. Geophys. Res.* 98, 12,207-12,218.
- O'Connell, R. J. and B. H. Hager (1980). *Physics of the Earth's Interior* (Eds. Dziewonski, A. M. & Boschi, E.), Chapter: On the Thermal State of the Earth, pp. 270-317. Elsevier, New York.
- Ogawa, M. (1988). Numerical experiments on coupled magmatism-mantle convection system: Implications for mantle evolution and Archean continental crusts. *J. Geophys. Res.* 93, 15119-15134.
- Ogawa, M. (1993). A numerical model of a coupled magmatism-mantle convection system in Venus and the Earth's mantle beneath Archean continental crusts. *Icarus* 102, 40-61.
- Ogawa, M. (1994). Effects of chemical fractionation of heat-producing elements on mantle evolution inferred from a numerical model of coupled magmatism-mantle convection system. *Physics of the Earth and Planetary Interiors* 83, 101-127.
- Ogawa, M. and H. Nakamura (1998). Thermochemical regime of the early mantle inferred from numerical models of the coupled magmatism-mantle convection system with the solid-solid phase transitions at depths around 660 km. *J. Geophys. Res.* 103(B6), 12,161-12,181.

- O'Hara, M. J. (1985). Importance of the 'shape' of the melting regime during partial melting of the mantle. *Nature* 314, 58–62.
- O'Hara, M. J., M. J. Saunders, and E. L. P. Mercy (1975). Garnet-peridotite, primary ultrabasic magma and eclogite; interpretation of upper mantle processes in kimberlite. *Phys. Chem. Earth* 9, 571–604.
- Ohtani, E., T. Kato, and H. Sawamoto (1986). Melting of a model chondritic mantle to 20 GPa. *Nature* 322, 352–353.
- Ohtani, E. and H. Sawamoto (1987). Melting experiments on a model chondritic mantle composition at 25 gpa. *Geophys. Res. Lett.* 14(7), 733–736.
- Pari, G. and W. R. Peltier (1996). The free-air gravity constraint on subcontinental mantle dynamics. *J. Geophys. Res.* 101, 28,105–28,132.
- Pavlenkova, N. I., G. A. Pavlenkova, and L. N. Solodilov (1996). High velocities in the uppermost mantle of the Siberian craton (in 'kimberlites and structure of cratonic lithosphere'). *Tectonophysics* 262, 51–65.
- Pavlenkova, N. I. and A. V. Yegorkin (1983). Upper mantle heterogeneity in the northern part of Eurasia. *Physics of the Earth and Planetary Interiors* 33, 180–193.
- Pearson, D. G. (1997). The age of continental roots. In *Workshop on continental roots*. Harvard University & Massachusetts Institute of Technology.
- Polet, J. and D. L. Anderson (1995). Depth extent of cratons as inferred from tomographic studies. *Geology* 23(3), 205–208.
- Pollack, H. (1997). *Greenstone Belts* (eds. de Wit, M. J. & Ashwal, L. D.), Chapter: Thermal characteristics of the Archaean, pp. 223–232. Oxford University Press.
- Pollack, H. N. (1986). Cratonization and thermal evolution of the mantle. *Earth Plan. Sci. Lett.* 80, 175–182.
- Pollack, H. N. and D. S. Chapman (1977). On the regional variation of heat flow, geotherms, and lithospheric thickness. *Tectonophysics* 38, 279–296.
- Pollack, H. N., S. J. Hurter, and J. R. Johnson (1993). Heat flow from the earth's interior: analysis of the global data set. *Reviews of Geophysics* 31, 267–280.
- Press, W. H., B. P. Flannery, S. A. Teukolsky, and W. T. Vetterling (1992). *Numerical Recipes, the art of scientific programming*. New York: Cambridge University Press.
- Ranalli, G. (1986). *Rheology of the Earth: Deformation and flow processes in geophysics and geodynamics*. London, U.K.: Allen & Unwin.
- Ranalli, G. (1991). *Glacial Isostasy, Sea-Level and Mantle Rheology* (Eds. Sabadini, R. et al.), Chapter: The microphysical approach to mantle rheology, pp. 343–378. Kluwer, The Netherlands.
- Revenaugh, J. and T. H. Jordan (1991c). Mantle layering from ScS reverberations 3: The upper mantle. *J. Geophys. Res.* 96, 19,781–19,810.
- Ribe, N. M. and U. R. Christensen (1994). Melt generation by plumes; a study of Hawaiian volcanism. *J. Geophys. Res.* 99, 669–682.
- Ringwood, A. E. (1982). Phase transformations and differentiation in subducted lithosphere: Implications for mantle dynamics, basalt petrogenesis, and crustal evolution. *Journal of Geology* 90, 611–643.
- Roermund, H. L. M. and M. R. Drury (1998). An ultra-deep ($d > 200$ km) orogenic peridotite body in western Norway. In *Fall Meeting abstracts*, Volume V21E-03, pp. F971. AGU.
- Rudnick, R. L. (1995). Making continental crust. *Nature* 378, 571–578.
- Rudnick, R. L., W. F. McDonough, and R. J. O'Connell (1998). Thermal structure, thickness and composition of continental lithosphere. *Chemical Geology* 145, 395–411.
- Schmeling, H. (1999). *Physics and Chemistry of Partially Molten Rocks* (Eds. Bagdassarov, N., Laporte, D. & Thompson, A. B.), Chapter: Partial melting and melt segregation in a convecting mantle. Kluwer Academic Publishers, The Netherlands.
- Schmeling, H. and G. Y. Bussod (1996). Variable viscosity convection and partial melting in the continental asthenosphere. *J. Geophys. Res.* 101, 5411–5423.
- Schott, B. and H. Schmeling (1998). Delamination and detachment of a lithospheric root. *Tectonophysics* (Submitted).
- Segal, A. (1982). Aspects of numerical methods for elliptic singular perturbation problems. *SIAM J. Sci. Stat. Comput.* 3(3), 327–349.
- Segal, A. and N. Praagman (1995). *Sepran user manual*. Sepra, Leidschendam, The Netherlands.
- Sethian, J. (1996). *The Level Set Methods*. Cambridge Univ. Press.
- Sleep, N. H. and B. F. Windley (1982). Archean plate tectonics: constraints and inferences. *Journal of Geology* 90, 363–379.
- Sotin, C. and E. M. Parmentier (1989). Dynamical consequences of compositional and thermal density stratification beneath spreading centers. *Geophys. Res. Lett.* 16, 835–838.

- Sparks, D. W. and E. M. Parmentier (1993). The structure of three-dimensional convection beneath oceanic spreading centers. *Geophys. J. Int.* 112, 81–91.
- Spiegelman, M. (1993a). Flow in deformable media. part 1: Simple analysis. *J. Fluid. Mech.* 247, 17–38.
- Spiegelman, M. (1993b). Flow in deformable media. part 2: Numerical analysis - the relationship between shock waves and solitary waves. *J. Fluid. Mech.* 247, 39–63.
- Spiegelman, M. (1993c). Physics of melt extraction: theory, implications and applications. *Phil. Trans. R. Soc. Lond. A* 342, 23–41.
- Steinbach, V. (1991). *Numerische Experimente zur Konvektion in kompressiblen Medien*. Ph. D. thesis, Mitteilungen aus dem Institut für Geophysik und Meteorologie der Univ. zu Koeln. 79.
- Steinbach, V., U. Hansen, and A. Ebel (1989). Compressible convection in the Earth's mantle: a comparison of different approaches. *Geophys. Res. Lett.* 16, 633–635.
- Steinbach, V. and D. A. Yuen (1994). Effects of depth-dependent properties on the thermal anomalies produced in flush instabilities from phase transitions. *Physics of the Earth and Planetary Interiors* 86, 165–183.
- Su, W.-j., R. L. Woodward, and A. M. Dziewonski (1994). Degree 12 model of shear velocity heterogeneity in the mantle. *J. Geophys. Res.* 99, 6945–6980.
- Takahashi, E. (1986). Melting of a dry peridotite KLB-1 up to 14 GPa: Implications on the origin of peridotitic upper mantle. *J. Geophys. Res.* 91, 9367–9382.
- Takahashi, E. (1990). Speculations on the Archean mantle: missing link between komatiite and depleted garnet peridotite. *J. Geophys. Res.* 95, 15,941–954.
- Takahashi, E. and I. Kushiro (1983). Melting of a dry peridotite at high pressure and basalt magma genesis. *Am. Miner.* 68, 859–879.
- Taylor, S. R. and S. M. McLennan (1985). *The Continental Crust: its Composition and Evolution, An Examination of the Geochemical Record Preserved in Sedimentary Rocks*. Geoscience Texts. Blackwell Scientific Publications.
- Ten, A., D. A. Yuen, T. B. Larsen, and A. V. Malevsky (1996). The evolution of material surfaces in convection with variable viscosity as monitored by a characteristics-based method. *Geophys. Res. Lett.* 23, 2001–2004.
- Trampert, J. (1998). Global seismic tomography: The inverse problem and beyond. *Inverse Problems* 14, 371–385.
- Trampert, J. and J. H. Woodhouse (1996). High resolution global phase velocity distribution. *Geophys. Res. Lett.* 23, 21–24.
- Turcotte, D. L. and G. Schubert (1982). *Geodynamics; Applications of continuum physics to geological problems*. John Wiley & Sons.
- Vacher, P., A. Mocquet, and C. Sotin (1998). Computation of seismic profiles from mineral physics: The importance of the non-olivine components for explaining the 660 km depth discontinuity. *Physics of the Earth and Planetary Interiors* 106, 275–298.
- Van Den Berg, A. P., P. E. Van Keken, and D. A. Yuen (1993). The effects of a composite non-Newtonian and Newtonian rheology on mantle convection. *Geophys. J. Int.* 115, 62–78.
- Van Keken, P. E. (1993). *Numerical modelling of thermochemically driven flow with non-Newtonian rheology: applied to the Earth's lithosphere and mantle*. Ph. D. thesis, Utrecht University; Geologica Ultraiectina. no. 107.
- Van Keken, P. E., S. D. King, H. Schmeling, U. R. Christensen, D. Neumeister, and M.-P. Doin (1997). A comparison of methods of the modeling of thermochemical convection. *J. Geophys. Res.* 102, 22,477–22,495.
- Vitarello, I. and H. N. Pollack (1980). On the variation of continental heat flow with age and the thermal evolution of continents. *J. Geophys. Res.* 85, 983–995.
- Vlaar, N. J. (1985). *The Deep Proterozoic Crust in the North Atlantic Provinces (Eds. Tobi, A. C. & Touret, J. L. R.)*, Chapter: Precambrium geodynamical constraints, pp. 3–20. D. Reidel Publishing Company.
- Vlaar, N. J. (1986). Archaean global dynamics. *Geologie en Mijnbouw* 65, 91–101.
- Vlaar, N. J. and A. P. Van Den Berg (1991). *Glacial Isostasy, Sea-Level and Mantle Rheology (Eds. Sabadini, R. et al.)*, Chapter: Continental evolution and Archaean-sea-level, pp. 637–662. Kluwer, The Netherlands.
- Vlaar, N. J., P. E. Van Keken, and A. P. Van Den Berg (1994). Cooling of the Earth in the Archaean; consequences of pressure-release melting in a hotter mantle. *Earth Plan. Sci. Lett.* 121, 1–18.
- Vreugdenhil, C. B. and B. Koren (Eds.) (1993). *Numerical Methods for Advection-Diffusion Problems*, Volume 45 of *Notes on Numerical Fluid Mechanics*. Braunschweig, Germany: Vieweg.
- Walzer, U. and R. Hendel (1997). Time-dependent thermal convection, mantle differentiation and continental-crust growth. *Geophys. J. Int.* 130, 303–325.

- Waugh, D. W. and R. A. Plumb (1994). Contour advection with surgery: A technique for investigating fine-scale structure in tracer transport. *J. Atmos. Sci.* 51, 530–540.
- White, R. and D. McKenzie (1989). Magmatism at rift zones: the generation of volcanic continental margins and flood basalts. *J. Geophys. Res.* 94, 7685–7729.
- Windley, B. F. (1995). *The evolving continents*. England: John Wiley & Sons.
- Woodhouse, J. H. and J. Trampert (1995). Global upper mantle structure inferred from surface wave and body wave data. In *Fall Meeting abstracts*, Volume S42C-9, pp. F422. AGU.
- Yoshioka, S., R. Daessler, and D. A. Yuen (1997). Stress fields associated with metastable phase transitions in descending slabs and deep-focus earthquakes. *Earth Plan. Sci. Lett.* 104, 345–361.
- Zhang, Y.-S. and T. Tanimoto (1993). High-resolution global upper mantle structure and plate tectonics. *J. Geophys. Res.* 98, 9793–9823.

Appendix A

FORMULATION OF PARTIAL MELTING SOURCE TERM

The inexact differential of the degree of depletion dF can be expressed in terms of the solidus and liquidus temperatures T_s and T_l , and a melting curve $f(\Theta)$ in terms of the ‘super-solidus temperature’ Θ . We relate F and f through

$$F(p, T) = f\left(\frac{T - T_s(p)}{T_l(p) - T_s(p)}\right) = f\left(\frac{T - T_s(p)}{\Delta T_{sl}(p)}\right) = f(\Theta) \quad (\text{A.1})$$

where T is the dimensioned temperature and Θ is the normalized ‘super-solidus temperature’, with $0 \leq \Theta \leq 1$, i.e. in between solidus and liquidus. The differential dF is given by

$$dF = \frac{\partial F}{\partial p} dp + \frac{\partial F}{\partial T} dT \quad (\text{A.2})$$

where the partial derivatives are defined as,

$$\begin{aligned} A(p, T) = \frac{\partial F}{\partial p} &= \frac{df}{d\Theta} \frac{\partial \Theta}{\partial p} \\ &= \frac{df}{d\Theta} \left[-\Delta T_{sl}^{-1} \frac{dT_s}{dp} - (T - T_s) \Delta T_{sl}^{-2} \frac{d}{dp} \Delta T_{sl} \right] \end{aligned} \quad (\text{A.3})$$

$$B(p, T) = \frac{\partial F}{\partial T} = \frac{df}{d\Theta} \frac{\partial \Theta}{\partial T} = \Delta T_{sl}^{-1} \frac{df}{d\Theta} \quad (\text{A.4})$$

In (A.3) and (A.4) the slope of the phase equilibrium lines dT_s/dp is treated as a known constant material property.

Recurrent melting in recycled depleted material will only take place if the volume is subject to super-solidus temperatures that exceeds any previously experienced value. Therefore, the source term \mathcal{P} is also F -dependent: $\mathcal{P}(p, T, F)$.

Appendix B

DISCRETIZED FORM OF THE ENERGY EQUATION

The non-dimensional form of the energy equation (Equation 2.23) is:

$$\begin{aligned} \frac{dT'}{dt'} - Di(T' + T'_0)w' &= \\ \nabla^2 T' + \mathcal{R}H' + \frac{Di}{Ra}\Phi' - \frac{\Delta S}{c_p} \frac{dF'}{dt'}(T' + T'_0) - \sum_{i=1,2} \frac{X_i \Delta S_{\Gamma_i}}{c_p} \frac{d\Gamma'_i}{dt'}(T' + T'_0) & \end{aligned} \quad (\text{B.1})$$

where the primes indicate non-dimensional symbols. In the following, we show how the different incorporated physical aspects contribute to the mass matrix \mathbf{M} , stiffness matrix \mathbf{S} , and the right-hand-side vector \mathbf{R} of the discretized energy equation (Eq 3.1).

With the expression for dF' introduced in Appendix A we find with the pressure scaling given in Table 2.4:

$$\frac{dF'}{dt'} = \frac{\rho_0 g h^3}{\kappa \eta_0} A' w' + B' \frac{dT'}{dt'} \quad (\text{B.2})$$

For the phase-transitions and corresponding phase functions Γ'_i we have in terms of reduced pressures π'_i (see Table 2.1 and 2.2):

$$\frac{d\Gamma'_i}{dt} = \frac{d\Gamma'_i}{d\pi'_i} \frac{d\pi'_i}{dt} = \frac{d\Gamma'_i}{d\pi'_i} \left(\frac{d\pi'_i}{dp} \frac{dp}{dt} + \frac{d\pi'_i}{dT} \frac{dT}{dt} \right) \quad (\text{B.3})$$

and non-dimensionalization yields:

$$\frac{d\Gamma'_i}{dt'} = \frac{d\Gamma'_i}{d\pi'_i} \left(\frac{\rho_0 g h^3}{\kappa \eta_0} w' - \gamma'_i \frac{dT'}{dt'} \right) \quad (\text{B.4})$$

where $d\Gamma'_i/d\pi'_i$ is defined by Equations 2.12 and 2.13 in the Boussinesq Approximation for which one of the assumptions is $p = \rho_0 g z$. Substituting Expressions B.2 and B.4 into the non-dimensional energy equation (Equation B.2) and applying the expression for the total derivative of T' :

$$\frac{dT'}{dt'} = \frac{\partial T'}{\partial t'} + \vec{u}' \cdot \nabla T' \quad (\text{B.5})$$

results in an equation of the form:

$$F'_C \left(\frac{\partial T'}{\partial t'} + \vec{u}' \cdot \nabla T' \right) - \nabla^2 T' + F'_T T' = F'_R \quad (\text{B.6})$$

with:

$$F'_C \equiv \left[1 + \frac{\Delta S}{c_p} B'(T' + T'_0) + \sum_{i=1,2} \frac{\delta_i \rho X_i}{\rho_0} \frac{d\Gamma'_i}{d\pi'_i} (\gamma'_i)^2 \frac{Di}{Ra} (T' + T'_0) \right] \quad (\text{B.7})$$

$$F'_T \equiv \left[\frac{\Delta S}{\alpha c_p \Delta T} \frac{Ra}{Di} A' - \sum_{i=1,2} \frac{d\Gamma'_i}{d\pi'_i} \gamma'_i \frac{Rb_{\Gamma_i}}{Ra} - 1 \right] Di w' \quad (\text{B.8})$$

$$F'_R \equiv \left[\mathcal{R}H' + \frac{Di}{Ra} \Phi' - \left(\frac{\Delta S}{\alpha c_p \Delta T} \frac{Ra}{Di} A' - \sum_{i=1,2} \frac{d\Gamma'_i}{d\pi'_i} \gamma'_i \frac{Rb_{\Gamma_i}}{Ra} - 1 \right) Di w' T'_0 \right] \quad (\text{B.9})$$

The two last terms of F'_C contain the temperature and make the energy equation non-linear. Furthermore, A' is T' -dependent which causes a non-linearity through the first term of F'_T and the third term of F'_R . In time-dependent computations these terms are linearized where necessary, using the values computed from the most recent available temperature solution.

The weak formulation of this equation is:

$$\int_V F'_C \frac{\partial T'}{\partial t'} v dV + \int_V \{ F'_C \vec{u}' \cdot \nabla T' - \nabla^2 T' + F'_T T' \} v dV = \int_V F'_R v dV \quad (\text{B.10})$$

where V is the 2-D domain with boundary ∂V and v is a test-function. Applying the Gauss divergence theorem:

$$\int_V \nabla^2 T' v dA = - \int_V \nabla v \cdot \nabla T' dV + \oint_{\partial V} v \nabla T' \cdot \hat{n} dA \quad (\text{B.11})$$

we find:

$$\begin{aligned} \int_V F'_C \frac{\partial T'}{\partial t'} v dV + \int_V \{ F'_C \vec{u}' \cdot \nabla T' v + \nabla v \cdot \nabla T' + F'_T T' v \} dV \\ = \int_V F'_R v dV - \oint_{\partial V} v \nabla T' \cdot \hat{n} dV \end{aligned} \quad (\text{B.12})$$

We expand the spatial part of $T'(\vec{x}', t')$ in basis functions $N_J(\vec{x}')$:

$$T'(\vec{x}') = \sum_J N_J(\vec{x}') T'_J, \quad \text{with } T'_J = T'(\vec{x}'_J, t') \quad (\text{B.13})$$

and in the Bubnov-Galerkin formulation the test-function v is specified as the basis function $N_I(\vec{x}')$. This gives for the energy equation:

$$\begin{aligned}
 & \sum_J \frac{\partial T'_J}{\partial t'} \int_V F'_C N_I N_J dV \\
 & + \\
 & \sum_J T'_J \int_V \{F'_C(\vec{u}' \cdot \nabla N_J) N_I + (\nabla N_J \cdot \nabla N_I) + F'_T N_J N_I\} dV \\
 & = \\
 & \int_V F'_R N_I dV - \oint_{\partial V} N_I \nabla T' \cdot \hat{n} dA
 \end{aligned} \tag{B.14}$$

On the vertical model boundaries homogeneous natural boundary conditions are imposed. As a result, the boundary integral contribution vanishes on the vertical boundaries. On the horizontal boundaries the prescribed temperature represents an essential boundary condition, which results in a vanishing boundary integral term in Equations B.9 and right-hand-side contribution to the Equations B.7-B.9. The mass matrix \mathbf{M} is defined by:

$$M_{IJ} = \int_V F'_C N_I N_J dV \tag{B.15}$$

The stiffness matrix \mathbf{S} is defined by:

$$S_{IJ} = \int_V \{F'_C(\vec{u}' \cdot \nabla N_J) N_I + (\nabla N_J \cdot \nabla N_I) + F'_T N_J N_I\} dV \tag{B.16}$$

and the right-hand-side vector \mathbf{R} is defined by:

$$R_{IJ} \int_V F'_R N_I dV \tag{B.17}$$

If SUPG techniques are applied, the test-function v is velocity-dependent and identical to the basis functions. For time-dependent upwind techniques the test-function also depends on the time-step.

SUMMARY

This thesis elaborates on the evolution of the continental upper mantle based on numerical modelling results. The descriptive and explanatory basis is formed by a numerical thermo-chemical convection model. The model evolution starts in the early Archaean about 4 billion years ago. The model follows from the conservation equations, which are based on the physical laws describing the upper mantle. Several simplifications have been made as is common practice in model studies. Nowadays, modern high- and top-end computers pave the way for these increasingly realistic simulations. Qualitative scenarios can now be tested and furthermore modelling may reveal new dynamical concepts, which had not been proposed.

Several observations indicate that the continental lithosphere is essentially different from present-day oceanic lithosphere. Dating shows that the majority of continental crust is old compared to present-day oceanic crust. Ages of cratons reach up to 4 billion years. These ages contrast strongly with the maximum age (180 million years) for modern oceanic lithosphere. This implies that continental fragments have been buoyant enough to remain at the surface for almost the entire Earth's history. In addition, this continental stabilization was apparently established during early stages of the Earth's evolution. The concept of plate tectonics adequately explains the young ages of oceanic plates by means of plate generation at Mid Ocean Ridges (MOR's) and destruction during subduction at oceanic trenches.

In addition to the age, other significant differences exist between the two crustal types. The continental crust has a non-uniform thickness from 20 to 60 kilometers, a largely variable composition, and a low density when compared to oceanic crust. The modern oceanic crust has an almost uniform thickness of 6 to 7 kilometers and a basaltic composition.

The shallow part of the upper mantle that underlies old continental shields and cratons is characterized by high seismic velocities when compared to oceanic upper mantle at identical depths. This implies that the continental upper mantle is cold, a conclusion which is consistent with the observed low surface heat flow values for these areas and accordingly derived cold geotherms. The difference in the thermal state is not the only indication that continents have roots that can extend to large depths. Upper mantle samples, in the form of xenoliths, from depths up to 200 kilometers have been described. These rock fragments imply that the continental lithosphere has a specific composition and density up to large depths. Furthermore, upper mantle material in the form of peridotite massives confirm the specific compositional and thermal state of the continental mantle. However, the available information is not unambiguous. The mechanism that can explain the majority of these findings forms the basis of the evolution of the dynamical model used here.

The process of pressure-released partial melting that occurs during the upwelling of upper mantle material can explain several of the aspects that have been summarized above. The composition of the solid residual rock changes gradually, due to the gradual formation of melt during partial melting. The mass fraction of the melt generated, is called the degree of depletion, can be used as an indicator for the density change of the solid residue upon melting. This density effect results from the associated change in composition. In our model this density reduction is the most important effect of partial melting on the dynamics of the continental upper mantle. The associated consumption of latent heat is significant and thus also included in the model formulation. The resulting decrease in thermal buoyancy is smaller than the counteracting compositional

effect. As a result, the intrinsically low density of the depleted upper mantle rock prevents the rock from taking part in large-scale thermal upper mantle convection.

In the model the compositional and thermal effects of partial melting are combined with an initial scenario for the evolution of the continental upper mantle. A thick crust with a high concentration of heat producing radioactive elements thermally isolates the underlying mantle. The concentration of heat producing elements used is 2 to 3 times higher than the present-day value. This higher concentration is thought to represent an Archaean situation. A statistically stationary initial state for the upper mantle model is dynamically created. The resulting averaged mantle temperature is several hundreds of degrees higher than present-day mantle temperatures. This is assumed to be a valid thermal state of the early Earth and the initial formation of a continental root takes place rapidly in this relatively hot upper mantle model.

The scenario used explains the presence of a thick, compositionally differentiated, and relatively cold continental roots underneath the cratonic crust as presently observed. Furthermore, it is plausible within the model restrictions that the majority of the depleted continental root forms a stable system over a time-span of several billion years. This long-term stability is partly caused by the rheology applied in the model. In addition to the compositional and thermal buoyancy effects, rheology has a large influence on the convection regime. The temperature- and pressure-dependent viscosity used has an important stabilizing effect on the shallow upper mantle. During the long term evolution the more mobile deeper part of the depleted root takes an active part in the process of thermo-chemical convection, which results in large lateral variations of continental root thicknesses.

Importantly, the model reveals the possible occurrence of a phenomenon not seen before in numerical modelling studies and these can be used to explain observations in a new context. Cooling from the top triggers thermal convection in the deeper part of the upper mantle. In hot upwellings the solidus is crossed by undepleted rock and partial melting is initiated. Due to the decrease in effective density, this upwelling process accelerates the ascending and melting centre leading to a small-scale diapir, which adds depleted material to the root. This intermittent process results in compositional variations within the root. At the same time, the overall structure of the compositionally differentiated root remains unchanged. The degree of depletion gradually increases from high to low with increasing depths.

Furthermore, when partial melting is described using realistic phase relations, deep mantle differentiation occurs in the model. This phenomenon of deep melting is studied by means of an isentropic, one-dimensional kinematic model. It is proposed that in a hot Archaean upper mantle the process of partial melting might be initiated at greater depths than previously thought. If correct, the depth at which the associated komatiitic melting starts is pushed to much higher figures.

SAMENVATTING (SUMMARY IN DUTCH)

In dit proefschrift wordt de evolutie van de continentale bovenmantel bestudeerd aan de hand van een numeriek model. De model evolutie begint ongeveer 4 miljard jaar geleden in het vroege Archaïcum. De beschrijvende en verklarende basis wordt gevormd door een numeriek thermo-chemisch convectie model waarin de vergelijkingen, corresponderend met de fysische behoudswetten zoals deze gelden voor de bovenmantel, worden opgelost. Zoals gebruikelijk in model studies zijn er diverse simplificaties in het model opgenomen. Met behulp van moderne computers zijn model berekeningen als deze mogelijk geworden en kunnen steeds realistischer simulaties gemaakt worden. Kwalitatieve scenario's die in de loop der tijd voorgesteld zijn kunnen getoetst en gequantificeerd worden. Het is tevens mogelijk dat in een model nieuwe dynamische scenario's worden waargenomen die nog niet eerder geopperd zijn.

Diverse observaties duiden erop dat de continentale lithosfeer essentieel verschilt van de huidige oceanische lithosfeer. Uit dateringen van continentale korst blijkt dat het merendeel relatief oud is in vergelijking met moderne oceanische korst. Ouderdommen van cratons, de oudste continent segmenten, reiken tot ongeveer 4 miljard jaar. Dit terwijl de oudste huidige oceanische lithosfeer een leeftijd van slechts 180 miljoen jaar heeft. Dit impliceert dat delen van continenten gedurende vrijwel de gehele Aardse evolutie zijn blijven drijven aan het aardoppervlak en vroeg zijn gestabiliseerd. Een dergelijke stabiliteit gaat voor hedendaagse oceanische lithosfeer niet op. Binnen het concept van de plaattectoniek is de leeftijd van oceanische platen te verklaren door middel van de generatie van nieuwe oceanische lithosfeer bij een Mid Oceanische Rug (MOR) en subductie in de diepzee troggen bij continentranden.

Naast het leeftijdsverschil van beide types korst zijn er andere significante verschillen. Continentale korst heeft een niet uniforme dikte van 20 tot 60 kilometer en een sterk variërende samenstelling met, in vergelijking tot oceanische korst, een relatief lage dichtheid. Bepaald is dat basaltisch gesteente de huidige oceanische korst vormt die een vrijwel uniforme dikte heeft van 6 à 7 kilometer.

De ondiepere bovenmantel onder oude continentale schilden en cratons heeft seismische snelheden die hoger zijn dan de snelheden die gevonden worden op vergelijkbare diepte in de oceanische bovenmantel. Dit impliceert dat de continentale mantel koud is. De gemeten lage warmtestroom aan het aardoppervlak voor deze gebieden en de daaruit afgeleide geothermen vormen indicaties die aangeven dat het concept van een koude continentale lithosfeer consistent is. Dit verschil in de thermische toestand is niet de enige aanwijzing dat continenten zogenoemde wortels hebben die tot diep in de bovenmantel kunnen reiken. Xenolieten die de continentale bovenmantel bemonsteren over een diepte tot ongeveer 200 kilometer impliceren een specifieke compositie en dichtheid van continentale lithosfeer tot op grote diepte. Daarnaast worden er andere monsters van mantelmateriaal gevonden aan het aardoppervlak in de vorm van peridotietmassieven die vermoedelijk op hetzelfde duiden. Het mechanisme dat deze compositie grotendeels kan verklaren vormt de basis van het hier gebruikte dynamische evolutie model.

Het proces van het partiël smelten door decompressie dat plaatsvindt tijdens het opwellen van bovenmantel materiaal, kan diverse van de bovengenoemde aspecten verklaren. Door de geleidelijke vorming van smelt tijdens het partiël opsmelten van stijgend bovenmantel gesteente, verandert de samenstelling van het vaste residu geleidelijk. De massafractie van de gevormde smelt, ofwel de depletiegraad, is indicatief voor de dichtheidsverlaging van het residu als gevolg van de met het partiël smelten

gepaard gaande compositionele wijziging. Deze dichtheidsafname is het belangrijkste effect dat partieel smelten heeft op de continentale bovenmantel dynamica in het hier gepresenteerde model. De met het partiële decompressie smelten gepaard gaande consumptie van latente warmte is significant en is daarom opgenomen in het model. De hierdoor veroorzaakte afname van het thermisch drijfvermogen is geringer dan het tegenovergestelde compositionele effect. Het is daarom onder andere de intrinsiek lage dichtheid die kan voorkomen dat dit gedepleteerde gesteente deel kan nemen aan convectorie op de schaal van de gehele bovenmantel.

Dit compositionele en thermische effect van partieel smelten wordt in het model gecombineerd met een startscenario voor de evolutie van het model van de continentale bovenmantel. Een dikke korst met een hoge concentratie van radioactieve warmteproducerende elementen heeft een thermisch isolerende werking op de eronder gelegen mantel. De concentratie van warmteproducerende elementen in het model is 2 tot 3 keer hoger dan vandaag de dag, hetgeen verondersteld wordt overeen te komen met de situatie tijdens het Archaïcum. Dynamisch wordt een statistische stationaire toestand voor de bovenmantel gecreëerd. De resulterende gemiddelde manteltemperatuur is enkele honderden graden hoger dan de hedendaagse manteltemperatuur en de hogere manteltemperatuur wordt verondersteld representatief te zijn voor de vroege Aarde. In dit model vindt de formatie van de continentale wortel in deze relatief warme mantel plaats.

Het gebruikte scenario verklaart de aanwezigheid van een compositioneel gedifferentieerde en relatief koude continentale wortel die onder de cratonische korst ligt en vermoedelijk tot grote diepte kan reiken. Daarnaast is binnen de modelrestricties aannemelijk gemaakt dat het grootste deel van de oude gedepleteerde continentale bovenmantel stabiel kan zijn gedurende enkele miljarden jaren. Dit wordt voor een deel bewerkstelligd door de gebruikte rheologie. Naast het door de thermische en compositionele toestand bepaalde drijfvermogen, is het de rheologie die het convectieregiemede beïnvloedt. De temperatuur- en drukafhankelijkheid van de viscositeit heeft een belangrijke stabiliserende werking op de ondiepe mantel. Gedurende de lange evolutie blijkt dat het meer mobiele diepere deel van de gedepleteerde wortel tot grote laterale variaties in de diepte van de wortel kan leiden.

Een verschijnsel dat zich voordoet in het model kan tevens diverse andere waarnemingen verklaren of deze waarnemingen in een nieuw kader plaatsen. De afkoeling van de continentale wortel van boven af veroorzaakt thermische convectorie in de diepere bovenmantel. In warme opwellingen wordt de solidus overschreden worden door niet gedepleteerd mantelmateriaal dat vervolgens begint te smelten. Door de afnemende dichtheid versnelt de partieel smeltende kern en vormt een kleine diapier die gedepleteerd materiaal aan de wortel toevoegt. Dit pulserend verlopend proces geeft aanleiding tot compositionele variaties in de wortel. Tegelijkertijd blijft de globale opbouw van de compositoneel gedifferentieerde wortel intact. Op geringe diepte heeft de wortel een hoge depletiegraad die met toenemende diepte geleidelijk afneemt.

Verder vindt er in het model diepe manteldifferentiatie plaats wanneer een realistisch fase-diagram wordt gebruikt voor de beschrijving van het partieel smelten. Dit fenomeen van diep smelten wordt aan de hand van een eenvoudig ééndimensionaal isentroop en kinematisch model bestudeerd. Gesuggereerd wordt dat in een warme Archaïsche bovenmantel het proces waarbij komatiïtische smelt wordt gevormd wellicht op grotere diepte start dan tot nu toe verondersteld werd.

DANKWOORD (ACKNOWLEDGMENTS)

Dit proefschrift is vanzelfsprekend tot stand gekomen met de medewerking van vele personen. In de eerste plaats wil ik mijn promotor Prof. dr. N.J. Vlaar bedanken voor zijn bijdrage in mijn academische vorming. Hij heeft mij enthousiast weten te maken voor de thermodynamische problemen die naar voren komen bij het proces van partiëel smelten van bovenmantel gesteenten en dan met name de fascinerende problematiek rond de toepassing van dit proces op het Archaïcum. Dit werk borduurt voort op de concepten die Prof. dr. N.J. Vlaar al in de jaren zeventig bedacht en die hij nog steeds weet te verfijnen. Ik heb waardering voor de eerlijke wetenschappelijke discussies die ik met hem heb mogen voeren. Er zijn nog steeds een aantal punten waarover we van mening verschillen. Ik voel me echter verplicht om het hem te laten weten wanneer ook die in zijn voordeel beslecht gaan worden.

Vervolgens gaat speciale dank uit naar dr. Arie van den Berg, mijn co-promotor en dagelijks begeleider. Gedurende de vele uren discussie heeft hij de inbreng gegeven die onmisbaar is gebleken om dit resultaat neer te zetten. Met name op momenten dat de onderzoeksresultaten er vrij hopeloos uitzagen, bleef hij mij stimuleren om weer nieuwe potentiële uitwegen uit te proberen. Even belangrijk is dat hij tevens mijn enthousiasme tactvol de kop in heeft weten te drukken wanneer de balans gelukkig ook eens naar de andere kant uitsloeg. Zowel zijn integriteit als die van Prof. dr. N.J. Vlaar heb ik zeker gewaardeerd.

I am very grateful to Prof. dr. David Yuen. He stimulated this work by making the computational resources of the Minnesota Supercomputer Institute available to me. We have also shared many other resources in the vicinity of the institute. It is not clear to me whether it helped to improve the scientific contents of this thesis or not, but we cannot be blamed for not exploring this option. In addition, these sessions increased my appreciation for the Minnesotans.

Peter van Keken wil ik met name bedanken voor het vereenvoudigen van mijn eerste stappen aan de andere kant van de grote plas. Daarnaast hoefde ik hem maar te vragen naar code en data om het vervolgens instantaan te krijgen. Oplossingen voor hem bekende problemen die ik soms had op diverse computerplatformen heeft hij ook altijd meteen doorgesluisd. Dit heeft soms kostbare tijd bespaard.

Onlangs de ongewenste verassingseffecten die enkele P-instructies soms hadden, voel ik me verplicht om de schrijvers van dit grafische hulpmiddel te bedanken. Zij, Wim Spakman, Marc de Jonge en Rob Govers, stonden altijd klaar om diverse speciale effecten weer om te buigen naar minder spectaculaire, maar wetenschappelijk correcte, visualisaties. Op slechts één figuur na zijn alle figuren in dit proefschrift met P gemaakt.

Joop Hoofd en Theo van Zessen bedank ik beiden voor het operationeel houden van alle computerfaciliteiten die ik in Utrecht op de Faculteit Aardwetenschappen tot mijn beschikking had. Voor hun bekwaamheid en grenzeloze inzet kan niet genoeg waardering worden opgebracht. Een proefschrift als dit kan niet tot stand komen zonder hun continue aanwezigheid en allertheid. Naast het voorkomen van zware fysieke mishandeling van het magisch sillicium, hebben zij diverse kleinere maar tastbare zaken altijd voor mij geregeld. Soms zonder dat ik er weet van had. Het is meermaals voorgekomen dat ik meende dat vele op band opgeslagen bits en bytes niet meer terug te lezen waren waardoor ik ze als overleden beschouwde. Dit bleek echter een toestand van schijn dood te zijn en Joop dan wel Theo bleek wel in staat te zijn om de bandjes te reanimeren. Daarnaast lazen zij tapes uit op momenten dat ik in Minneapolis zat en CD's werden zo snel gebakken dat ze ik ze soms nog rondspinnend op mijn bureau aantrof.

Gedurende mijn studie en promotieonderzoek hebben de volgende personen mij met theoretische en praktische numerieke kennis bijgestaan: Aad van der Steen, Gerard Sleijpen, Guus Segal, Cees Vuijk, Henk van der Vorst. Enkele samenwerkingsprojecten zijn door tijdsgebrek nooit uitgegroeid tot een volwassenheid waarop we hadden gehoopt. The people from Technical Support at MSI and those supporting the specific platforms available to MSI visitors are also thanked for their frequent help.

De data gebruikt voor diverse figuren zijn verkregen met de hulp van de volgende mensen: Paul Meijer, Rob Govers, Axel Rühm, Jeannot Trampert, Peter van Keken en Wim Spakman. Met Saskia Goes en Pierre Vachez heb ik diverse discussies gehad die mee hebben geholpen bij het totstandkomen van Hoofdstuk 8. Tevens had ik beschikking over hun code. Bernard de Jong heeft mijn inzichten in de petrologie weten te vergroten door precies aan te wijzen wat er bekend is. Helaas gebeurde dit in een zo laat stadium dat de petrologie wat laat voor mij tot leven kwam. Martyn Drury, Herman van Roermund, and Michel Jacobs have been very supportive in explaining several aspects of mantle rocks, which are relevant within the context of this thesis. Discussies met Tanja Zegers hebben mijn begrip voor diverse geologische aspecten met betrekking tot het Archaïcum vergroot. Paul Mason, Rob McDonnell, and Bas Kooi are thanked for there help with correcting my English.

Het delen van een kamer met Jeroen van Hunen gedurende meer dan twee jaar was een waar genoegen. Zijn grenzeloos optimisme in combinatie met een gezonde vracht humor maakte het een bijzonder aangenaam verblijf. Verder heeft hij nog talloze kleine foutjes gevonden tijdens het doorlezen van het manuscript, waarvoor dank. Daarnaast bleek de koffiezetter natuurlijk ook erg goed van pas te komen.

Het team van de AV-dienst onder aanvoering van Paul van Oudenallen bedank ik voor het altijd klaarstaan om vragen te beantwoorden met betrekking tot de mogelijkheden van grafische software. Alhoewel ik niet uitgebreid gebruik heb gemaakt van hun mogelijkheden, leverden zij op diverse cruciale momenten de nodige input en hulp. De medewerkers van de bibliotheek bedank ik hierbij ook voor hun medewerking bij het opsporen van diverse werken.

Mijn ouders, broers en zussen bedank ik voor hun begrip dat ze hebben opgebracht omdat ik zonodig het promotiepad op wilde. Wellicht hebben ze me nog nooit zo weinig gezien. Ik hoop dat Suzanne van Ratingen niet al teveel geleden heeft van mijn promotietijd en met name dan de perioden dat ik in het buitenland zat. Ik wil haar naast al het andere in ieder geval bedanken voor het niet klagen. Ron and Judy and their friends and relatives made live more pleasant in and around the Twin Cities during my stays in Minneapolis.

Ik heb genoten van de kroeg-sessies die op een of andere manier niet te voorkomen waren met de volgende personen: Láslo Evers, Mark Petit, Volker Steinbach, Bas Kooi, Jeroen Godtschalk, H el ene Avenarius, Rob Berendsen, Martijn Verwoerd en enkele anderen op een minder regelmatige basis. Het samenzijn met twee of meer van genoemde personen staat borg voor een avondvullend programma, waarbij er feitelijk niets op het programma staat.

Het Utrechts Geo Darts Dispuut *Bull's Hit* zorgde tevens voor de nodige ontspannende momenten. Gesprekken met diverse leden, zowel oud en jong, hebben mede geholpen om een richting te bepalen tijdens en na mijn studie. Ik betreur het nu al dat er in de nabije toekomst minder tijd zal zijn om actief deel te nemen aan de diverse activiteiten.

Financial support for travel and computational resources was obtained from the Dutch Science Foundation (NWO), Dr Sch urmann foundation, NCF, and NATO.

CURRICULUM VITAE

- May 15, 1968 Born in Rijswijk, The Netherlands
- 1980 - 1986 HAVO, Het Betaafse Kamp, Hengelo, The Netherlands
- 1986 - 1988 VWO, Het Betaafse Kamp, Hengelo, The Netherlands
- August, 1994 Doctoraal examen (MSc degree) Geophysics,
(judicium: *Met genoeg*)
Utrecht University, The Netherlands
- 1995 - 1999 Research assistant (AIO),
Department of Theoretical Geophysics,
Utrecht University, The Netherlands